# MAGNETIC TUNNEL JUNCTION BASED SPINTRONIC LOGIC AND MEMORY DEVICES

A DISSERTATION
SUBMITTED TO THE FACULTY OF THE GRADUATE SCHOOL
OF THE UNIVERSITY OF MINNESOTA
BY

XIAOFENG YAO

IN PARTIAL FULFILLMENT OF THE REQUIREMENTS
FOR THE DEGREE OF
DOCTOR OF PHILOSOPHY

ADVISOR: PROFESSOR JIAN-PING WANG

NOVEMBER 2011

**Acknowledgements**

I would like to thank my Ph.D advisor Professor Jian-Ping Wang for his patient guidance and invaluable support. He inspired me with his enthusiasm for scientific research, provided me the opportunity to work in such an exciting field, and showed me how to overcome the difficulties during the research study. He has also given me much valuable advice and considerate support for my future career. I would like to thank Professor Randall Victora, Professor Jack Judy, Professor Bethanie Stadler, Professor Chris Leighton, and Professor Paul Crowell from MINT center, from whom I learned a lot about magnetism and magnetic materials. I would like to thank Professor David Lilja and his student, Shruti Patil for valuable discussion on spintronic logic devices. I appreciate the help from Professor Bethanie Stadler, Professor Anand Gopinath, and Professor Tianhong Cui for serving on my Ph.D committee.

I would like to thank all the staffs in NSF Nano Fabrication Center, who gave me a lot of help and suggestions during the device fabrication. Dr. Rajiv Ranjan and Dr. Roger Malmhall from Avalanche Technology gave helpful comments and suggestions on MTJs.

Dr. Hao Meng, Yisong Zhang and Andy Lyle gave me valuable discussions on the subject of current induced switching in MTJ. I appreciate the help from Jonathan Harms and Farbod Ebrahimi on the HSPIC simulation. I also would like to thank all the other

MINT members, Dr. Jianmin Bai, Dr. Weikang Shen, Dr Jiaoming Qiu, Dr. Yunhao Xu, Dr. Xiao Shen, Dr. Patrick McGray, Dr. Liwen Tan, Dr. Xiaoqi Liu, Dr. Xi Chen, Dr. Stephanie Hernandez, Dr. Xiaobo Huang, Haibao Zhao, Yuanpeng Li, Hao Wang, Hui Zhao, ShiHai He, Nian Ji, Ying Jing, and Yan Dong for their friendship and discussions.

My sincere thanks also go to my parents, Guosheng Yao, Yuzhu Sun and my sister, Danfeng Yao, who provided me with an infinite amount of love and support during my hard times. To them, this thesis is dedicated.

## Abstract

The development of semiconductor devices is limited by the high power consumption and further physical dimension reduction. Spintronic devices, especially the magnetic tunnel junction (MTJ) based devices, have advantages of non-volatility, reconfigurable capability, fast-switching speed, small-dimension, and compatibility to semiconductor devices, which is a promising candidate for future logic and memory devices. However, the previously proposed MTJ logic devices have been operated independently and therefore are limited to only basic logic operations. Consequently, the MTJ device has only been used as ancillary device in the circuit, rather than the main computation component.

In this thesis, study has been done on both spintronic logic and memory devices. In the first part, systematic study has been performed on MTJ based logic devices in order to expand the functionalities and properties of MTJ devices. Basic logic cell with three-input has been designed and simulated. Nano-magnetic-channel has been proposed, which is the first design to realize the communication between the MTJ logic cells. With basic logic unit as a building block, a spintronic logic circuit has been designed with MTJ as the dominant component. HSPICE simulation has been done for this spintronic logic circuit, which acts as an Arithmetic Logic Unit.

In the spintronic memory device part, study has been focused on the fundamental study on the current induced switching in MTJ devices with hybrid free layer. With hybrid free layer, magnetic non-uniformity is introduced along the current direction, which induces extra spin torque component. Unique current-induced switching has been observed and studied in the hybrid free layer MTJ. Adiabatic spin torque, which is introduced by spatial non-uniform magnetization in the hybrid free layer, plays an important role for the unique switching. By tuning the bias field, single-polar current switching was achieved in this hybrid MTJ device, which gives the potential application of unidirectional switching in the spintronic memory devices.

## Table of Contents

## List of Tables

## List of Figures

### Chapter1



### Chapter 2

**Chapter 3**

**Chapter 4**

**Appendix A**



**Appendix B**

# Chapter 1 Introduction

## 1.1. Basics on Spintronics

Spintronics is a new created and combination word based on “spin transport electronics”, which was first introduced in 1996 to designate a program of U.S. defense advanced research project agency (DARPA) [1]. It is a new emerging technology to study on the intrinsic spin of the electrons and corresponding magnetic moments, in addition to the intrinsic electrical charge.

The basic principles of spintronics are briefly explained as follows. When a current is passing through a magnetic material, the conduction electrons in the current will be polarized by the local magnetic moment of the magnetic material. The majority spins will have the same direction as that of local magnetization, and the minority spins will have opposite direction to the local magnetization. The degree of the amount of majority spins relative to minority spins is described as spin polarization. This is an intrinsic property in a material, which is depended on the magnetization in that magnetic material. The polarized conduction electrons will contain the information (magnetization direction) of that magnetic material. The spin direction of the conduction electrons will be gradually changed from their original direction, when these polarized electrons continue flowing through another material and interact with local electrons/lattice. This process is called spin relaxation, and the distance the electrons can travel while keeping the spin direction is called spin diffusion length. And damping constant is the parameter

of a material, which is usually used to describe how fast a spin is relaxed in that material. The spin diffusion length is varied with different materials. Within the spin diffusion length, when polarized electrons enter another magnetic material, the spins of the polarized electrons will interact with local moments. Both directions of the conduction electron spins and local moments will be changed and align toward to each other. This magnetic moment change is depended on both the local moment and the initial moment which polarized the transport electrons. The giant magneto-resistance effect and magnetic tunneling effect are based on this interaction between transport electrons and local moments which links two magnetic layers. In the next section, we describe two types of spintronics devices, namely giant magneto-resistance (GMR) and magnetic tunnel junction (MTJ).

## 1.2. Spintronic Devices

### 1.2.1. Giant Magneto-Resistance and Magnetic Tunnel Junction

Giant magneto-resistance (GMR) and magnetic tunnel junction (MTJ) have similar sandwich-like structure, which includes two ferromagnetic layers separated by a non-magnetic layer. This non-magnetic layer is a metal layer in GMR devices and a insulate layer in MTJ devices. When two ferromagnetic layers have the parallel magnetization direction, the device resistance is low; when they are at opposite direction, it will show high resistance. GMR was first discovered in 1988 simultaneously but independently by Peter Grünberg of Forschungszentrum Jülich (Germany) and Albert Fert of the Univerisity of Paris-Sud (France). Grünberg studied a Fe/Cr/Fe trilayer

system, and Fert studied in Fe/Cr multilayer system. 2007 Nobel Prize in physics was awarded to Grünberg and Fert for the discovery of GMR, which is considered as the birth of spintronics [2].

The magnetic tunneling effect was originally discovered in 1975 by M. Jullière (University of Rennes, France) in the study of Fe/GeO/Co junctions at 4.2 K [3]. Room temperature tunneling effect was first reported by Maekawa and Gäfvert in 1982 with a system of Ni/NiO/FM, where FM is Fe, Co or Ni [4]. The MR ratio was a few per cent and this work remains unnoticed for a long time. In 1995, the breakthrough came with the use of amorphous $Al_2O_3$ tunneling barrier reported by two groups: T. Miyazaki's group[5] from Tohoku University[6], Japan, and J.S. Moodera's group from Massachusetts Institute of Technology, USA. The MR ratio was found to be 18% in $Fe/Al_2O_3/Fe$ [5] and 12% in $CoFe/Al_2O_3/Co$ [6] both at room-temperature.

In both GMR and MTJ devices, the two magnetic layers are defined as fixed layer and free layer, which have high and low switching field/current, respectively. Fig.1.1 shows the evolution of the magnetically engineered multilayer structures[7]. In order to get high switching field/current, synthetic antiferromagnetic (SAF) structure is usually used, which has a pinning layer, IrMn, and two ferromagnetic layers separated by a thin (0.8 nm) Ru. In GMR devices, Cu, which has long spin diffusion length, is widely used as a non-magnetic layer. For MTJ devices, there are two generations. First generation used amorphous $Al_2O_3$ as tunneling barrier, and the MR ratio can be as high as 70% [8]. The second generation of MTJ devices uses crystallized MgO barrier. The high oriented MgO structure gives as large as 604% MR ratio at room temperature[9]. The main

component of this Ph.D. thesis is based on the investigation of magnetic tunnel junction (MTJ) devices, which have much higher MR ratio than GMR devices.

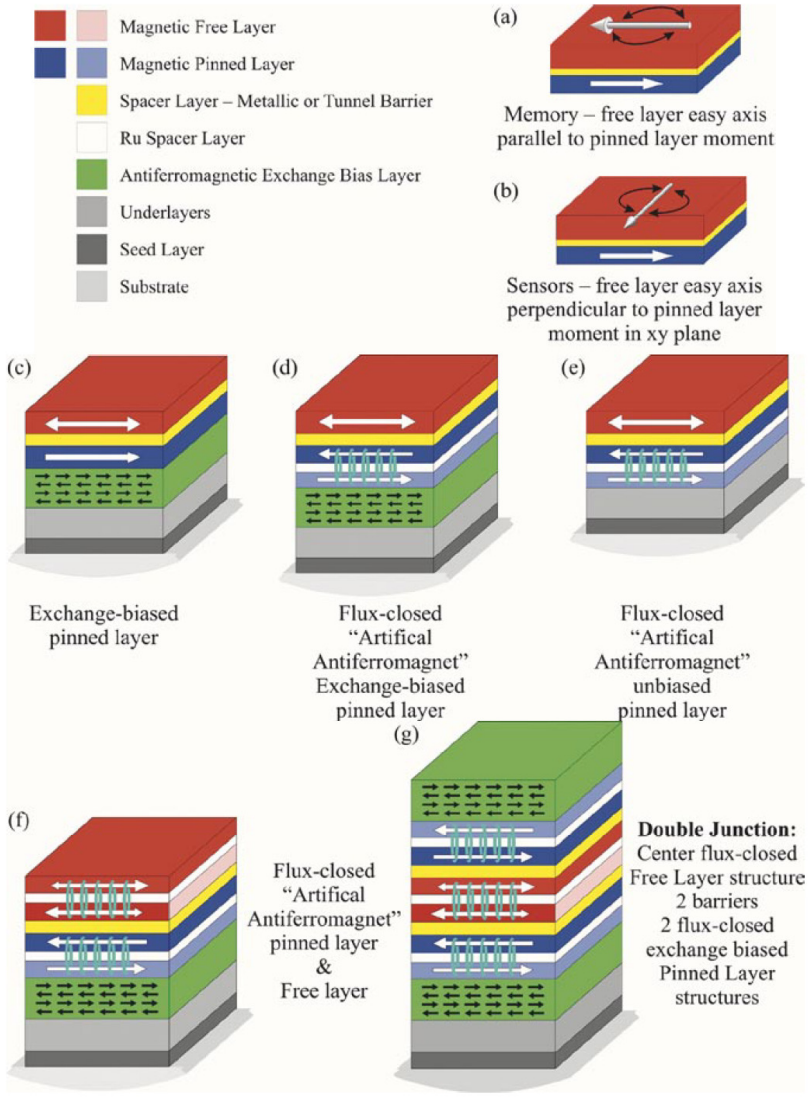


Fig.1.1(ref. [7]) Evolution of magnetically engineered multilayers: (a), (b) Varied orientation in free layer based on applications; (c) A basic GMR/TMR (tunneling magnetoresistance) stack; (d) Pinned layer uses antiferromagnetically coupled structure through a ruthenium (Ru) spacer layer. This flux closure increases the pinned layer magnetic stability and reduces coupling to the free layer. (e) Similar structure as (d) but without exchange bias layer to discourage rotation of the pinned element. (f) Both the pinned and free elements consist of AF-coupled pairs. (g) A double tunnel junction. All ferromagnetic elements consist of AF-coupled pairs. Spin filtering occurs both as current tunnels from the first pinned layer to the free element and again as it tunnels from the free element to the second pinned element.

### 1.2.2.Current Induced Magnetization Switching and Spin Transfer Torque

Traditionally, magnetic field is used to switch the free layer magnetization, and a current line is used to generate the magnetic field. However, the amplitude of the current, which needs to generate a large enough magnetic field, cannot be reduced with the device scaling. At the same time, there will be cross-talk issue when two current lines locate too close to each other. In 1996, J.C. Slonczewski [10] and L. Berger [11] independently predicted in theory that the current can be used to switching the magnetization. Later in 1998, M. Tsoi's group experimentally demonstrates the current induced magnetization switching in Co/Cu multilayers structure[12]. STT uses a current directly passing through the MTJ element to switching its free layer magnetization, without disturbing adjacent MTJ elements. Furthermore, the critical switching current is proportional to the device area so that the dynamic power is reduced with device scaling.

### 1.2.3. Spintronic Logic Devices

Great success has been achieved with transistor based semiconductor devices. However, the drastic increase of power consumption and the physical dimension limitation are the main challenges for future devices [13]. Spintronic devices are based on both the charge and the up and down spins of the electrons, rather than only on the charge of the electrons. A spintronic based device has the potential benefits of functionalities (e.g. non-volatility), faster computing, relatively low power dissipation, and higher-density integration when compared to the transistor-based device. Presently, several spintronic logic devices have been reported, which are magnetic cellular automata

(MCA) [14-17], domain wall logic [18-20], and magnetic tunneling junction (MTJ)-based logic [21-32].

| | CMOS-based | MTJ/GMR logic | | MQCA | Domain wall logic |
|---|---|---|---|---|---|
| **Element** | Transistor | MTJ/GMR | | Magnetic dot/pillar | Domain wall |
| **Binary states** | Voltage | Resistance (high, low) | | Magnetization direction | (head to head; tail to tail) |
| **Driving force** | Voltage | Magn. Field | Pulse current | Magn. field | Rotating magn. field |
| **Programmable Reconfigurable** | Yes | Yes | Yes | No | No |
| **Non-volatile** | No | Yes | Yes | Yes | Yes |
| **Power** | High | High | Low | Low | High |
| **Speed** | <ns | < ns | < ns | <ns | ns under large field |
| **Density** | Medium | Low | High | Low | Low |
| **Reliability** | High | High | High | Potentially low | High |
| **Radiation-hard** | No | Yes | Yes | Yes | Yes |

Table 1.1 Comparison of the properties of the different types of the logic devices.

Table 1.1 compares the properties of the three spintronic logic devices with traditional CMOS based devices. The unique advantages of being programmable and reconfigurable make MTJ based-logic an attractive system. Compared to the mature semiconductor technology, the development of MTJ based logic devices is still in its infant stage. Basic logic functions have been designed and demonstrated in magnetic field switching MTJ devices. As discussed in section 1.2.2, the limitations of magnetic field switching cannot meet the requirements for device scaling and power reduction. When spin transfer torque

was found, it quickly replaced the field switching method and dominant the development of MTJ devices. In 2008, Tohoku University and Hitachi Advanced Research Laboratory fabricated a nonvolatile full adder using STT switched MTJs [33,34]. This work demonstrated the compatibility of MTJ with CMOS devices and the potential to realize logic-in-memory and system-on-chip architecture. However, the reported MTJ logic devices have operated independently and therefore are limited to only basic logic operations. Consequently, the MTJ device has only been used as an ancillary device, rather than the main computation device. As a result, the full benefits of MTJ based computation have not been explored. A revolutionary breakthrough is needed to boost the development of MTJ based logic devices. The communication between MTJ cells is indispensable to expanse the logic functions. At the same time, the systematical study is needed which creates the fundamental building blocks for the future spintronic logic circuits, similarly to the CMOS and gate in semiconductor circuits.

## 1.3. Summary of Contributions

My three main technical contributions -- including the design and simulation magnetic tunneling junction based logic devices, the discovery of single polar current switching phenomenon in MTJ under various magnetic fields, and the study of MTJ devices with special intermediate states -- are summarized as follows.

- Magnetic tunneling junction (MTJ) based programmable logic devices have been proposed and studied for future reconfigurable and non-volatile computation devices and systems. Spin Transfer Torque (STT) based switching has advantages

in device scaling compared to the field-switching mechanism. However, the previously proposed MTJ logic devices have operated independently and therefore are limited to only basic logic operations. Consequently, the MTJ device has only been used as an ancillary device, rather than the main computation device. As a result, the full benefits of MTJ based computation have not been explored. New designs are needed to accelerate the development of the MTJ based logic devices. Specifically the realization of direct communication between the MTJ devices is crucial to fully utilize the MTJ devices in the circuits to implement more advanced logic functions. In this paper, new MTJ based spintronic logic units (building blocks) for spintronic circuits using the STT switching mechanism have been proposed and investigated, which includes the designs of a basic STT-MTJ logic cell, a direct communication between the MTJ logic cells, a three-MTJ logic unit and a spintronic logic circuit acting as an Arithmetic Logic Unit.

- The discovery of spin torque transfer (STT) has lead to a significant advance in the development of spintronic devices. Novel structures and materials have been studied in order to improve the performance of the magnetic tunnel junctions (MTJs) performances and understand the fundamental physics in spin torque transfer. The adiabatic spin torque effect, which is due to the spatial non-uniformity of magnetic properties, has been predicted in theory and demonstrated experimentally in magnetic nanowires. However, this important spin torque has been rarely concerned in the magnetic tunnel junctions (MTJ) because of its

extremely weak effect in conventional MTJs. This paper reports for the first time a giant adiabatic spin torque in MTJ devices with a hybrid free layer structure. The generation of the giant adiabatic spin torque was realized through the introduction of a spatial magnetic non-uniformity in a hybrid free layer along the current direction. It is observed that the giant adiabatic spin torque can substantially promote the current-induced switching process in the MTJ devices: the adiabatic spin torque can be larger than the in-plane spin torque, which allows for the switching with a single-polar current under different bias fields. Moreover, the adiabatic spin torque, which is proportional to the level of spatial non-uniformity, increases during the switching process. The observed effects are confirmed by numerical simulations. These results have far-reaching implications for the future of high-density STT-MRAM devices.

- The current-induced magnetization switching was studied in the MTJ devices with composite free layer (CoFeB/CoFeB-oxide/CoFeB). The stable intermediate state was observed due to the multi-domain structure induced by the dipole field and large device size. Two different stable intermediate states were observed in different applied current direction. The switching mechanisms of those two intermediate states are different, which is also indicated by the switching current distribution. Reversible intermediate state was also observed at low applied current, which may be due to the domain nucleation.

# Chapter 2 Experimental Methods

## 2.1 Magnetic Tunnel Junction Development

Magnetron enhanced sputtering is very important and widely used method in thin film deposition. A very high vacuum (below 1E-7 Torr) is preferred for thin film deposition. Magnetron enhanced sputtering with DC power supply has a simple setup and widely used for metal layer thin film deposition. The target which has the material to deposit is connected to the cathode of the DC power supply. Plasma is usually struck in mTorr range with Ar gas. The Ar atom or Ar+ ions bombard on the target to knock out the target atoms, which has enough energy to fly through the space between the target and the substrate and deposit on the substrate. During the traveling across the chamber, the target atoms will have collisions with other species and loss their energy. The process pressure is used to control the collision number and then the atom energy. The substrate is usually applied with a bias voltage in order to adjust the energy of the adatoms deposited on it. The substrate temperature is another important parameter which controls the adatom energy in order to get proper properties, such as crystal structure. For DC magnetron sputtering, the target should have good conductivity so that the accumulated charges on the target surface can flow away. For the insulate materials, the charges will accumulate on the target surface and repulse the Ar+ ions to further bombard on the target, and induce arcs which makes the plasma instable. RF power supply is used for insulate material deposition, which has alternative voltage applied on the target to avoid any charge accumulation. The frequency for RF deposition usually uses the standard 13.65 MHz. Matching network is used together with RF power supply which tunes its

impedance to match chamber environment in order to get the minimum power loss. In the deposition of magnetic tunnel junction, both DC and RF magnetron sputtering were used.

As explained in section 1.2.1 Magnetic tunnel junction has basic sandwich-like structure, which is fixed magnetic layer, tunneling barrier layer and free magnetic layer. And synthetic antiferromagnetic (SAF) structure is used to pin the fixed layer and minimize the leakage flux from the fixed layer to the free layer. The general MTJ structure is: substrate/bottom electrode/pinning layer (IrMn)/pinned layer/Ru/fixed layer/tunnel barrier/free layer/bottom electrode. Thin Ru layer (0.8nm) is used to induce the exchange coupling between the pinned layer and the fixed layer. All the multilayer structure was sputtered using Shamrock sputter system (Fig.2.1), which has six targets.

Fig.2.1 Shamrock Sputtering System, with load/unload chamber; transfer chamber and main deposition chamber with six targets.

The property of the tunneling barrier, MgO, which is only one and two nanometer in thickness, is very critical to get high tunnel magnetoresistance ratio (TMR). The highly (001) oriented crystal structure and the smooth interface are preferred. MgO (001) plane is the lowest energy plane. However, with sputtered method, MgO film is polycrystallized. The effects of underlayer, process conditions were studied in order to get high (001) oriented MgO film.

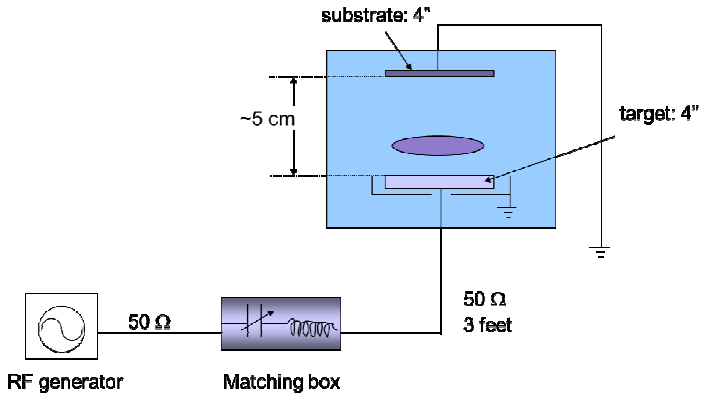


Fig.2.2 schematic drawing of radio frequency (RF) magnetron sputtering system.

First, underlayer effect was studied with thick MgO film. Various underlayers with either amorphous or crystallized structure were studied. CoFe is usually used as a fixed layer in MTJ, due to small lattice mismatch between CoFe(001)[100] and MgO (001)[110] (Fig.2.3). Therefore, CoFe40 underlayer was studied first. It found that CoFe40 film easily built (110) orientation, which will induce MgO (110) growth instead of (002) orientation. No MgO (002) peak was found in X-ray diffraction and X-ray micro-diffraction pattern. When MgO was directly deposited on thermal oxide SiO2 underlayer, (220) orientation is dominant in the film instead of (002) texture, which is not

preferred in MTJ. When using CoFeB underlayer, (002) texture in MgO was obtained at room-temperature with a Ta seedlayer on SiO2 substrate (Fig.2.4). It indicates that the growth of MgO is very sensitive to the crystal structure of the underlayer, and the lowest energy plane (001) is preferred to growth on amorphous surface if there is no (001) orientation in the underlayer.

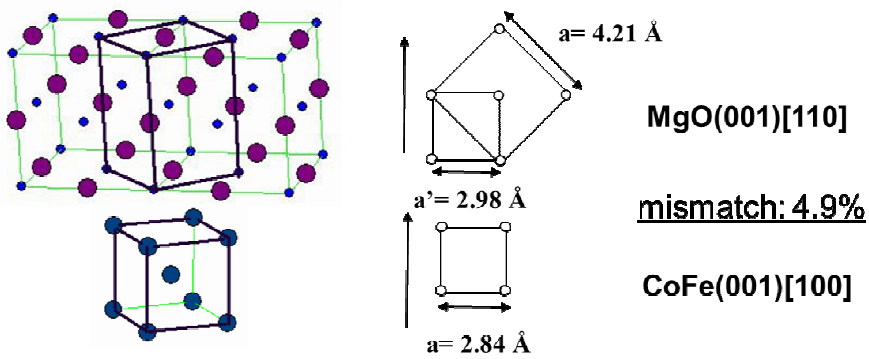


Fig.2.3 Schematic drawing of crystal structure of CoFe and MgO. The mismatch between CoFe (001)[100] and MgO (001)[110] is 4.9%.

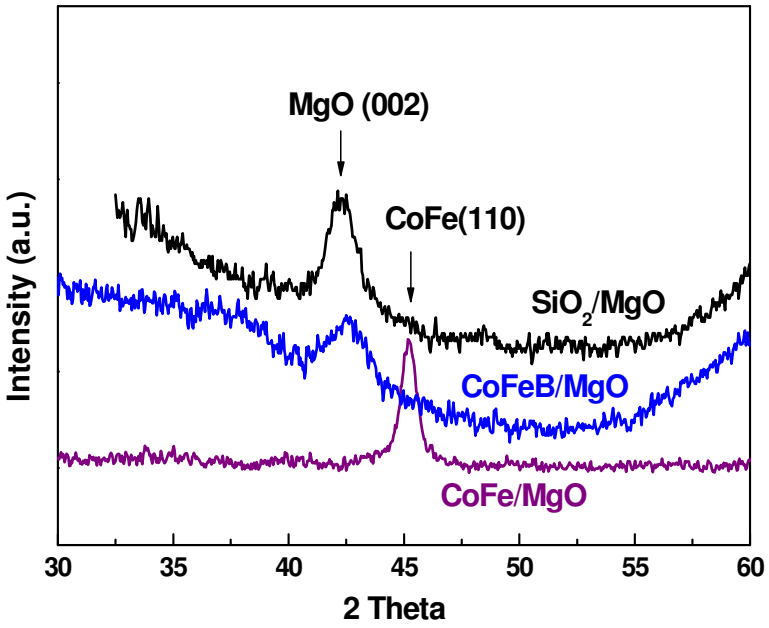


Fig.2.4 X-ray Micro-diffraction spectra of thick MgO film on different underlayer.

With the same CoFeB amorphous underlayer, the sputtering conditions of MgO film were studied with the film structure of substrate/Ta30/CoFeB30/MgO150Å. Fig.2.6 shows the X-ray micro-diffraction spectra of samples with different MgO sputter power. The sputtering power of MgO was changed from 120W to 384W with fixed 1.5 mTorr pressure. The MgO (200) peak increases with the power increasing, and reach the maximum at about 300W. Further increasing the power doesn't enhance MgO (200) orientation. Fig.2.5 shows the x-ray micro-diffraction images for these samples. The brightness represents the peak intensity, and the width and the length of the arc represent for the in-plane orientation. It shows that the brightness (peak intensity) increases with the power. And the arc is sharp and short which means the in-plane distribution of (200) texture is good. This result indicates that there is a threshold energy of adatoms to get good (200) orientation, and in our sputtering system, 300 W (3.74 W/cm$^2$) is the optimized power at 1.5 mTorr pressure. The grain size was calculated by: g.s.=(0.9*λ)/(FWHM*cos(θ)), where λ is x-ray wavelength, θ is the peak location, and FWHM is full width at half maximum. For the sample with highest power, FWHM is 4.4º and the grain size is 9.9 nm.

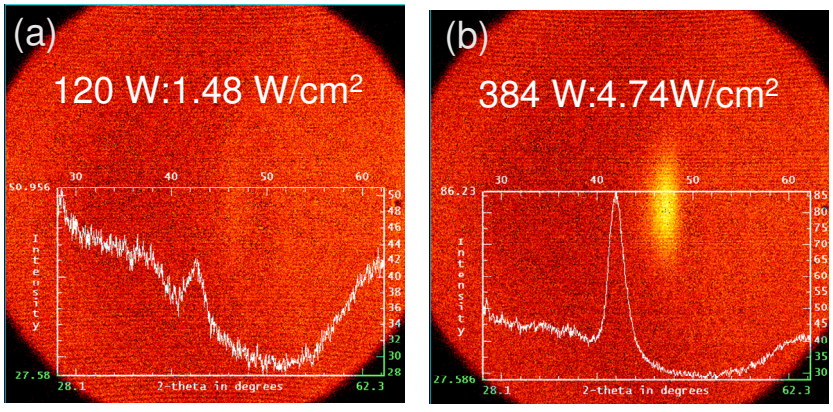


Fig.2.5 Micro-diffraction images for as-deposited samples with

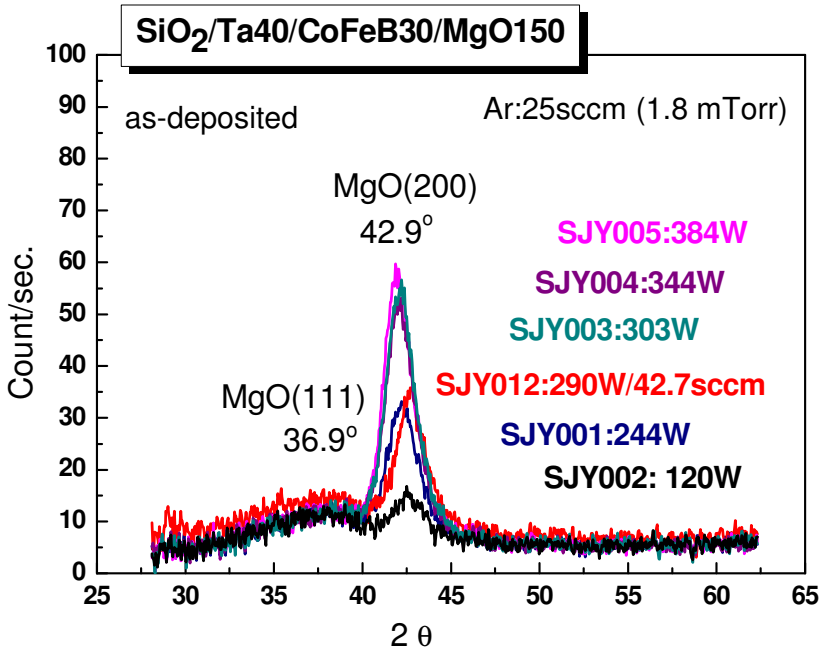


Fig.2.6 X-ray micro-diffraction spectra for as-deposited MgO film with different sputter power.

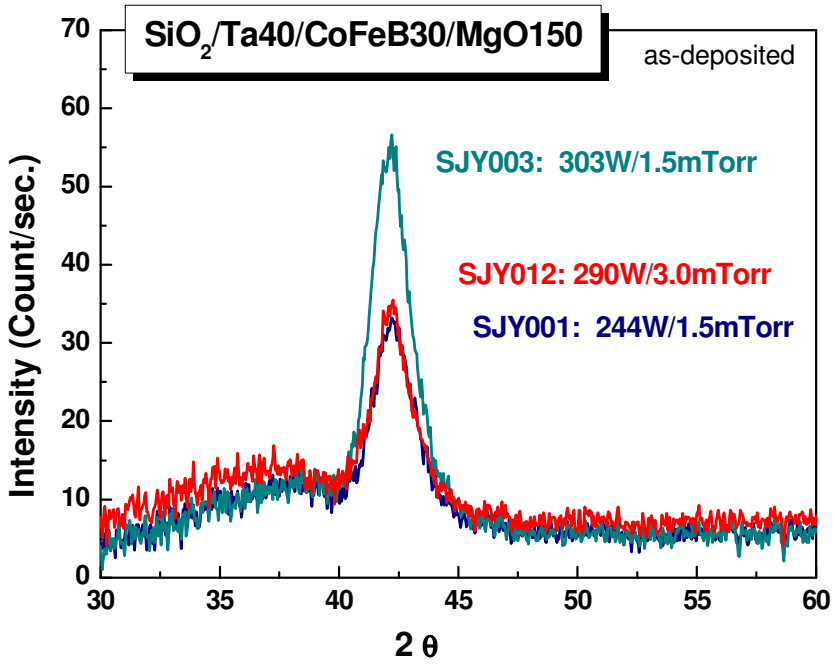


Fig.2.7 X-ray micro-diffraction spectra of as-deposited MgO film with different sputtering pressure.

Fig. 2.7 shows Ar pressure effect on MgO orientation. With similar power (~300 W), higher pressure gives poor MgO (200) orientation. As discussed earlier, there is threshold energy for adatoms. When the pressure increases, there are more gas atoms in the chamber and the collision number increases which reduce the atoms/ions energy. The mean free pass of the Ar gas can be calculated by the following equation: $\lambda_{mfp}=(k_BT/\pi d^2_cP)$, where $\lambda_{mfp}$ is the mean free pass in that gas; $k_B$ is Boltzmann constant ($1.3806\times10^{-23}$); T is temperature (293 K); P is pressure; and $d_c$ is the diameter of the gas atom ($d_c$_Ar=362 pm). Under 1.5 mTorr (199.98 Pa), the mean free path is 4.91 cm, which is close to the target to substrate distance in our sputter system. It indicates that only one collision will happen during the flying of the atoms outside the plasma. When the pressure increases to 3 mTorr (399.96 Pa), the mean free path reduces to half: 2.46 cm, and the collision increases to twice which reduces the atoms' energy. Therefore, from the x-ray micro-diffraction result, MgO (200) orientation got worse under 3 mTorr compared to 1.5 mTorr. If further reducing the pressure (lower than 1.5 mTorr), atoms' energy may increase with less collision and the MgO (200) growth will be enhanced. Due to the hardware limitation in our sputter system, low pressure study didn't be performed: the Mass Flow Controller shows large variation for small flow rate (below 25 sccm (1.5 mTorr)). Another knob to control the atom energy is substrate bias. In this study the substrate is grounded for all the samples. By applying negative bias to the substrate, the Ar+ ions will be accelerated which also increases the adatoms energy and enhance (200) growth. This substrate bias study could be done in the future after the hardware modification.

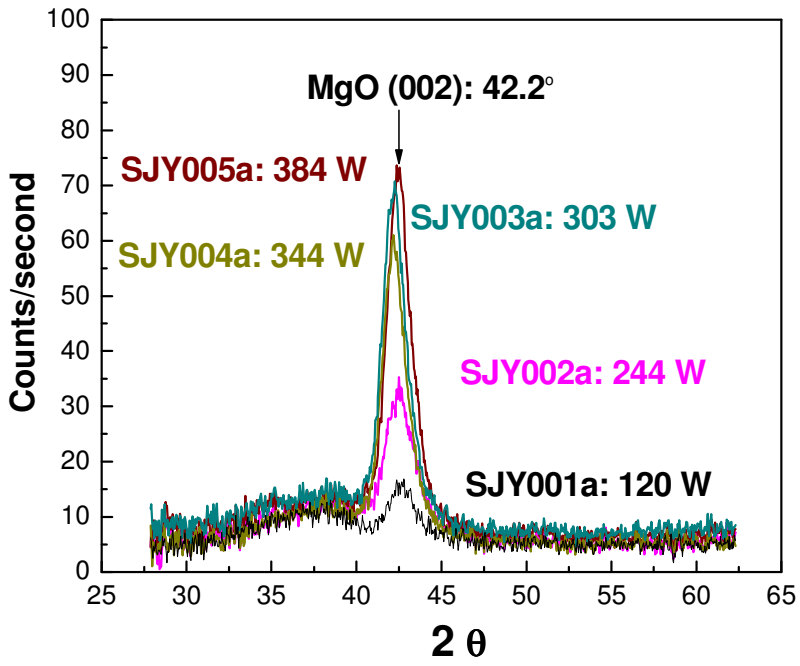


Fig.2.8 X-ray micro-diffraction spectra of post-annealed MgO film with different sputtering power.

As discussed above, by optimizing the underlayer and sputtering conditions, (200) texture can be achieved in MgO layer. However, the (200) texture in these as-deposited samples are not good enough to get high TMR ratio. Post-annealing is very critical for MgO based MTJ, which can dramatically improve the crystallinity of the MgO layer. The TMR ratio is highly depended on MgO crystal structure through post-annealing treatment. Fig2.8 shows the MgO (200) peak intensity under different sputter power before and after the annealing process. With low sputter power, the peak intensity doesn't change after post-annealing; while when the power is higher than threshold power, the peak intensity starts to increase after annealing, which indicates the improvement of MgO

(200) orientation. The annealing time is usually 1~2 hours, and the annealing temperature is in the range of 250~400 °C. With the annealing temperature and time increasing, the crystallinity of MgO barrier improves which results in high TMR ratio. At the same time, the device resistance will also increase since MgO is an insulate material. Then, larger current/voltage is needed to switch the MTJ devices, which is not the right direction of the application. Therefore, optimized annealing condition is needed to get large enough TMR ratio and small enough switching current/voltage. A magnetic field is applied during post-annealing, which is to align the magnetization direction of the fixed layer.

In MgO-based MTJ devices, the fixed layer, the free layer and the tunnel barrier are all very thin (1~3 nm). Therefore the interface roughness is very critical for MTJ performance. The smooth interface will reduce the scattering effect during the electron transportation, and improve TMR ratio. Also, the smooth surface is desired to get good crystal orientation during the film growth. In the MTJ devices, besides the basic MTJ structure, there are also bottom and top electrodes, which are used for applying current and measuring voltage across the junctions. The MTJ structure will be deposited on the bottom electrode and the surface roughness needs to be controlled as low as possible. Fig.2.9(a) shows the AFM (atomic force microscopy) images of the substrate: Si with 1000 Å thermal oxide SiO2. Thick SiO2 layer is for device fabrication purpose which will be discussed in the section 2.2. The roughness (RMS: root mean square) is 0.209 nm with scanning area of 1 μm x 1 μm. Fig.2.9(b) shows the AFM images of the sample with the structure of Si substrate/SiO2/Ta40/CoFeB30/MgO20/Ta20Å. The MgO deposition condition is the optimized condition which is discussed earlier. The roughness increase

slightly, RMS=0.287 nm, compared to the substrate with thermal oxide, which indicates that the deposition of CoFeB and MgO films has relatively smooth interface. There is a minimum thickness for the bottom electrode, which is due to device fabrication requirements. During the MTJ device fabrication, usually slightly over-etching is needed to make sure the etching is complete for all the area across the wafers. Therefore, a minimum thickness is required to get proper fabrication margin (~900 Å). If a single metal layer is grown as the bottom electrode, the roughness will be very large because the grain size increases with the thickness increasing which results in large roughness. In this study, two metal layers were alternatively deposited in order to minimize the roughness with target thickness. Metals with good conductivity were chosen, which are Al and Cu. A thin Cu (30 Å) layer was deposited after each Al (150 Å) layer, which is to break the growth of Al grains. The roughness for a total 950 Å bottom electrode is 0.322 nm, shown in fig (c), which is 0.12 nm larger than the roughness of the substrate.

(a) $Si/SiO_2$ 100nm
RMS: 0.209nm

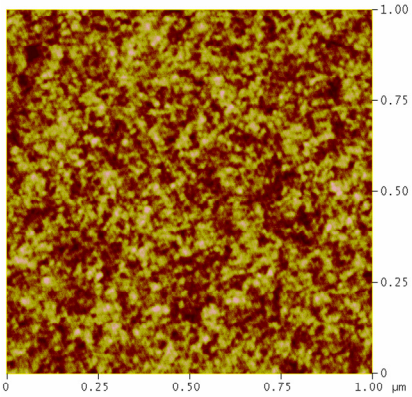


(b) $SiO_2$/Ta4/CoFeB3/MgO2/Ta2nm
RMS: 0.287nm

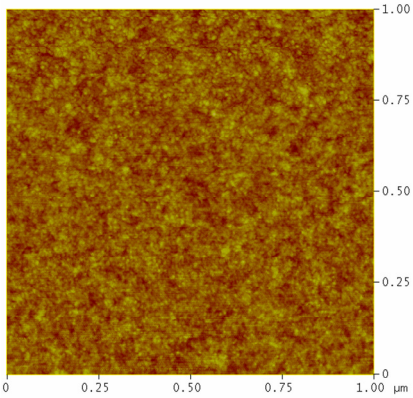


(c) $SiO_2$/Ta2/$(Al15/Cu3)_4$/Al15/Ta3nm
RMS: 0.322nm

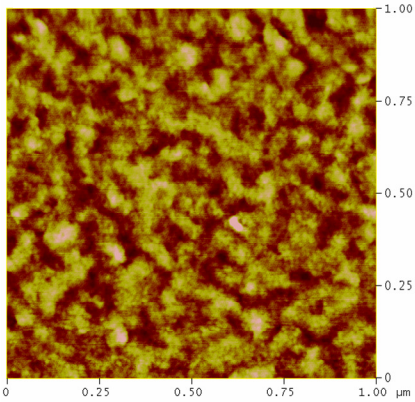


Fig.2.9 AFM images of (a) substrate with thermal oxidation layer; (b) MgO film deposited on CoFeB underlayer on $Si/SiO_2$ substrate; (c) multilayer structure used for bottom electrode.

## 2.2 Magnetic Tunnel Junction Fabrication

The magnetic tunnel junction multilayer films were deposited in the sputtering system without breaking the vacuum, which includes bottom electrode, MTJ stack, and top electrode. And after post-annealing treatment, the sample is ready for nano-scale device fabrication. All the steps in the device fabrication were done in the cleanroom of Nano Fabrication Center of University of Minnesota.

The whole MTJ device fabrication procedure includes four main parts: 1) bottom electrode patterning (photo-lithography); 2) MTJ stack patterning (e-beam lithography); 3) Planarization (photo-lithography); and 4) top electrode patterning (photo-lithography). The schematic drawing is shown in Fig.2.10, and the detailed fabrication flow is shown in table 2.1. Photo-lithography method is the fundamental part and frequently used in the device fabrication, which is explained in the follows. The photo-lithography includes 1) resist coating; 2) UV exposure; 3) resist development; 4) etching; and 5) resist removal. The wafer was prebaked at a temperature sufficient to remove any moisture at surface, and the baked temperature and time are depended on the resist type. Then the resist is spin coated on the wafer, and the resist thickness can be adjusted by the spinning speed. After coating, the wafer is baked (soft-bake) which is to remove the residual resist solvent. In the second step, the wafer is aligned with a mask which has designed device pattern. The pattern is coated by Cr, which can block UV light. The rest part of the mask is transparent for UV light. For positive tone resist, the resist which is exposed to the UV light, becomes soluble to the photoresist developer. And for the negative tone resist, the

resist which is exposed to the light becomes insoluble to the resist developer. After UV

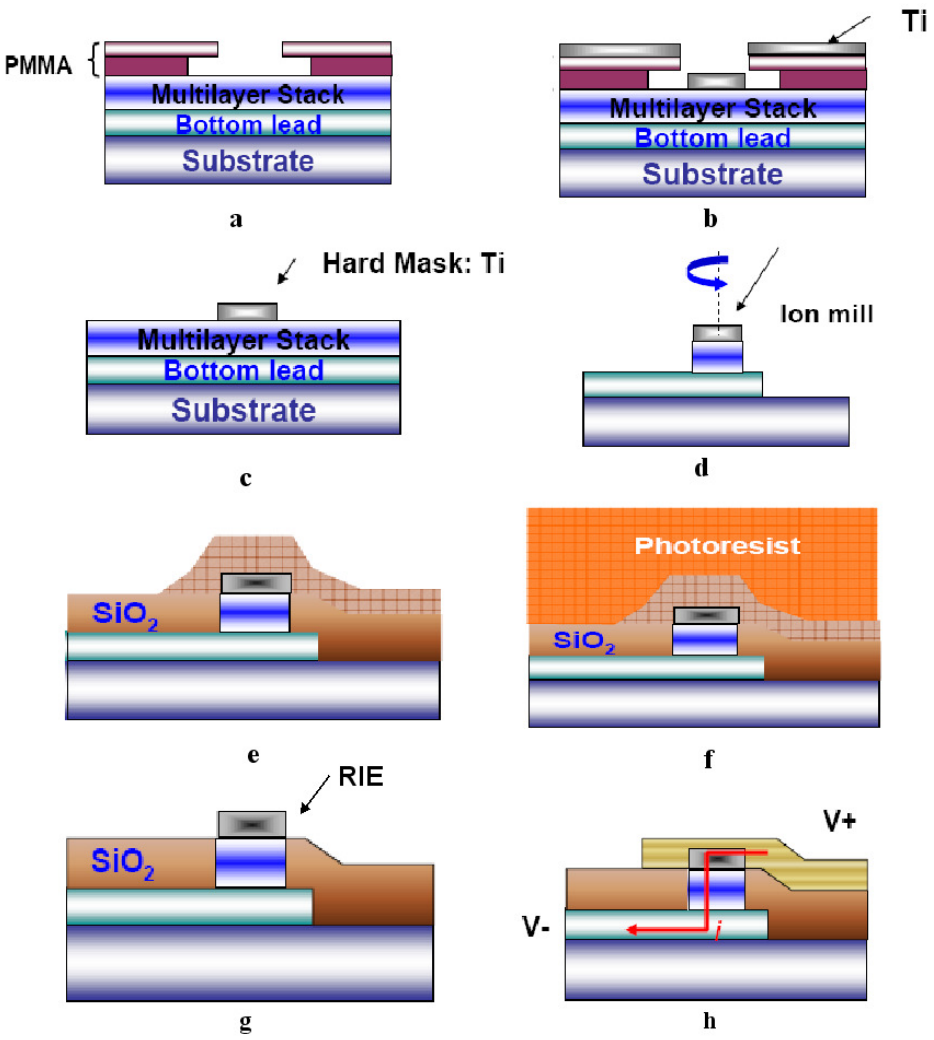


Fig.2.10 The fabrication flow of Magnetic Tunnel Junction devices. a) e-beam resist definition b) Ti hard mask deposition c) hard mask lift-off d) ion milling of MTJ stack e) insolate layer deposition f) photoresist coating for planarization g) planarization by reactive ion etching h) top electrode definition

exposure and development, the wafer is baked again (hard-bake) in order to make the resist harder for the following etching process. Now the photoresist acts as an etching mask which protects the underneath films, the area which is opened will be etched. Ion milling is generally used for etching. Ar+ ions which are generated by the plasma are accelerated and bombard on the wafer surface. Because it is a physical bombardment, ion milling method can etch both metal and insulate materials. The wafer holder can be tilted in order to set the proper angle between the wafer and the ion beam direction. The etching time is controlled by a reference sample, and a slight over-etching may be needed. The final step for photolithography is resist removal. A particular resist remover is used for each type of resist. During the etching the resist is also etched and bombarded by Ar+ ions, which becomes harder and difficult to be removed. For some of the resist removals, the wafer can be put in a bath with higher temperature which will improve the removal efficiency.

E-beam lithography, which uses shorter wavelength exposure source, is used to pattern MTJ stack into nanometer scale. It has similar procedure as photo-lithography, but with different resist type and exposure source. E-beam resist, which is sensitive to the shorter wavelength, is baked at much higher temperature than that for the photo-resist, in order to completely remove the moisture and get good adhesion. The thickness of the e-beam resist is much thinner (a few hundreds nm range) than the photoresist (in the range of um), because the minimum feature dimension is also limited by the resist thickness (roughly, about one third of the resist thickness). For MTJ stack patterning, metal hard mask (Ti) is usually used for stack etching due to long etching time (depth), and lift-off

process is needed to define Ti hard mask. Bi-layer e-beam resist is usually used for the process involved lift-off, which can generate an "undercut" structure. In our study, e-beam resist is PMMA (polymethyl methacrylane). The bottom resist is PMMA 495K A4 (~160nm) and top resist is PMMA 950K C2 (~120nm). 495K and 950K represent for the molecular weight of the resin in the resist; A and C series are the solvent type, which is anisole or chlorobenzene, respectively. The number after solvent type indicates the density of the resist which controls the resist thickness. Different types of PMMA are required for bi-layer structure, which can form undercut structure after developing (smaller opening in top resist and wider opening in bottom resist).

The e-beam exposure is the most critical step in the MTJ patterning in order to get nanometer scale patterns/devices, which is required for current induced magnetization switching. The e-beam exposure was done using Raith 150. And every step, which is related to e-beam, is important. For example, the wafer surface should keep clean and flat before the e-beam exposure. And the Au top layer deposition before e-beam may affect it in two ways: 1) the film uniformity (it shows that the film has better uniformity when deposited each at a time by AJA.) 2) the WIP time control between bottom lead patterning and e-beam patterning. The shorter WIP time between two process results gives better results.

For e-beam exposure, there are several important parameters, which will be discussed in details in the following. First is the accelerate voltage, which controls the electrons energy. The higher accelerate voltage gives the higher the electron energy, so that they penetrate deeper into the resist with well confined exposed area. Therefore, in

order to get small pattern size, the higher accelerate voltage is preferred. E-beam exposure equipment, Raith 150, has the highest accelerate voltage of 30kV, which has been used during the fabrication. The optimized exposure dose is ~200~300 uAs/cm$^2$, which is not influenced by the accelerate voltage much.

The aperture size should be kept at 10 um, which has the largest depth of focus (~10 um). 20 um aperture was tried also, which has much smaller depth of focus (~2.5 um). Large depth of focus is required, and the reason is that in the experiments, the wafer or wafer holder is not perfectly flat or parallel to the source. There is a range of the distance between the source and the wafer surface. The larger depth of focus will cover the whole range so that the whole wafer surface can be exposed under the optimized condition. The working distance (WD) does not change the depth of focus much when changes from WD=6.8 mm to WD=10.3 mm. WD=10.3 mm has been used.

"Autofocus" function is an option in 3-point alignment. In this function, the machine will automatically calculate the focus length based on the result of 3-point alignment, assuming the whole 4 inch wafer is a flat surface. The yield is dramatically increased when using this "autofocus" function and with optimized dose. (The yield can be up to 100%.)

Fig.2.11 are SEM images of nano-scale pattern with different size, and these images were taken after Ti hard mask lift-off, which is after step 12 in table 2.1.

| Fabrication Flow of Nano-scale Magnetic Tunnel Junction Devices | | | | |
|---|---|---|---|---|
| **Step** | **Name** | **Purpose** | **Tool** | **Description** |
| 1 | shamrock | MTJ deposition | shamrock | The top lead should be thick enough ~150 nm. |
| 2 | Ion mill | clean surface before Au depositioin | Ion mill | Etch time ~ 3 min, and immediately transfer to AJA |
| 3 | Cover Au layer | Protect metal suface | AJA | Ta/Au total 40 nm (with reference sample and test sample) |
| 4 | Bottom Lead (BL) pattern | Pattern BL | MABA6 | Prebake@115C-1min;<br>P.R.1813-3000PRM-30sec.; softbake105C-1min.;<br>exposure(Mask #2):hard contact;5.5sec;20um;<br>microscope;<br>hardbake 120C-1min |
| 5 | Bottom Lead (BL) pattern | Pattern BL | Ion mill | Angle: 60 degree, Current: 9.5A, Etch 3 min. stop 3 min |
| 6 | Resist removal | remove resist | Web bench | Sonicate 50% at Acetone for 10+ min.,<br>DI water rinse, N2 blow dry |
| 7 | Clean wafer | remove resist | STS | Recipe: "Planr12" for 30s |
| 8 | PMMA coating | For EBL | Spinner | prebake 180 C-2 min;<br>P.R 495K A4 500RPM-8sec-2500RPM-45s,<br>softbake@180C-1min;<br>P.R. 950K PMMA C2 500RPM-8sec-3000RPM-45s,<br>softbake@180C-1min; |
| 9 | EB expose | Nano shape | Raith 150 | 30KV, 10 um, dose=200~250 uC/cm^2 |
| 10 | Develop | Remove exposed resisit | Ultrasonic bath | Developer: IPA: DI water = 7:3,<br>ultrasonics bath @ 50% power for 50s.<br>Immediately IPA clean for> 3 min, change rinse direction & angle<br>soft N2 blow dry; |
| 11 | Ti deposition | Hard mask | EB evaporator | Ti thickness: 60 nm (depend on etched layer thickness;<br>rate: 0.2 nm/sec) |
| 12 | Ti lift-off | Form hard nano mask | Sonicate | Acetone bath at room-temperature for ~2hr+;<br>Sonicate @ Acetone bath with 40% power for 5min ,<br>DI rinse, soft N2 blow dry |
| 13 | Ion milling nano stack | Form nano stack | Ion milling | Angle @ 10 degree, Current: 9.0A; Etch 3 min. stop 3 min<br>Using reference sample to monitor the etching progress;<br>When ref. sample is clear, change angle to 70 degree and<br>continue etching for 3 more mins |
| 14 | Step measurement | Measure the stack height | Profilmeter | Measure the reference line height. |
| 15 | Remnant SiO2 thickness | Measure the thickness of left thermal SiO2 | Ellipsometer | Measure remnant SiO2 thickness. |
| 16 | PECVD SiO2 | Stack coverage | PECVD | Recipe: SiO2150; thickness is 100nm higher than the stack height ( 352.7A/min) |
| 17 | SiO2 thickness | Measure PECVD SiO2 thickness | Ellipsometer | Recipe: SiO2 on thermal SiO2 on Si;<br>Measure total SiO2 thickness. |

Table 2.1: Fabrication Flow of Nano-scale Magnetic Tunnel Junction Devices.

| Fabrication Flow of Nano-scale Magnetic Tunnel Junction Devices (Cont.) | | | | |
|---|---|---|---|---|
| **Step** | **Name** | **Purpose** | **Tool** | **Description** |
| 18 | Resist coating | For planarization | Spinner | Prebake @ 200C for 5 mins;<br>HMDS 30min;<br>Spin P.R. 1805: spray @ 500RPM for 8s then 4000RPM for 30s |
| 19 | Bake resist | To get a flat surface | Hot plate | 50C for 3min; 105C for 1min |
| 20 | Resist thickness | Measure coating 1805 thickness | Ellipsometer | Recipe: resist on SiO2 on thermal SiO2 on Si;<br>Measure P.R. 1805 thickness. |
| 21 | Resist etch | test resist etching rate | RIE | Recipe: "planr12" for 10 min<br>( Ar 70sccm, CF 47sccm, CHF3 5sccm) |
| 22 | Resist thickness | Measure left 1805 thickness | Ellipsometer | Measure remnant P.R.1805 thickness, calculate the etch rate of P.R. 1805. |
| 23 | Etching resist and SiO2 | remove all resist | RIE | Recipe: "planr12" for 5 min |
| 24 | Measure SiO2 thickness | Monitor left PECVD SiO2 thickness | Ellipsometer | Measure remnant P.R.1805 thickness. This etch step will be repeated till get target remnant SiO2 thickness. |
| 25 | Pattern via of bottom lead | Bottom Lead (BL) opening | MA6 | prebake@115C-1min;<br>P.R. 1813:4000RPM-30sec;<br>softbake@105C-1min;<br>expose(Mask #3):hard contact; 5.5sec.20um;<br>develop: 351:H2O=1:5 for 30sec.<br>Hard bake:120C-1min |
| 26 | BL open | | RIE | Planr12, etch time depends on etched depth. |
| 27 | Resist removal | remove resist | Ultrasonic bath | Acetone ultrasonic 25min, then revomver 1165 ultrasonic for 5min.; DI water rinse, N2 blow |
| 28 | Bilayer prebake | Cover exposed edge of BL | Hot plate | Prebake 5 mins @ 200C |
| 29 | SF5 coating | For better lift-off | Spinner | 500RPM, 10s; 3500RPM 40s; softbake @180C for 5mins |
| 30 | Resist coating | For better lift-off | Spinner | P.R. 1813, 4000RPM 30s; soft bake @ 105C for 1 min |
| 31 | BL coverage pattern | Cover exposed edge of BL | MA6 | Mask #5, SiO2 |
| 32 | Develop | Form pattern | Web bench | CD-26 for 1 min 10sec (SF5); DI water rinse;<br>Oriel expose for 15sec(easy to lift-off);<br>Hard bake 1 min @ 120C |
| 33 | PECVD SiO2 | Cover exposed edge of BL | PECVD | Recipe: "SiO2150"; thickness: 50nm |
| 34 | Lift-off | Remove SiO2 on the BL and the stack | Web bench | Remover 1165 bath@ 65C for 1hr 30 min,<br>sonicate for 20 min;<br>DI water rinse and N2 blow |

Table 2.1(cont.): Fabrication Flow of Nano-scale Magnetic Tunnel Junction Devices.

| Fabrication Flow of Nano-scale Magnetic Tunnel Junction Devices (Cont.) | | | | |
|---|---|---|---|---|
| **Step** | **Name** | **Purpose** | **Tool** | **Description** |
| 35 | Bilayer prebake | Top lead (TL) patterning | Hot plate | Prebake @ 200C for 5 mins. |
| 36 | SF5 coating | For better lift-off | Spinner | Spray@500RPM, 8s; 3500RPM 40s;<br>softbake @ 180C for 5mins |
| 37 | Resist coating | For better lift-off | Spinner | P.R. 1813, 4000RPM 30s;<br>softbake @ 105C for 1 min |
| 38 | Top lead (TL) expose | TL patterning | MA6 | Mask #4; hard contact; 5.5 sec. 20 um |
| 39 | Develop | Form TL pattern | Web bench | CD-26 for 1 min 10 sec (SF5); DI water rinse;<br>Oriel expose for 15sec(easy to lift-off);<br>Hardbake @ 120C for 1 min. |
| 40 | Ion milling | Remove oxidized metal suface | Iom milling | Angle @ 0 degree for 3 mins |
| 41 | TL Depostion | Cover TL | Shamrock | CWetching 12 mins; Cover Ta 5nm/Cu100nm/Ta8nm |
| 42 | Lift-off | lift-off | Web bench | 1165 bath@65C for hrs, sonicate@50% power till it is clean;<br>DI water rinse and N2 blow |

Table 2.1(Cont.): Fabrication Flow of Nano-scale Magnetic Tunnel Junction Devices.

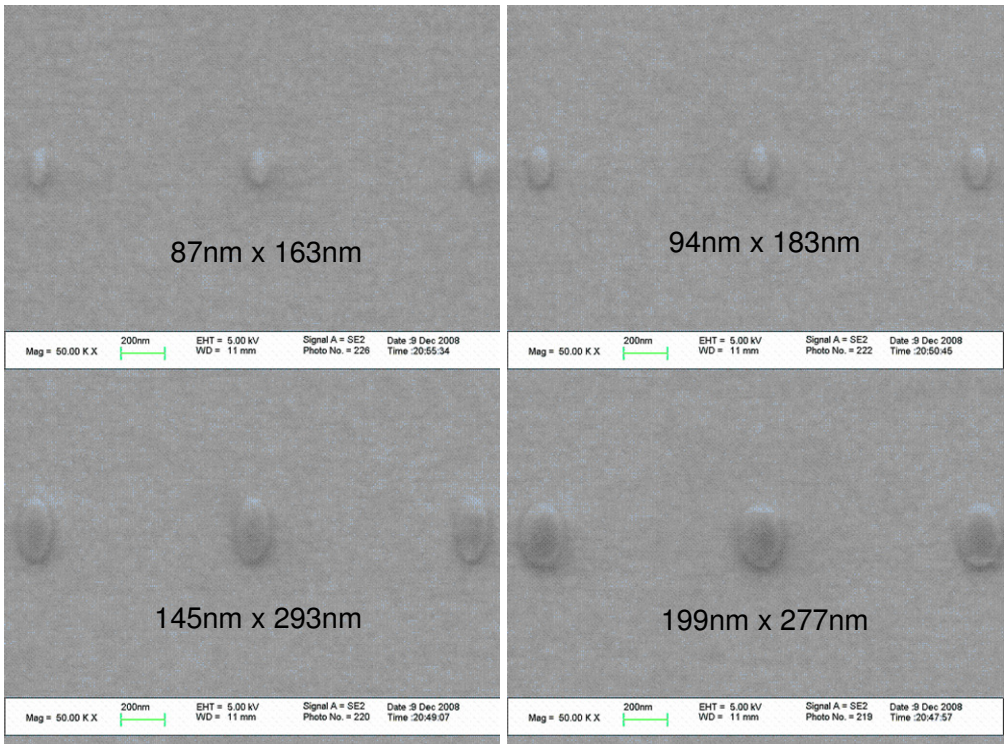


Fig. 2.11 SEM images of nanometer-scale patterns after Ti hard mask lift-off (images taken after step 12 of table 2.1).

# Chapter 3 Magnetic Tunnel Junction based Spintronic Logic Devices

As discussed in the section 1.2.3, spintronic logic devices are promising to replace traditional semiconductor logic devices with advantages of non-volatile, small scale, low power consumption. However, current study mainly uses MTJ cell to replace CMOS devices, which shows limited advantages of spintronic logic devices. In this study, systematic study has been done on STT operated MTJ-based logic devices and circuits, which includes 1) basic MTJ logic cell with three inputs; 2) a STT MTJ-based spintronic logic design that realizes direct communication between two or more MTJs; 3) a three-MTJ logic unit; 4) a design of an Arithmetic Logic Unit (ALU), a fundamental computation unit.

## 3.1 Basic MTJ logic cell with three inputs

A single MTJ with three inputs (shown in Fig.3.1a) can realize fundamental logic functions such as AND, OR, NAND, NOR and Majority. This three-input MTJ logic cell was developed from our previous two-input designs [28,35] with the advantage of instant turn-on without a pre-set step. As shown in the schematic drawing, the MTJ is located in between the top and bottom electrodes, which connect to three input terminals on each side. The logic states "1" ("0") for input is defined as the positive current that flows from the input terminal into the MTJ (from the MTJ to the input terminal). Each input current amplitude ($I$) is larger than the critical switching current ($I_c$) of the MTJ. The logic "1" ("0") of the output is defined as the high (low) voltage across the MTJ. For functions

AND or OR, input terminals A, B, C are used while the top electrode is grounded, as shown in Fig.1(a). When the total input current is positive, the electrons are flowing from the free layer to the fixed layer. Since the total current is larger than the switching current of MTJ cell, due to the spin transfer torque effect, the free layer will be switched antiparallel to the fixed layer. Consequently, the output resistance is high, which is logic "1". On the other hand, when the total input current is negative, the electrons are flowing from the fixed layer to the free layer. If the device starts in the antiparallel state, the polarized electrons will exhibit a torque on the free layer that will cause it to align parallel to the fixed layer. In this parallel state, the output resistance is low, which corresponds to logic "0". As shown in the formula in Fig. 3.1(a), input C can act as a control signal. When C=0, the logic cell acts as AND gate; while C=1, it acts as OR gate. Fig. 3.1(b) shows the HSPICE simulation results of AND and OR function for a basic MTJ logic cell. The detailed HSPICE model can be found in ref. [36]. In the simulation, the high and lower resistances of MTJ are 1008 Ω and 288 Ω, respectively. The critical switching current of the MTJ is 346 μA with a thermal stability factor of 60. The input current for A, B, and C is 400 μA with a 10ns pulse width. NAND, and NOR functions can also be realized by injecting the current into the D, E, and F electrodes and reversing the ground connection.

The engineering constraint on the three-current-input MTJ is that $3I_{in} < I_{breakdown}$. This criterion could be relaxed when we consider two factors. First, the current sources would be implemented using CMOS. These devices would have a natural tendency to saturate as their $V_{ds}$ drops due to the increased voltage across MTJ when all three current

sources are in the same direction. The result is that the three current sources would never reach $3I_{in}$ when they are all in the same direction. Second, the three-current-input MTJ

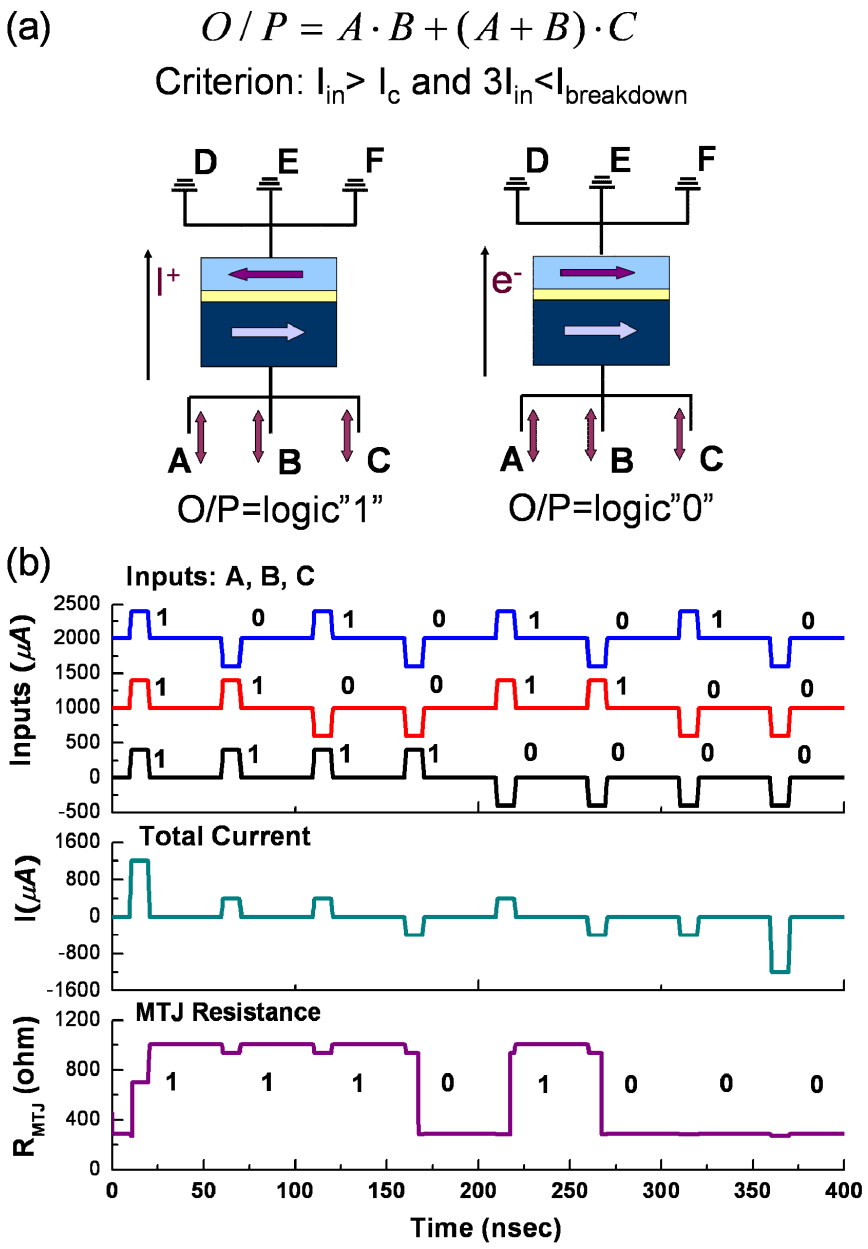


Fig.3.1 (a) Schematic drawing of three-input basic MTJ logic cell with its criterion and logic functions. (b) HSPICE simulation result of this basic MTJ logic cell: (upper) input signal A,B,C; (middle) total input current; (bottom) MTJ resistance. C acts as control signal. When C is 1, OR function is performed. When C is 0, AND function is performed.

design could be modified by using MTJs as inputs to replace the direct current inputs. Such a design was recently proven experimentally [37]. By using MTJs as inputs, the breakdown current criterion would be reduced from $3I_c$ to only slightly over $I_c$.

## 3.2 Communication between MTJ logic cells

As discussed in the introduction section, MTJs usually operate independently of each other [38] and only compose a small portion of the whole circuit which is dominated by semiconductor components. In this paper, we propose a novel design of a key spintronic component, which can realize the direct communication between two or more MTJ logic cells. As shown in Fig. 3.2, a nano-magnetic-channel (NMC) can act as a communication channel that controls the transfer of logic information between two or more MTJ cells without any semiconductor component.

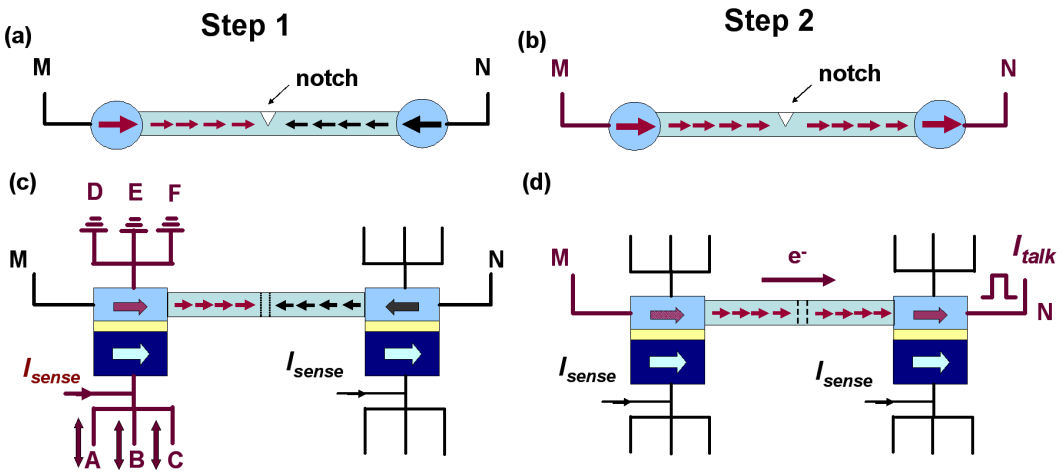


Fig.3.2 Schematic drawing of the operation of nano-magnetic-channel (NMC). (a) and (b) are top views; (c) and (d) are side views. In step 1 when the input MTJ (left MTJ) is programmed by its inputs, shown in (a) and (c). In step 2 when the current is driven down the NMC, the logic data is transferred to the output MTJ (right MTJ) through domain wall propagation driven by a pulse current, $I_{talk}$, shown in (b) and (d).

In Fig. 3.2, each MTJ cell has the same structure as discussed in the previous section. The fixed layer of these two MTJ cells has the same magnetization direction. The inputs for each MTJ cell control the magnetization of its free layer (logic state of each MTJ cell) individually. An NMC connects the two free layers. When the two free layers have opposite magnetization, a domain wall will be formed in the NMC.

The operation of the proposed NMC is based on current-driven domain wall movement, which has been studied and demonstrated by several groups [39-45]. Two additional electrodes, M and N, are connected at the far ends of the two free layers of MTJ cells, as shown in Fig. 3.2. A pulse current across the electrodes M and N is used to drive the domain wall propagation along the NMC. A notch in the middle of the NMC acts as a strong pinning site for the domain wall movement. The pinning potential of the notch can be tuned by altering the shape and size of the notch [46-48]. This is used to control the threshold current of the channel [49], which provides reliable and predictable operation.

Fig. 3.2 shows the two-step operation of this twin MTJ system. First, the left MTJ cell, which is called the input MTJ, is programmed by its inputs when all other inputs are floating (Fig. 3.2(a)). Since no current flows through the channel, there is no domain wall propagation along the NMC and the two MTJ cells are magnetically isolated. When the free layer in the input MTJ is set to antiparallel to the free layer in the output MTJ (right MTJ), a domain wall is formed and pinned near the notch. Then in the second step, a pulse current ($J_{talk}$) is applied from electrode N to electrode M, while keeping the other electrodes floating. The electrons flow from the free layer of the input MTJ and are

polarized by the local moment. These polarized electrons enter the NMC from its left side, and generate a torque on the moment of the right side of the NMC. When $J_{talk}$ is larger than $J_{th}$, the domain wall is propagated through the NMC and switches the free layer in the output MTJ (Fig.3.2(b)). Therefore, the logic state of the input MTJ is transferred to the output MTJ. The direction of the current across NMC is fixed, and electrons always flow from input MTJ to output MTJ to drive the domain wall propagation. When electrons flow from the input MTJ to the output MTJ, there will be back scattering of the electron spins from the output MTJ. Because the freelayer of the input and output MTJ as well as the NMC are the same material, the back scattering effect will increase the critical current for the domain wall propagation, but will not change domain wall propagation direction.

The NMC can also connect one input MTJ to two output MTJ cells. The threshold switching current $J_{th}$ in these two branches of nano-magnetic-channel can be designed to be equal. Therefore, with $J_{talk} > J_{th}$, both free layers in the output MTJs can be switched, and the logic information from the input MTJ propagates to both of the output MTJs, which is similar to the fan-out function in traditional semiconductor circuits.

## 3.3 MTJ-based basic logic unit

A basic logic unit is shown in Fig. 3.3 (a). It is composed of three MTJ cells connected with two NMCs. The center MTJ is the output of the basic logic unit, and is connected electrically with the rest of the circuit. The outer MTJs are the programmable inputs of the logic unit, and are connected only with the local output via the NMC. The operation of the basic logic unit has two steps. First, one or both input MTJs are

programmed by their inputs, while the other electrodes are floating. Then, one of the NMCs is activated by the control signal ($M_1$- $M'_1$ or $M_2$- $M'_2$) as shown in Fig. 3.3(a), which transfers the data from the input MTJ to the output MTJ.

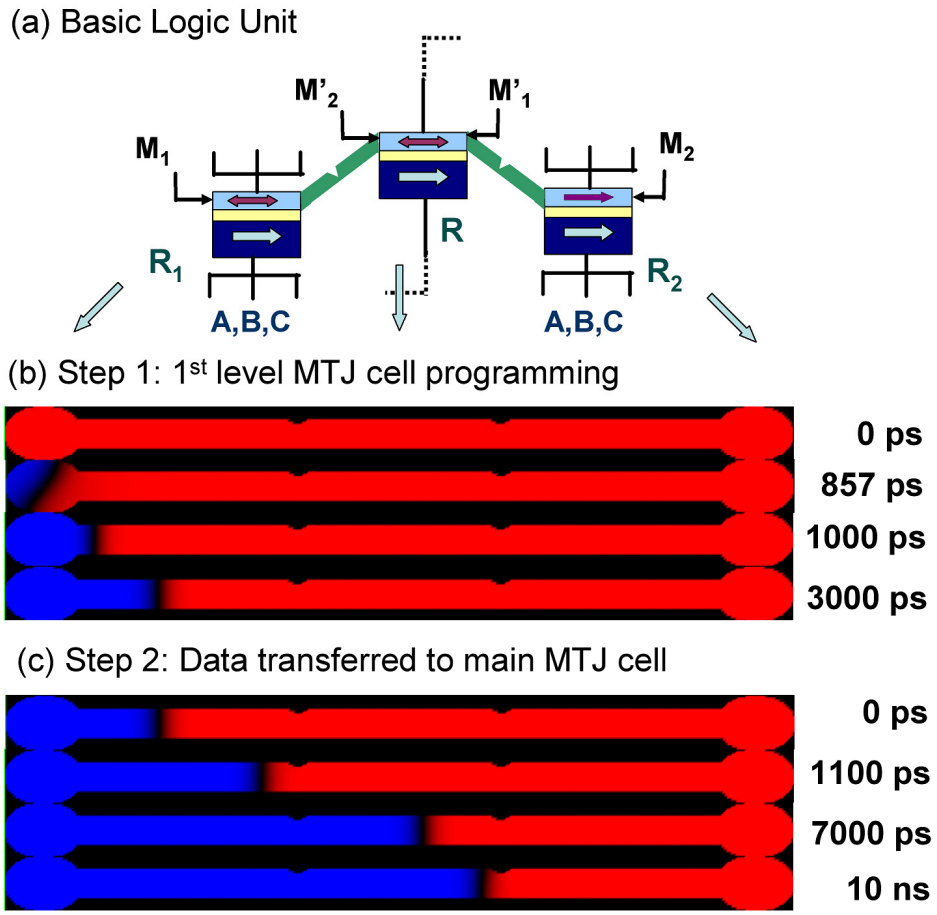


Fig.3.3 (a) Schematic drawing of basic MTJ logic unit with three MTJ logic cells and two nano-magnetic-channels. (b) and (c) show the micromagnetic simulation results of the operation of one basic MTJ logic unit (top view), in which magnetic layers have perpendicular anisotropy.

The operation feasibility of the basic logic unit has been simulated by using LLG Micromagnetics Simulator [50], as shown in Fig. 3.3(b) and (c). The MTJ pillar is ellipse shape with long axis of 70nm and short axis of 50nm. The NMC width is 25 nm. The notch is in the center of NMC with 12nm width and 6nm depth. The cell of the simulation is 2nm×2nm× (layer thickness). The saturation magnetization ($M_s$) for the fixed layer and the free layer are $5\times10^5$ A/m and $6.5\times10^5$ A/m, respectively. The fixed layer and the free layer have perpendicular anisotropy with anisotropy constant of $2\times10^6$J/m$^3$ and $2\times10^5$J/m$^3$, respectively. The spin polarization ratio is 0.6 for both magnetic layers. The simulations were done at zero degrees Kelvin without considering thermal effect. Fig.3.3 (b) and (c) show the top view of the basic logic unit at different times during the simulation. In the first step, Fig.3.3(b), a pulse current (1 ns pulse width) is applied through the input MTJ. When the applied current is larger than the critical switching current, the free layer of the MTJ switches from the parallel state (P) to the antiparallel state (AP). The critical switching current density of the input MTJ with a 1ns pulse width is $5.82\times10^8$A/cm$^2$, and $-1.82\times10^8$A/cm$^2$ for P to AP switch and AP to P switch, respectively. Fig. 3.3(b) shows that at the end of the pulse current, the whole pillar switches to AP state. The domain wall propagates along the NMC and stops in between of the pillar at the first notch. In the second operation step, Fig.3.3(c), another current pulse is applied across the NMC, which is large enough to drive the domain wall through the first notch. Moreover, the pulse current is adjusted in order to let the domain wall move through the main MTJ and stop at the second notch. The position of the main MTJ cell is in the middle of two notch structures. To minimize the critical switching current,

the width of the main MTJ cell is the same of the width of the NMC. The critical switching current density to drive the domain wall propagating through the main MTJ cell is $6.65\times10^{9}$A/cm$^{2}$. The detailed simulation result can refer to another paper [51]. These simulated current densities are fairly large without considering thermal effect. Various techniques could be employed to reduce the current density such as composite free layer which has been shown to reduce the current density by a factor of 2-3 [52-55].

## 3.4 Spin transfer torque based spintronic circuit: arithmetic logic unit (ALU) design

Based on the above proposed basic logic units, a spintronic circuit is proposed to act as an ALU. An ALU is a fundamental building block of the central processing unit (CPU) of a computer. ALU design varies with different applications, however most ALUs can perform the basic operations, such as addition, subtraction, AND, NOR, OR, XOR. In the spintronic ALU circuit that is proposed in this paper, there are six basic logic units (constructed of twenty MTJs) together with two sense amplifiers, as shown in Fig. 3.4. The sense amplifiers are used to convert the signal from a resistance into a voltage signal, which is compatible with the inputs of the next circuit. The main MTJ cells in each logic unit are: $R_1$, $R_2$, $R_3$, $R_4$, $R_5$, $R_6$. The status of each main MTJ cell will be controlled by the input MTJ cells (or reference MTJ cells) in each logic unit through an NMC. These input MTJ cells are: $R'_1$, $R''_1$, $R'_2$, $R'_3$, $R'_4$, $R'_5$, $R'_6$, which are controlled by one or more current inputs: A, B, and C. The $R_L$ and $R_H$ are reference cells, which have a fixed low and high resistance, respectively. Each NMC is controlled by one or more control signals: $M_1$-$M'_1$, $M_2$-$M'_2$, $M_3$-$M'_3$, $M_4$-$M'_4$, and $M_5$-$M'_5$. Table 3.1 summarizes the setting of the

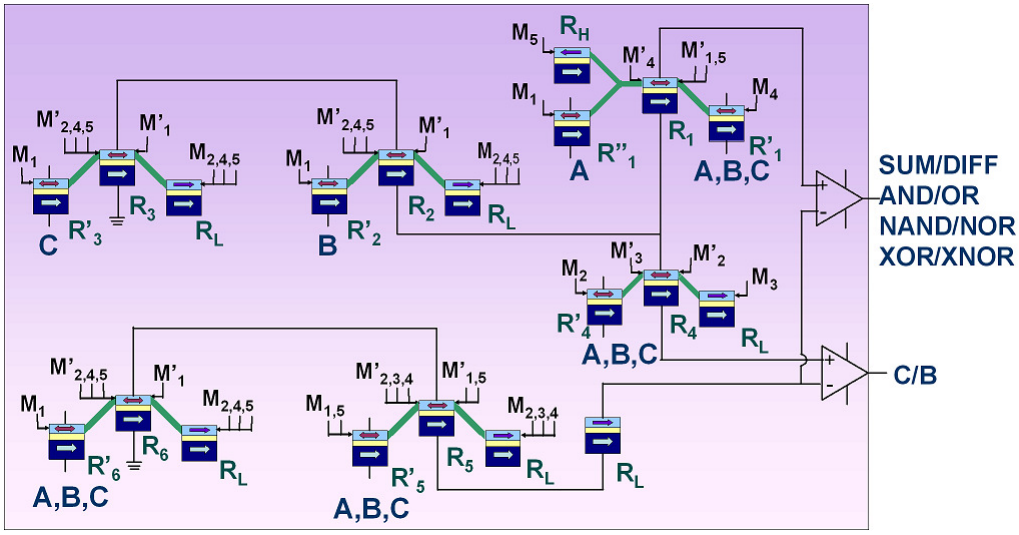


Fig.3.4 The Arithmetic and Logic Unit (ALU) design with twenty MTJ logic cells operated by spin-transfer torque, together with two sensing amplifiers. A,B, and C are inputs for MTJ cells. The NMC, shown in green, realizes the communication among the MTJ cells. The control signal for NMC is shown in $M_1$ ($M'_1$)~$M_5$($M'_5$).

| | A | B | C | $M_1$ | $M_2$ | $M_3$ | $M_4$ | $M_5$ |
|---|---|---|---|---|---|---|---|---|
| SUM | 1/0 | 1/0 | 1/0 | **1** | 0 | 0 | 0 | 0 |
| DIFF | 1/0 | 1/0 | 1/0 | **1** | 0 | 0 | 0 | 0 |
| CARRY | 1/0 | 1/0 | 1/0 | 0 | **1** | 0 | 0 | 0 |
| BORROW | 1/0 | 1/0 | 1/0 | 0 | 0 | **1** | 0 | 0 |
| AND | 1/0 | 1/0 | 0 | 0 | 0 | 0 | **1** | 0 |
| OR | 1/0 | 1/0 | 1 | 0 | 0 | 0 | **1** | 0 |
| NAND | 1/0 | 1/0 | 0 | 0 | 0 | 0 | 0 | **1** |
| NOR | 1/0 | 1/0 | 1 | 0 | 0 | 0 | 0 | **1** |
| XOR | 1/0 | 1/0 | 0 | **1** | 0 | 0 | 0 | 0 |
| XNOR | 1/0 | 1/0 | 1 | **1** | 0 | 0 | 0 | 0 |

Inputs A, B, C: logic "1"=+I; logic "0" = -I;
Control signals $M_1$, $M_2$, $M_3$, $M_4$, $M_5$: logic "1"=on, logic "0"=off

Table 3.1: The inputs (A,B,C) and control signal ($M_1$~$M_5$) of the NMC for each logic function in ALU circuit.

inputs and the control signals for individual logic function. For input, A, B and C, logic "1" and "0" are positive and negative current, respectively. "1/0" represents for active input with either "1" or "0". For control signals, $M_1$, $M_2$, $M_3$, $M_4$, and $M_5$, the logic "1" and "0" refer to the "on" and "off" of the pulse current applied to the NMC, respectively. For example, in "SUM" and "DIFF" functions, all A, B, and C are active inputs, and the control signal $M_1$ is on while others are off. For the "AND" function, A and B are active inputs, while C set to "0", and the control signal $M_4$ is on, while others are off.

The operation sequence of ALU circuit is shown in Fig.3.5. In the first step, the input MTJ cells are programmed by the current inputs A, B, and C while other electrodes are floating. Next, the control signal is "on" for individual logic function, and the data is transferred from the input MTJ cells to the output MTJ cells in each logic unit. Then, the upper sensing amplifier reads the final output for each logic function. For "SUM", "DIFF", "XOR", "XNOR", "AND", "OR", "NAND" and "NOR" functions, the above three steps are used. For "Carry" and "Borrow" functions, one more data transfer step is needed that is controlled by turning on the control signal only. After that, the lower sense amplifier is turned "on" to read the output. These two additional steps for "Carry" and "Borrow" functions are used in order to minimize the number of MTJ cells in the circuit. By increasing the number of MTJ cells, the last two steps can be removed.

The HSPICE simulations based on a STT MTJ macro-model [36] have been carried out to demonstrate the operation of this proposed ALU. Fig.3.6 shows the simulation results of the SUM/Diff. function. A and B are inputs, and C acts as carry-in, $C_{in}$, or borrow-in, $B_{in}$, for SUM or Diff. function respectively. The input current, the

control current, $M_1$, and the reading current, $I_{read}$, are turned on in sequence as shown in Fig.3.6. First, with input current on, the input MTJs in each basic unit are programmed. Then, with control current on, the data is transferred through NMC. Finally, with $I_{read}$ on, the output voltage of the sensing amplifier switches accordingly. In the simulation, the high and low resistance of MTJ are 2k Ω and 1k Ω. The critical switching current and the input current of MTJ cells are 400 μA and 650 μA. The critical switching current and the control current for NMC are 1mA and 2mA, respectively. The reading current for sense amplifier is 100 μA. All the currents are pulsed current with 10ns pulse width.

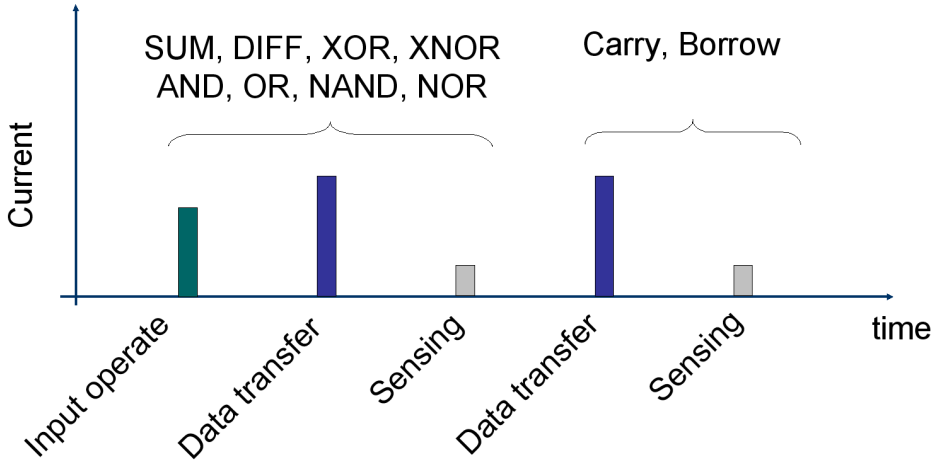


Fig.3.5: The operation sequence of ALU circuit.

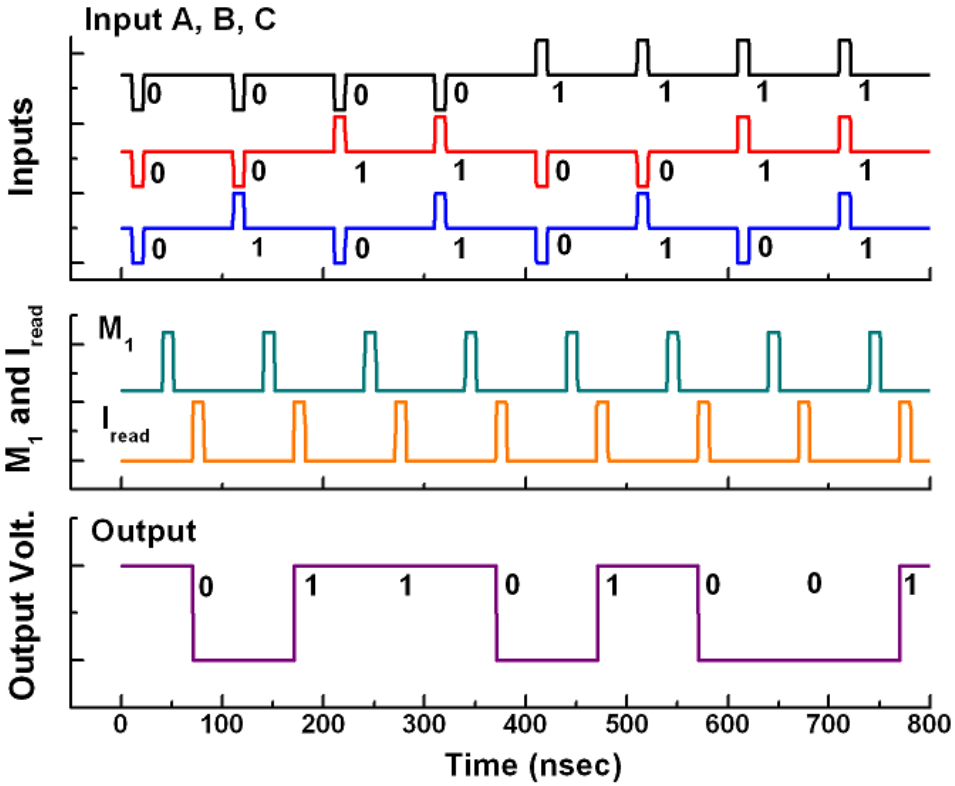


Fig.3.6 HSPICE simulation results of ALU circuit. Upper: input signals, A, B and C. Middle: NMC control signal, $M_1$, and read current, $I_{read}$. Control Signals $M_2$-$M_5$ remain low (off) during the operation. Bottom: the output for SUM/Diff. functions.

The proposed spintronic ALU circuit has advantages on device scaling, compared to the traditional ALU circuit with similar functions. At present device sizes, MTJ based logic circuit may be less energy efficient than their CMOS counterparts. However improvements in *RA* product, *TMR* and device size could change this[56]. The dimensions of MTJ cells can be reduced down to sub 10 nm based on the potential perpendicular MTJ technology [57]. Moreover, the non-volatile nature of the circuit might also be exploited by allowing a paradigm shift away from the Von Neumann architecture. Thereby the power delay product (PDP) could be greatly reduced [58].

## 3.5 Summary

MTJ based spintronic devices and circuit, which is operated by spin-transfer-torque switching, has been proposed and studied. Three input MTJ cell was proposed as the basic logic cell. A basic logic unit that is composed of three MTJs connected by two NMCs was proposed as the building block of spintronic circuits. An advanced spintronic circuit, ALU, was designed and demonstrated based on the above proposed building blocks. Micromagnetic and HSPICE simulations have been done and demonstrated the operation of the basic logic unit and ALU. Based on this work, we believe that maximizing the functionality of the MTJ cells and minimizing the semiconductor components in spintronic circuits can further push the limit of traditional spintronic logic circuits in terms of functionalities and better device scaling.

# Chapter 4 Magnetic Tunnel Junctions with Hybrid Free Layer

## 4.1 Unique Current Switching in MTJs with High Spin Reflection Layer

### 4.1.1 Spin Torque Type in Magnetic Tunnel Junctions

The adiabatic spin torque effect, which is due to the spatial non-uniformity of magnetic properties, has been predicted in theory [59-63] and demonstrated experimentally in magnetic nanowires [64-67]. However, this important spin torque has been rarely concerned in the magnetic tunnel junctions (MTJ) because of its extremely weak effect in conventional MTJs.

The discovery of spin torque transfer (STT) [10-12, 68] has led to a significant advance in the development of spintronic devices. Magnetic tunnel junctions (MTJ), which can have extremely large magnetoresistance, are one of the most important building blocks for spintronics devices, in particular, spin torque transfer magnetic random access memory (STT-MRAM) devices. The operation of the spin torque transfer is realized through the interactions between spin-polarized conduction electrons and local magnetic moments. Novel structures and materials have been studied in order to improve the performance of the magnetic tunnel junctions (MTJs) performances and understand the fundamental physics in spin torque transfer [53-54,69-72]. The concept of the spin torque transfer was first proposed by Slonczewski [10], and Berger [11], in 1996. In conventional MTJs, which have one free layer and one pinned layer, there are two different types of spin torques that can be transferred:

$$\tau = -\beta_{IT}\vec{M}_f \times (\vec{M}_f \times \vec{M}_p) - \beta_{PT}\vec{M}_f \times \vec{M}_p \qquad (1)$$

where $\vec{M}_f$ and $\vec{M}_p$ are the magnetizations for the free and pinned layers, respectively, and $\beta_{IT}$ and $\beta_{PT}$ are two coefficients that depends mainly on spin polarization ratio and saturation magnetization of the magnetic layers. The first term is often called the in-plane spin torque. The second term is called the perpendicular spin torque, which was not explored until very recently [74-77].

The concepts described above are based on the assumption that the free layer has a spatially uniform magnetization along the direction of the current. In novel MTJ structures, however, very often two or more magnetic thin films are used as a composite free layer. This composite configuration results in a spatial non-uniformity of the magnetic properties along the current direction, which leads to additional spin torques. In conventional MTJ devices, those non-uniformity induced spin torques are very weak and, therefore, have been rarely concerned. In contrast, there have been a number of previous works that studied the effect of such spin torques on the dynamics of the current-induced domain wall motion in magnetic nanowires [59-67]. The non-uniformity associated spin torques fall into two different categories: adiabatic and non-adiabatic. The adiabatic spin torque corresponds to the situation where the spatial variation of the magnetization is gradual and the spins of the conduction electrons can follow the direction of the local moments. The non-adiabatic spin torque is the case when there is a sharp change in the magnetization and the spins of the conduction electrons cannot follow the direction of the local moments. One can describe these torques as [63],

$$\tau = -b_{AT}\vec{M}_f \times (\vec{M}_f \times \frac{\partial \vec{M}}{\partial z}) - b_{NT}(\vec{M}_f \times \frac{\partial \vec{M}}{\partial z}), \qquad (2)$$

where the first and second term represent the adiabatic and non-adiabatic spin torque, respectively, $\vec{M}$ is the magnetization within the non-uniform region, $z$ is a space variable in the direction of the current, and $b_{AT}$ and $b_{NT}$ are the coefficients that depend on the spin polarization ratio and the saturation magnetization of magnetic layers of the testing devices. It is worth to note that in this dissertation we follow the use of the names of adiabatic and non-adiabatic spin torques due to a spatial magnetic non-uniformity of the magnetic properties in magnetic layers, which are typically used in the studies of current-induced domain wall motion.

Based on the above discussion, there are four types of spin torques that can be involved in the current-induced magnetization switching process in MTJ devices. The in-plane and adiabatic spin torques act along the same axis within the layer plane, while perpendicular and non-adiabatic spin torques have directions perpendicular to the layer plane. When there are two or more spin torques (with the same type, or different types) along the same axis, the net spin torque exerted on the free layer will be augmented or diminished, depending on the relative orientations of the magnetizations in these magnetic layers, and the relative position of these magnetic layers to the free layer. Many works have been done to study on the enhancement or reduction of two in-plane spin torques in giant magnetoresistance (GMR) or MTJ devices with dual pinned structures [54,78-80] or synthetic antiferromagnetic structures [81-82]. However, there is little study on the effect of the adiabatic spin torque in MTJ devices. Recently, Kim's paper [83] introduces the adiabatic spin torque term in their micromagnetic simulation of MTJ devices with polarization enhancement layers. However, there is no experimental

demonstration of the adiabatic spin torque effect in MTJ devices. More fundamental studies in both theory and experiment on adiabatic spin torques in MTJ devices are required to improve the device performances.

### 4.1.2 MTJ with Hybrid Free Layer Structure

The generation of the adiabatic spin torque was realized through the introduction of the spatial magnetic non-uniformity in a hybrid free layer structure. Such an adiabatic spin torque can substantially promote the current-induced switching process in the MTJ device: the adiabatic spin torque can be larger than the in-plane spin torque, which allows for the switching with a single-polar current under different bias fields. These results have far-reaching implications for the future of high-density STT-MRAM devices.

The key to realize the adiabatic spin torque is the introduction of the spatial magnetic non-uniformity in the hybrid free layer structure by inserting a high spin reflection layer to the free layer side of a conventional MTJ structure. The high spin reflection layer needs to satisfy three criteria to generate the giant adiabatic spin torque. First, the spin reflection layer should have a relatively large saturation magnetization compared to the free layer. In general, the larger the magnetization is, the higher the spin polarization ratio and the amplitude of the adiabatic spin torque are. Second, the exchange coupling between the spin reflection layer and the free layer should be ferromagnetic and relatively weak. Third, the spin reflection layer should have stronger magnetic anisotropy than the free layer. The latter two criteria ensure that the free layer can be switched independently, while the spin reflection layer will not be switched.

It is worth to first discuss about the perpendicular spin torque effect before the detailed analysis of MTJ devices. In recent a couple of years, there are many works on perpendicular spin torque, which can be estimated by fitting the switching phase diagrams. However, there are still some controversial results about perpendicular spin torque, such as if its sign changes with the polarity of applied voltage changes. In our study, the perpendicular spin torque is neglected due to two main reasons: 1) none of the papers about perpendicular spin torque observe unique switching as shown in our devices, which indicates that perpendicular spin torques is not the dominant factor for the unique switching; 2) the amplitude of perpendicular spin torque is still small compared to in-plane spin torque (recent study reports that it can be 10%~30% of in-plan spin torque). Also, the non-adiabatic spin torque, which is the counter part of the perpendicular spin torque in non-uniform magnetization devices, is also neglected in our study.

As a result, only the in-plane spin torque and the adiabatic spin torque are responsible for the magnetization switching in the free layer. Thus the total torque can be written as

$$\tau = -\beta_{IT}\vec{M}_f \times (\vec{M}_f \times \vec{M}_p) - b_{AT}\vec{M}_f \times (\vec{M}_f \times \frac{\partial \vec{M}}{\partial z}), \quad (3)$$

For the data presented below, the hybrid free layer structure is composed of a $Co_{60}Fe_{20}B_{20}$ layer and a thin FeSiO layer. The $Co_{60}Fe_{20}B_{20}$ layer is the free layer, since its magnetization direction controls the MTJ device resistance. The thin FeSiO layer acts as the high spin reflection (HSR) layer. The Fe in the FeSiO layer provides large saturation magnetization and high spin polarization ratio, while the $SiO_2$ dopant ensures the high anisotropy of the film and the weak exchange coupling between the FeSiO film and the

CoFeB free layer. The fixed layer is composed by a synthetic antiferromagnetic structure. The MTJ devices have a multilayered structure as follows: Si substrate / $SiO_2$ (100 nm) / bottom lead / PtMn (20 nm) / $Co_{70}Fe_{30}$ (2.5 nm) / Ru (0.85 nm) / $Co_{60}Fe_{20}B_{20}$ (2.4 nm) / MgO (1.0 nm) / $Co_{60}Fe_{20}B_{20}$ (2.0 nm) / FeSiO (1.5 nm) / top lead. The devices were patterned into an ellipse shape by the use of e-beam lithography followed by an ion milling process. The lateral dimensions are either 130 nm by 162 nm or 149nm by 185nm. The transport measurements were carried out under different currents and bias magnetic fields. The positive current is defined as the electrons flowing from the fixed layer to the free layer. The direction of positive magnetic fields is defined as the direction opposite to the magnetization in the fixed layer. The tunnel magnetoresistance ratio (TMR) ranges from approximately 100% to 130%. The production of the resistance and area (RA) values for the parallel state is 10~12 $\Omega \cdot \mu m^2$. The bias field discussed below is defined as: $H_{bias} = \left( H_{applied} - H_{offset} \right) / H_c$ , where $H_{applied}$ , $H_{offset}$ , $H_c$ are the applied magnetic field, the offset field, and the coercive field, respectively. Note that the offset field originates from the dipole field from the fixed layer. The orange peel coupling from the interface roughness may also contribute the field offset.

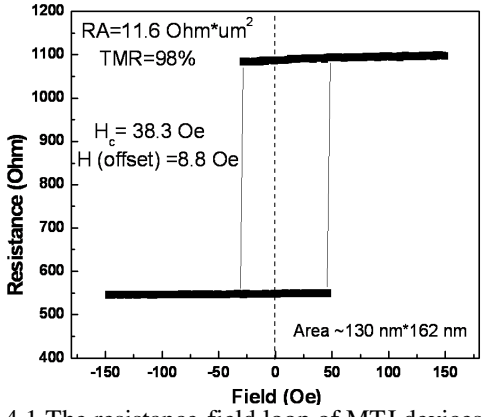

Fig.4.1 The resistance-field loop of MTJ devices

### 4.1.3 Unique Current Induced Switching

Figure 4.2 (a) and (b) shows the transport properties of the MTJ devices with hybrid free layer structures. The current induced switching from antiparallel (AP) state to parallel (P) state under different bias fields is shown in Fig.4.2(a). The MTJ device was first set to AP state as shown in the schematic drawing of Fig.4.2(c). A negative bias field is applied, which lowers the energy barrier of the CoFeB free layer between P and AP states. The positive current is applied with the electrons first polarized by the fixed layer. The majority spins have opposite direction to the CoFeB free layer. Therefore, an in-plane spin torque is exerted on the CoFeB free layer to switch it to the parallel state, as shown in the drawing of Fig.4.2(e). As discussed previously, the CoFeB free layer has smaller anisotropy than FeSiO HSR layer and weak exchange coupling with FeSiO HSR layer. Therefore, CoFeB free layer switches first, while FeSiO remains in its initial state. As the CoFeB free layer switches, the spatial magnetic non-uniformity along the current direction in the hybrid free layer structure increases consequently, which enhances the adiabatic spin torque, through the reflected majority spins. The adiabatic spin torque has the same direction with the in-plane spin torque and helps switch CoFeB free layer to the P state as shown in the drawing of Fig.4.2(e). When the bias field amplitude decreases, the critical current increases as shown in Fig.4.2(a). The switching current under the different bias field in Fig.4.2(a) and (b) is the average value based on multiple measurements. The AP to P switching in MTJs with the hybrid free layer structure is similar to the conventional MTJ devices, which use positive current to switch the free layer from AP to P.

Interestingly, the P to AP switching in the MTJs with hybrid free layer structures is much different from the conventional MTJs. Fig. 4.2(b) shows that the same positive current can also switch the MTJ devices from P to AP state under different bias fields, which cannot be realized with conventional MTJ devices. The MTJ device is pre-set to parallel state as shown in the schematic drawing in Fig.4.2(d). The positive bias field is applied, which lowers the energy barrier of CoFeB free layer between P and AP states. The same positive current is applied through MTJ devices with electrons flowing from the fixed layer to the CoFeB free layer. The polarized electrons have majority spins with the same direction to the CoFeB free layer and the FeSiO HSR layer. Thus the in-plane spin torque, which is exerted by the majority spins coming from the fixed layer, helps keep the CoFeB free layer parallel to the fixed layer as shown in Fig.4.2(f). However, due to the spatial magnetic non-uniformity in the hybrid free layer structure along the current direction, the minority spins that flow through the interface region and the FeSiO HSR layer, are scattered back to the CoFeB free layer. These reflected minority spins exert the adiabatic spin torque, which has opposite direction to the in-plane spin torque as shown in the drawing of Fig.4.2(f). Moreover, during the switching of the CoFeB free layer, the FeSiO HSR layer remains in its initial state as discussed early in this paper. Therefore, the amplitude of adiabatic spin torque increases with the switching of the CoFeB free layer since it is proportional to the level of the spatial non-uniformity in the hybrid free layer. This kind of dynamic spin torque during the switching process due to the spatial non-uniformity of the magnetization is a unique property in the MTJ devices with our proposed hybrid free layer structure, which is different from the MTJ devices with the

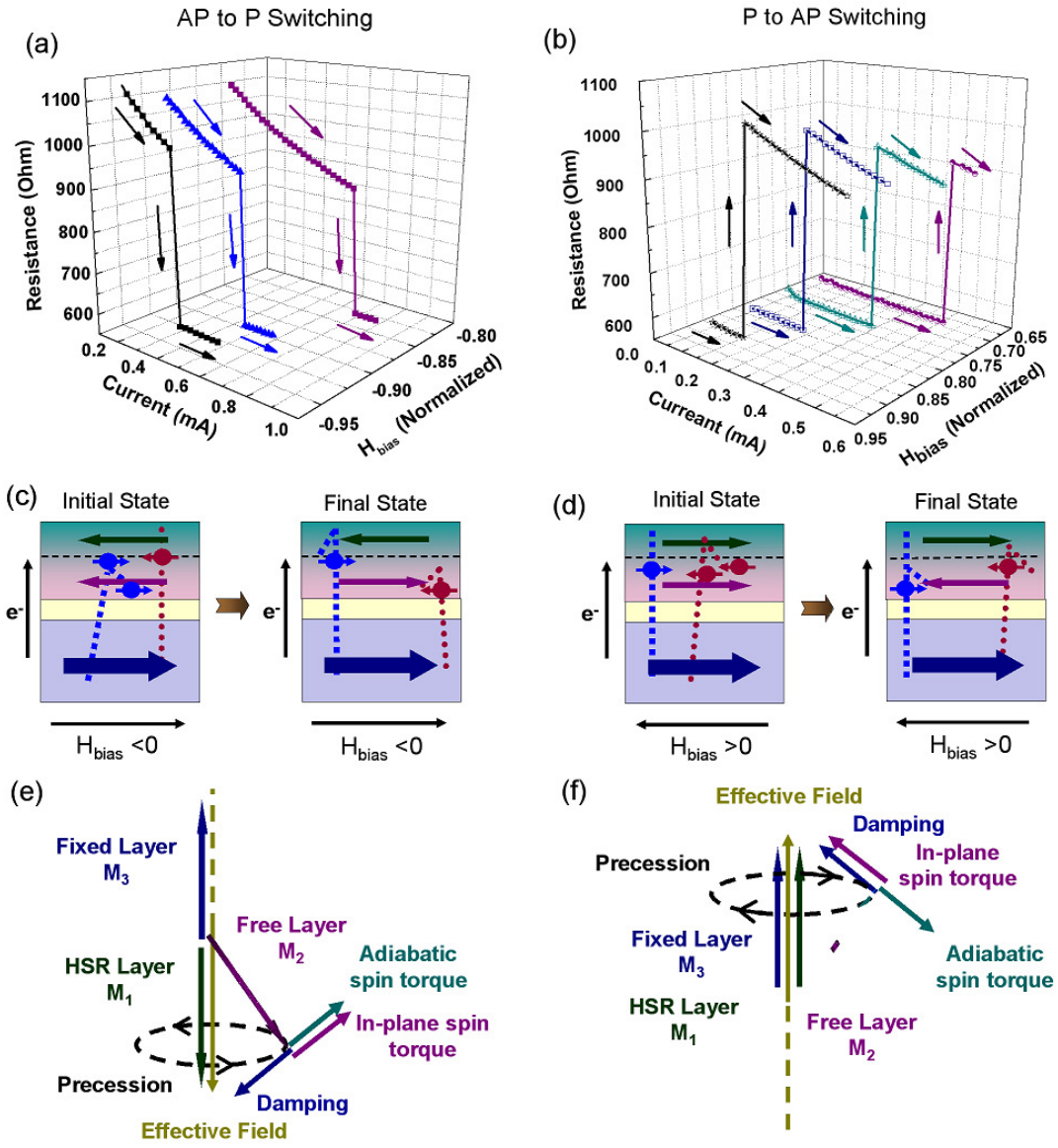


Fig.4.2 The transport behavior of the MTJs with a hybrid free layer structure for AP to P switch (a,c,e) and P to AP switch (b,d,f). Experimental results are shown in (a) and (b). The schematic drawings of the initial state and the final state of MTJ devices are shown in (c) and (d). The drawings of the motion of the free layer moment are shown in (e) and (f).

dual pinned structures in previous reported works [54, 78-80]. As shown in Fig.4.2(f), the adiabatic spin torque competes with the sum of the in-plane spin torque and the damping coming from the effective field. When the applied current is larger than a critical value, the adiabatic spin torque is larger than the sum of the in-plane spin torque and the damping, which induces the unique P to AP switching as shown in Fig.4.2(b). This implies that the adiabatic spin torque increases with the current faster than the in-plane spin torque. This unique P to AP switching with positive current has been observed in a wide range of the bias field from 0.710 to 0.903. As the decrease of the bias field, the effective field, which is dominated by the anisotropy field, becomes larger which results in the increase of the contribution from the damping. Since the adiabatic spin torque competes with the sum of the in-plane spin torque and the damping, the excess of the adiabatic spin torque compared to the in-plane spin torque should become larger with the decrease of the bias field. As shown in the experimental results, when the bias field is reduced to 70% of the coercive field (switching field), the adiabatic spin torque can still be large enough to realize the unique P to AP switching. The final AP state of the MTJ devices is a stable state within the applied current range, and is also stable when the applied current is removed.

The giant adiabatic spin torque effect leads to the single-polar current switching in MTJ devices with hybrid free layer structures under different bias fields. As shown in Fig.4.3, by tuning the bias field, the same amplitude positive current can switch the MTJ device with a hybrid free layer structure in both directions (from P to AP and from AP to P). The switching in both directions is a sharp transition without any intermediate state.

The same transport behaviour can be well repeated in different MTJ devices with two different sizes. The above unique P to AP switching is believed to result from the giant adiabatic spin torque generated by the spatial magnetic non-uniformity in the hybrid free layer structure. At the same time, it is important to exclude any thermal heating effect for such unique P to AP switching. If the thermal heating due to the large current passing through the MTJ device is the cause, a negative current with the same or even smaller amplitude should also induce such P to AP switching, as reported in ref. **Error! Bookmark not defined.**. However, the experimental result shows that even when a negative current three times larger than the positive switching current, the MTJ device remains in P state, which is shown in the Fig.4.4. Therefore the unique P to AP switching with a positive current is not due to the thermal heating effect.

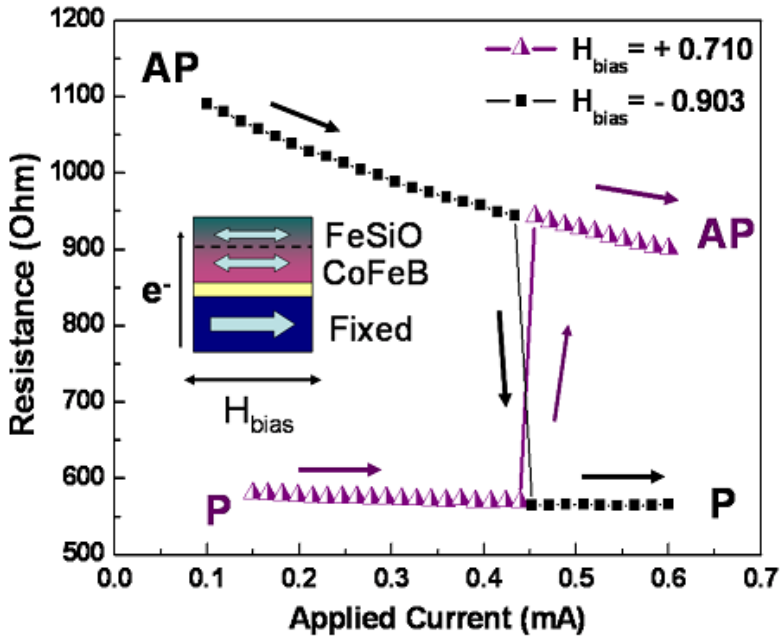


Fig.4.3 Single-polar current induced switching of the free layer of the MTJ devices with a hybrid free layer structure in both directions under different bias field. (Black square curve shows AP to P switch, and purple triangle curve shows P to AP switch.)

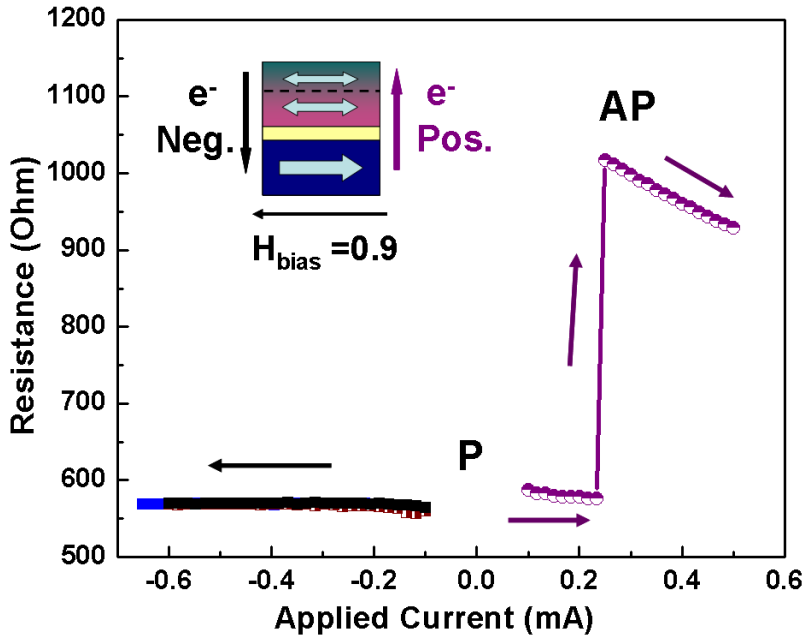


Fig.4.4 The measurement curves of MTJ devices with hybrid free layer with initial parallel state under both positive and negative current in order to exclude the thermal heating effect.

To gain more insight, the FeSiO HSR layer was analyzed to confirm that it indeed satisfied the three criteria to realize giant adiabatic spin torque as mentioned earlier in this paper. First, the HSR layer should have high saturation magnetization ($M_s$) and/or high spin polarization. The X-ray photoelectron spectroscopy (XPS), fig.4.5, shows that Fe is the dominant phase in the FeSiO thin film, and there is no $Fe_2O_3$ peak in the Fe 2p3 XPS spectrum. Si has two phases in FeSiO thin film, silicon oxide and iron Silicide or silicon, as shown in Fig.1s of the supplementary information. The volume fraction of Fe, $SiO_2$ and (Fe)Si is approximate 70%, 15% and 15%, respectively. Based on the TEM images shown in Fig.4s of the supplementary information, the Fe and/or Fe(Si) grains are

surrounded by $SiO_2$ grain boundaries. Besides the dominant phase of Fe, the $Fe_3Si$ phase is also believed to exist in FeSiO film. Both Fe and $Fe_3Si$ [84] have high spin polarization ratio, which enhances the adiabatic spin torque during the current-induced switching process. The second criterion for a proper HSR layer is that there is relatively weak coupling between FeSiO and CoFeB layers. This criterion is satisfied by using $SiO_x$ in FeSiO layer, which diffuses to the grain boundaries and also the interface between FeSiO and CoFeB layers during the post-annealing process. The diffusion of $SiO_x$ reduces the interlayer exchange coupling between FeSiO and CoFeB layers. The third criterion is that FeSiO layer should have higher anisotropy than CoFeB layer so that the CoFeB switches independently with a lower switching current. The magnetic anisotropy constants of the annealed FeSiO and CoFeB thin films were estimated, with the Law of Approach to Saturation (LATS) based on the initial magnetization curves, as 4.0 and $2.0 \times 10^4$ $erg/cm^3$, respectively. The increase of the magnetic anisotropy constant in FeSiO thin film has been studied by other groups [85] and may be due to changes of particle size and percolation effect. Moreover, the damping constant for FeSiO and CoFeB thin films was measured using the ferromagnetic resonance (FMR) method. The effective damping constant of FeSiO and CoFeB films are 0.015 and 0.008, respectively, as shown in Fig.4.6. Therefore, due to the lower anisotropy constant and damping constant, the CoFeB free layer has a lower critical switching current than the FeSiO HSR layer [86]. Thus based on the above analysis, the FeSiO does satisfy all three of the required criteria to realize the giant adiabatic spin torque.

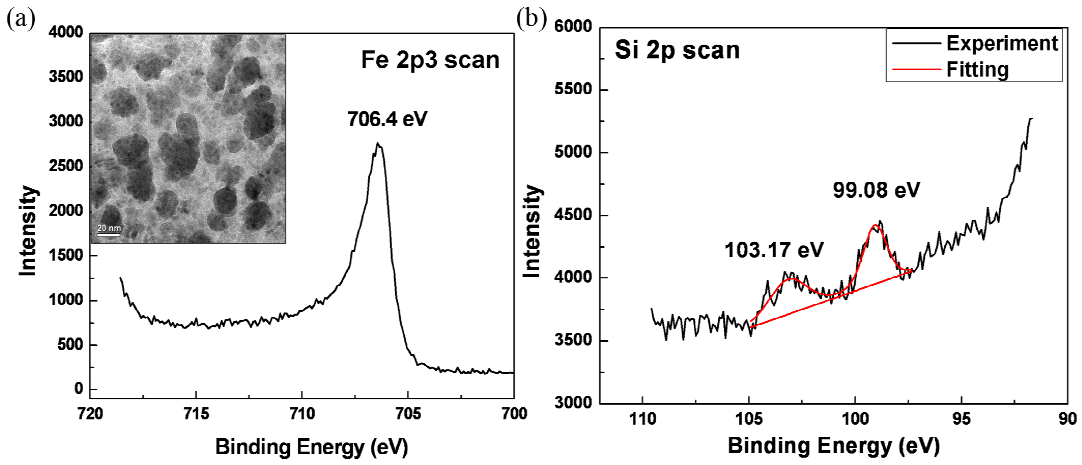


Fig.4.5 X-ray photoelectron spectroscopy (XPS) results of (a) Fe 2p3 scan and (b) Si 2p scan.

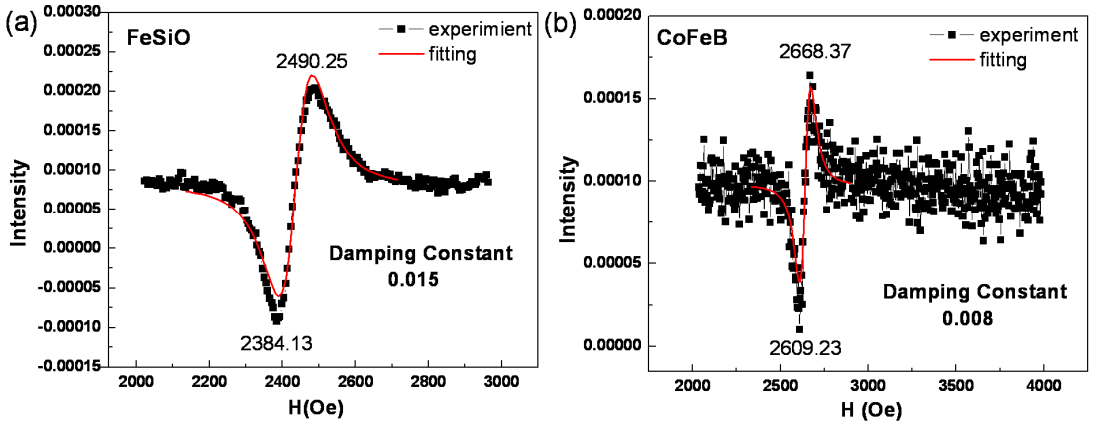


Fig.4.6 The ferromagnetic resonance (FMR) spectra (black curves) for 3nm CoFeB film (a) and 5nm FeSiO film (b). The red curves are the fitting curves.

4.1.4 Simulation based on Macrospin Model

In order to confirm the experimental observations, numerical analysis based on a macrospin model has been done. The motion of the CoFeB free layer moment is described by modified Landau-Lifshitz-Gilbert (LLG) equation, which includes in-plane and adiabatic spin torque terms as shown in the following:

$$\frac{\partial \vec{M}_2}{\partial t} = -\gamma \vec{M}_2 \times \vec{H}_{eff2} - \alpha^* \vec{M}_2 \times (\vec{M}_2 \times \vec{H}_{eff2}) - \beta_{IT2} \vec{M}_2 \times (\vec{M}_2 \times \vec{M}_3) + b_{AT2} \vec{M}_2 \times (\vec{M}_2 \times \frac{\partial \vec{M}_{1,2}}{\partial z})$$

For the FeSiO HSR layer, there is only an adiabatic spin torque term in LLG equation, which is: $\frac{\partial \vec{M}_1}{\partial t} = -\gamma \vec{M}_1 \times \vec{H}_{eff1} - \alpha^* \vec{M}_1 \times (\vec{M}_1 \times \vec{H}_{eff1}) + b_{AT1} \vec{M}_1 \times (\vec{M}_1 \times \frac{\partial \vec{M}_{1,2}}{\partial z})$ . The subscript number 1, 2 and 3 represent the FeSiO HSR layer, CoFeB free layer and CoFeB fixed layer, respectively. $\alpha_{1,2}{}^* = \frac{\gamma \alpha_{1,2}}{(1+\alpha_{1,2}{}^2) M_{s1,2}}$ , $\beta_{IT2} = \frac{\mu_B J P_3}{e d_2 M^2{}_{s2} M_{s3}}$ , $b_{AT1,2} = \frac{\mu_B J P_{2,1}}{e M^2{}_{s1,2} M_{s2,1}}$ are coefficients of the damping, in-plane spin torque and adiabatic spin torque, respectively. γ is the gyromagnetic ratio, α is the Gilbert damping constant, $M_s$ is the saturation magnetization, P is spin polarization ratio, $\mu_B$ is the Bohr magneton, *e* is electron charge, and *J* is the current density, *d* is layer thickness. The X,Y and Z axes are the in-plane easy-axis, hard-axis and out-of-plane direction (current direction), respectively. Based on the macrospin approximation, $\frac{\partial \vec{M}_{1,2}}{\partial z} \approx \frac{\vec{M}_1 - \vec{M}_2}{d^*}$ , where $d^* = \frac{(d_1 + d_2)}{2}$ represents the distance of the magnetization change in the interface region of the CoFeB free layer and the FeSiO HSR layer. The effective field includes the

external field, magnetic anisotropy field, demagnetic field and interlayer coupling field. The saturation magnetization, magnetic anisotropy constant and damping constant used in the simulation are based on the experimental results. The spin polarization ratio of FeSiO and CoFeB is set to 0.55 and 0.40, respectively. Fig.4.7(a) and (b) show the simulation result for AP to P switching with a positive current and a negative bias field (-0.903), which is the same as the experimental setting. The critical switching current density ($J_c$) for CoFeB and FeSiO layers are $0.8\times10^7$ A/cm$^2$ and $6.1\times10^7$ A/cm$^2$, respectively. The simulation value of $J_c$ is about four times larger than the experimental $J_c$ value, which is attributed to the fact that the simulation is performed at zero Kelvin and no temperature effect is considered.

The unique P to AP switching with a positive current and a positive bias field (0.903) is also obtained in the simulation as shown in Fig. 4.7(c). The switching current for CoFeB free layer is $4.4\times10^7$ A/cm$^2$. This simulation result agrees with the experimental observation of the unique P to AP switch. When the adiabatic spin torque term is removed from the LLG equations, such unique P to AP switch cannot be obtained with any current value, which indicates that the giant adiabatic spin torque plays an indispensable role for the unique P to AP switching. At the CoFeB critical switching current, the FeSiO HSR layer does not switch as shown in Fig. 4.7 (d). Since the device resistance is dominated by the relative alignment of the two magnetic layers adjacent to the tunneling barrier, the contribution from the FeSiO HSR layer orientation to the device resistance can be neglected. When a larger current is applied, the FeSiO HSR layer

switches to AP state, while the CoFeB free layer switches back to P state as shown in Fig. 4.7 (e) and (f). However, when the applied current is larger than $10\times10^7$ A/cm$^2$, both

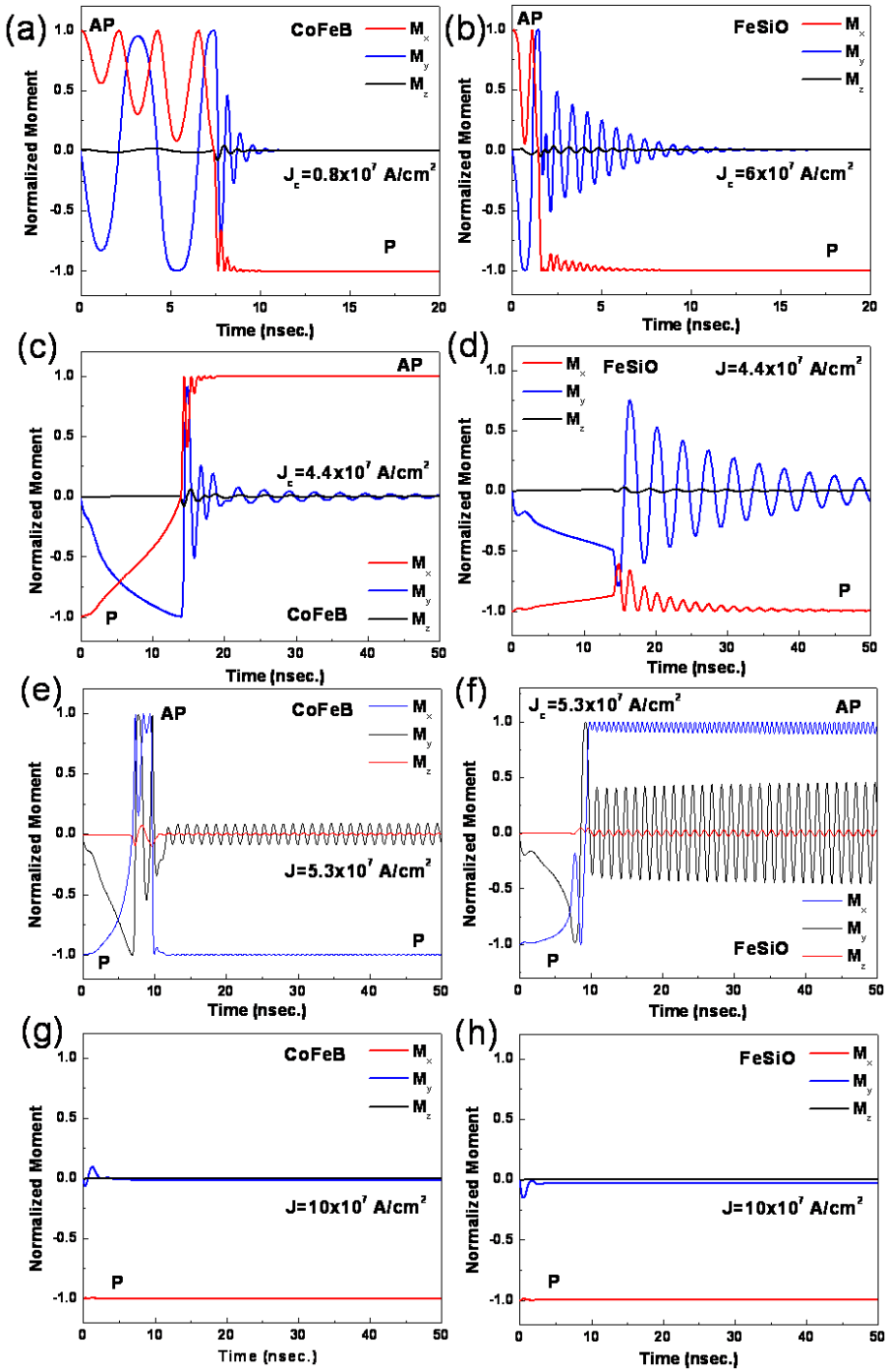


Fig.4.7 Simulation results of AP to P switching (a, b) and P to AP switching (c~h). The transport behavior of the CoFeB free layer is shown in (a, c, e, g) and that of the FeSiO high spin reflection layer is shown in (b,d,f,h). The applied current increases from (c) to (g) and also from (d) to (h). X,Y, and Z direction represent the in-plane easy-axis, in-plane hard-axis, and out-of-plane direction, respectively.

CoFeB free layer and FeSiO HSR layer prefer P state as shown in Fig. 4.7 (g) and (h). This behavior was not observed in the experiment since the current is higher than the break-down current of the MTJ devices. Fig. 4.7 (c)~(h) shows that the unique P to AP switching with a positive current only happens within a window of applied current. Such an operation window for the unique P to AP switching depends on the difference of the spin polarization ratio and the interlayer exchange coupling between CoFeB free layer and FeSiO HSR layer, which was discussed in the first and second criteria of the HSR layer earlier. The simulations show that such an operation window is only obtained with a weak interlayer coupling between the FeSiO HSR layer and the CoFeB free layer. When the interlayer coupling is strong, CoFeB free layer switches together with FeSiO layer, and P to AP switch cannot happen with any positive current.

### 4.1.5 Summary

A new type of MTJ devices that has a hybrid free layer structure was studied. The hybrid structure introduces a spatial magnetic non-uniformity along the current direction, which exerts an adiabatic spin torque on the free layer. Through the optimization of the properties of the hybrid structure, we demonstrated an adiabatic spin torque that is surprisingly larger than the conventional in-plane spin torque. Such a giant adiabatic torque can plays a critical role in the switching of the magnetization in the free layer. In particular, this torque allows for both the AP to P and P to AP switching operations with a single-polar current under different bias fields. In addition, the experimental results were confirmed by numerical simulations that were based on a macrospin model.

## 4.2 Intermediate State in Magnetic Tunnel Junctions with Composite Free Layer

Spin angular momentum transfer from a polarized current to a ferromagnetic layer/pillar was first predicted by Slonczewski [10] and Berger [11] theoretically, and later experimental demonstrated by several groups [68,87-94]. The current-induced-magnetization-switching (CIMS) has advantages of device scaling compared to the traditional field-induced switching, which boosts the development in the field of magnetic random-access memory (MRAM) and the spintronic logic devices. One of the main challenges by using CIMS mechanism is the high critical switching current density, normally in the order of $10^7$ A/cm$^2$. On the other hand, several groups reported the existence of an intermediate state or inhomogeneous switching in CPP GMR structure by the spin-polarized current [68,87, 95-97]. Multi-domain structure was formed by polarized current with or without external magnetic field in either free layer or pinned layer. It is important to understand the current-induced switching behaviour in nanoscaled element. And to generate and control reversible intermediate states is one of ways to realize the multilevel spintronic devices such as MRAM. In this study, we discuss the current-driven switching behaviour of large MTJ devices with a composite free layer, with the emphasis on the intermediate state observation. The switching current distribution and reversible intermediate state are also studied.

### 4.2.1 Composite Free Layer Deposition

The composite free layer was studied in our previous papers, which can reduce the critical switching current density [93,98-100] and also improves the switching current

symmetry [101] in the magnetic tunnel junctions. FeSiO was used as nano-current-confined (NCC) structure in the previous work, which was inserted within or besides the free layer. In this work, the composite free layer structure is CoFeB/CoFeB-oxide/CoFeB. The oxide used in this study is $SiO_2$ type oxide with higher dielectric constant.

The CoFeB-oxide layer, which acts as nano-current-confined structure, was deposited by magnetron sputtering method with CoFeB and oxide targets. Similar to FeSiO, the oxide material as well as small element, Boron, prefers to locate at the grain boundary. And CoFe forms the grain core, which is isolated by the B-riched grain boundary. There are two criteria for NCC layer. First, NCC layer should be superparamagnetic, so that it can be easily switched under very small current. Second, NCC layer should be exchange coupled with besides sub-freelayer, so that the switching current can be further reduced.

The magnetic hysteresis loops were measured by vibrating sample magnetometer (VSM) with the field in the film plane. The current-induced magnetization switching loops were measured by four-point measurement tester with bias field along easy-axis of the samples. The initial and final states of MTJs after each current sweep were confirmed by measuring the device resistance using a small current ($2\times10^{-5}$ A) at zero field, and the current pulse width at each point was 200 ms. The devices' sizes were measured by scanning electron microscope (SEM). The switching current density, $J_c$, is calculated by dividing the switching current by average device area.

Fig.4.8 shows the hysteresis loops of CoFeB-oxide single layer with different oxide volume fraction. The total film thickness is fixed at 12 nm. The oxide volume fraction was changed from 10 vol% to 50 vol% by adjusting the sputtering power. By increasing the oxide fraction, both the loop squareness and the film coercivity decrease. The sample with 10 vol% oxide has good squareness, which indicates that the oxide volume is not large enough to completely isolate the CoFe grains and the CoFe grains may switch coherently. With the increase of the oxide fraction to 20 vol%, the decrease of the squareness indicates that part of CoFe grains are exchange-decoupled by the oxide grain boundary, and start to switch gradually. At the same time, the film coercivity decreases with the increase of the oxide fraction, which implies the reduction of the CoFe grain size. Theoretically, with a fixed total film thickness, when the grain size is reduced to a certain value, the film shows superparamagnetic property. This agrees well with our experimental results that when the oxide fraction is larger than 40 vol%, the film became superparamagnetic (insert of fig.4.8).

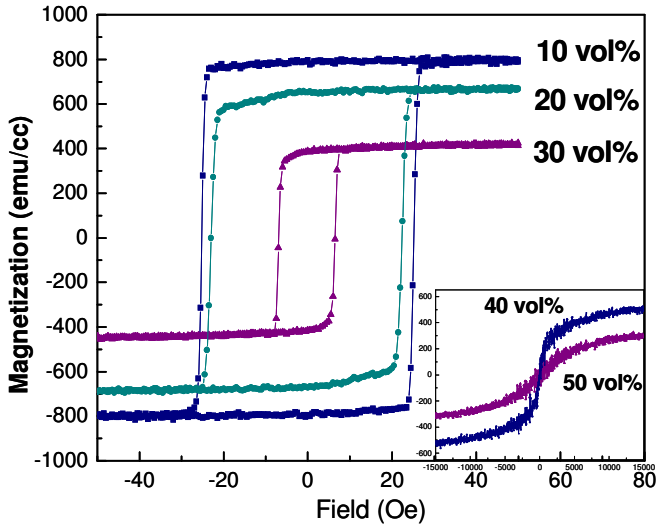


Fig.4.8. Hysteresis loops of CoFeB-oxide single layer samples with different oxide volume fraction. The total film thickness is 12 nm.

The CoFeB-oxide layer should have small thickness in order to achieve relatively low resistance-area (RA) value and at the same time keep its superparamagnetic property. Therefore, the thickness dependent behaviour was also studied with fixed oxide fraction (30 vol%). The sputtering conditions of CoFeB and oxide were kept the same while the sputtering time was varied to get different film thickness. 12 nm CoFeB-oxide film shows clear ferromagnetic behaviour with the coercivity of 7 Oe (Fig.4.8). When the thickness is reduced to 6 nm, the film has a very small remnant squareness and coercivity. By further decreasing the thickness to 3 nm, the film shows superparamagnetic property, as shown in Fig.4.9.

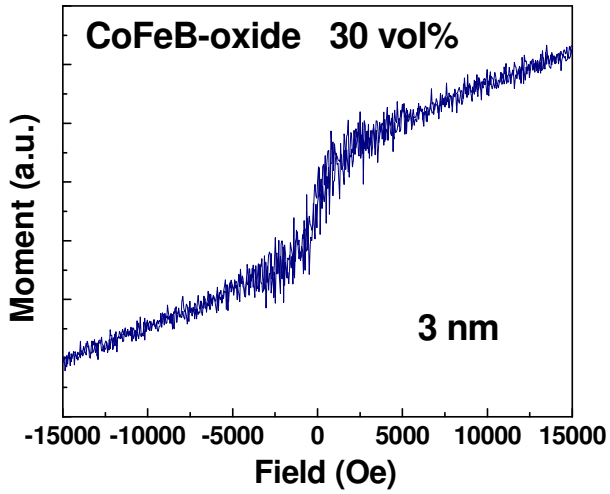


Fig.4.9. Hysteresis loop of single CoFeB-oxide film with 30 vol% oxide and 3 nm thickness, which shows superparamagnetic property at room-temperature.

The sample with full MTJ structure was deposited by the sputtering method. The film structure is: $SiO_2$/Bottom electrode/IrMn/CoFe/Ru/CoFeB/MgO/ composite free layer/top electrode. The composite free layer is: CoFeB 2nm /CoFeB-oxide 30vol% (NCC layer) 3nm/CoFeB 1nm. The sample was patterned by e-beam lithography into 200 nm*600 nm with different shape (bar and ellipse).

### 4.2.2 Current-Induced Magnetization Switching in MTJ with Composite Free Layer

#### *4.2.2.1 Ellipse Shape MTJ Devices*

Fig.3 shows the current-induced magnetization switching curves for the ellipse shape MTJ devices. The switching from antiparallel (AP) to parallel (P) states under different bias fields is shown in Fig.4.10a. A stable intermediate state (IM1) was observed in the switching from AP to P states (Fig.4.10a). With small bias field, the switching from AP to IM1 and IM1 to P were sharp. When the applied bias field changed from the switching field ($H_{sw}$=11.08 Oe) toward the offset field ($H_{offset}$=-8.73 Oe), the switching current density increased, as shown in the dashed line in Fig.3a. With an offset field, the switching from AP to IM1 became gradual, and the switching current density from IM1 to P state is $J_c^{IM1-P} = 5.45\times10^6 \quad A/cm^2$. Although the TMR value in our MTJ devices is relatively low compared to other group's result, the critical switching current density is comparable [102], which shows the effect from nano-current-confined structure. The intermediate state appeared at the positive applied current may be due to the multi-domain structure, which is expected for the large size devices. Similarly to the result in the paper of Jiang et al [96], the intermediate state was induced by the multi-domain

structure in the free layer. And current-induced resistance oscillation among AP, P, and IM states was reported under an intermediate external field [96].

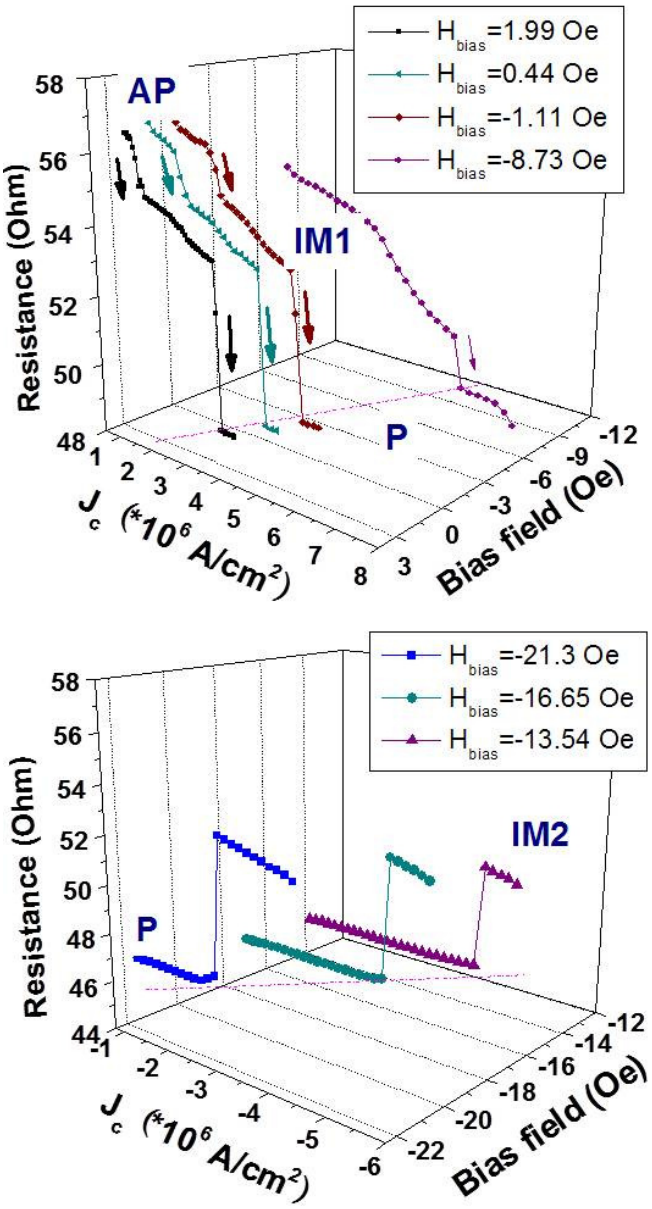


Fig.4.10. Current-induced magnetic switching (CIMS) curves of ellipse shape MTJ device with composite free layer under different bias fields. (a) switching from AP state to P state with IM1 state; (b) switching from P state to IM2 state with negative applied current

Different from the switching from AP to P, with negative applied current, only switching from parallel state to another intermediate state (IM2) was observed (Fig.4.10b). Interestingly the intermediate state, IM2, is stable with large negative current. The switching current density at the offset field is estimated to be $J_c^{P-IM2} = 5.50 \times 10^6 \quad A/cm^2$. The switching mechanisms in two current directions are different, which results in two different intermediate state configurations. And the study on switching current distribution, which is discussed in the following section, also shows the two different switching mechanisms of the intermediate states. The detailed discussion will be addressed in another paper.

*4.2.2.2 Bar Shape MTJ Devices*

Fig.4.11a and Fig.4.11b show the major and minor curves of current-induced magnetization switching in the bar shape MTJ devices. Similar to the ellipse shape samples, the intermediate states were observed in both current directions. With positive applied current, the electrons fly from the fixed layer to the free layer. The device first switched from AP state to IM1 state, then switch to P state (Fig.4.11a). The switching current density from IM1 to P states is $J_c^{IM1-P} = 4.20 \times 10^6 \quad A/cm^2$, which is smaller than that in the ellipse shape samples. With a negative applied current, IM2 state is the stable state with large applied current. Only the switching from P to IM2 states was obtained. Fig.4.11b shows the current-induced switching between AP to IM1 (or IM2) states. It is interesting to note that when the device was initially at IM1 state, with decreasing the applied current, IM1 state switched back to AP state at a small positive

current. And with further increasing the negative current, the device switched from AP to IM2 state, and kept at IM2 state at the large negative current. The spin transfer torque does not contribute the switching from IM1 to AP state at low positive current, because P state is preferred with positive current. The dipole field between the free layer and the pinned layer may also induce the multi-domain structure in either the free layer or the pinned layer, which was reported by Yang et al [95]. When the applied field is smaller than the dipole field, the AP state is preferred, which has the lowest energy. And when the applied field is larger than the dipole field, the P state is preferred. In our measurements, the applied field is -7.33 Oe, which is smaller than the dipole field. Therefore IM1 state switched to AP state at a small positive current.

#### 4.2.2.3 Distribution of Switching Current Density

The switching current density under different bias fields was studied by multi-scan under the same conditions for ellipse shape MTJ devices. Fig.4.12a and Fig.4.12b show the current distribution of the switching from IM1 to P state and P to IM2 states under different bias fields, respectively. The average standard deviation of the switching current was 18% for the switching from IM1 to P, and 10% for the switching from P to IM2. The large difference between the switching current distributions in two current directions indicates that the switching mechanisms are different for two stable intermediate states.

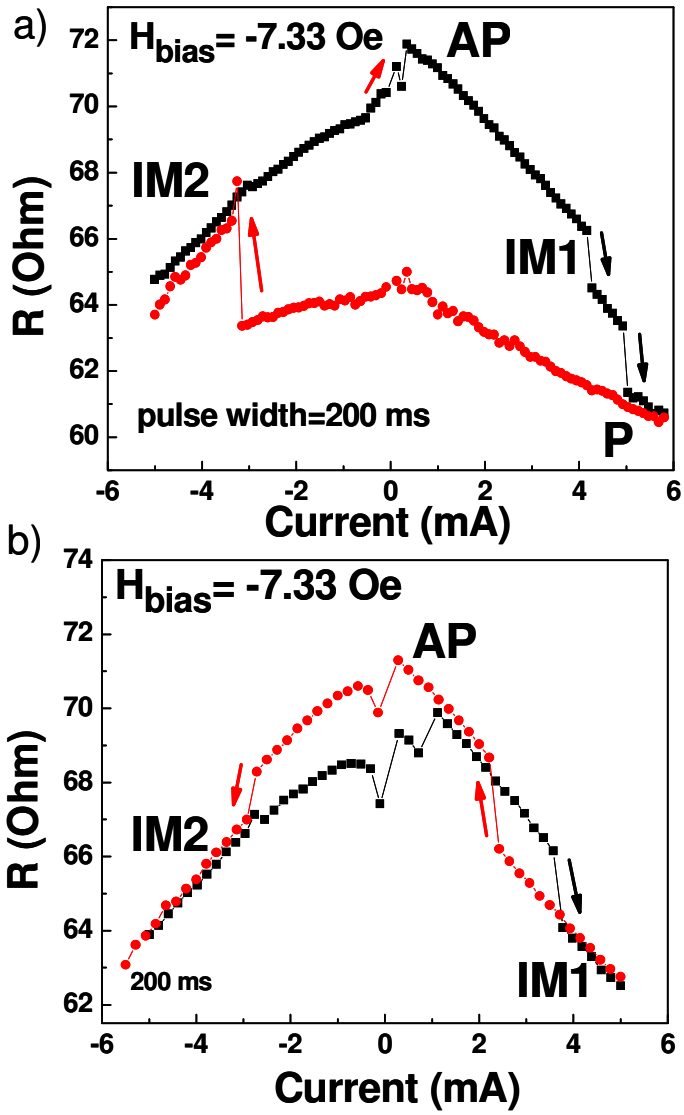


Fig.4.11. Major (a) and minor (b) loops of current-induced switching in bar shape MTJ device with composite free layer.

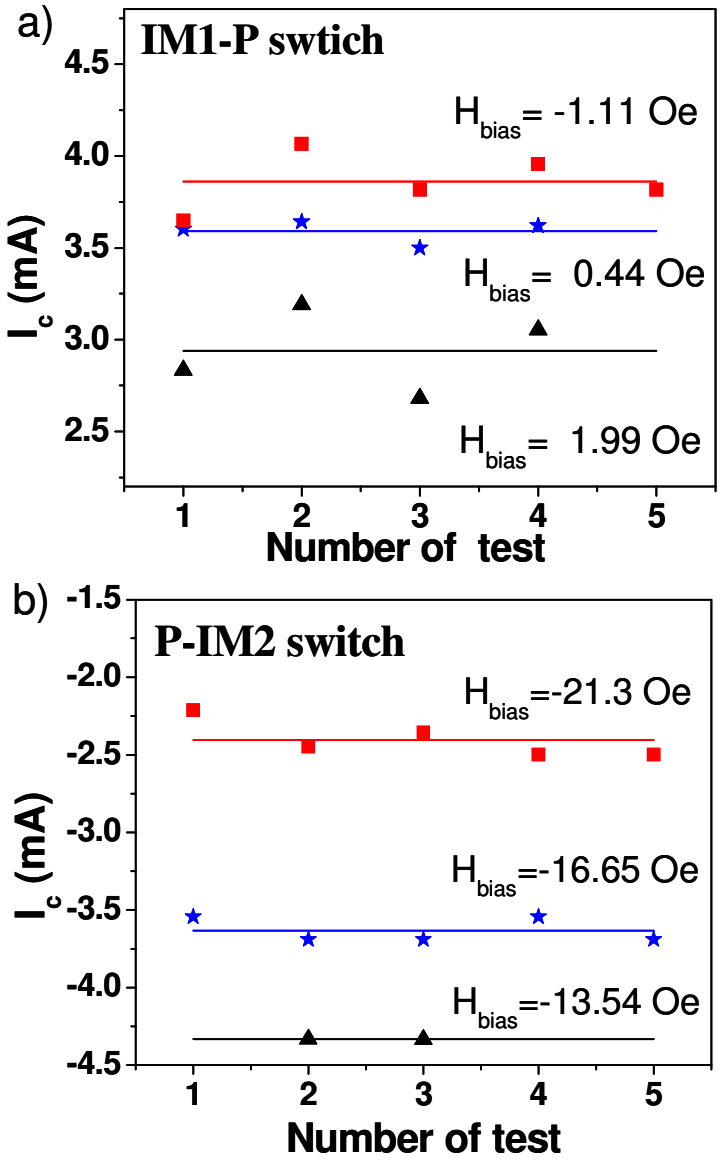


Fig.4.12 Switching current distribution for (a) IM1-P switch and (b) P-IM2 switch under different bias fields. The large difference of the switching current distribution indicates the different switching mechanisms in two intermediate states.

4.2.2.4 Reversible Intermediate States

In addition to the stable intermediate states, the reversible intermediate states were also observed with small applied current. Here we define the stable intermediate state as the resistance state, which does not switch automatically to P or AP state after removing the applied current. And the reversible intermediate state is the instable resistance state, which switch automatically to P or AP state after removing the applied current, as shown in Fig.4.13. The reversible intermediate states were only observed around small applied current in both directions. The formation of these reversible intermediate states may due to the domain nucleation induced by the polarized current. The oscillation between two states is different from the electrical noise, which is one order smaller than the measurement value. And the oscillation only appears around the small switching current.

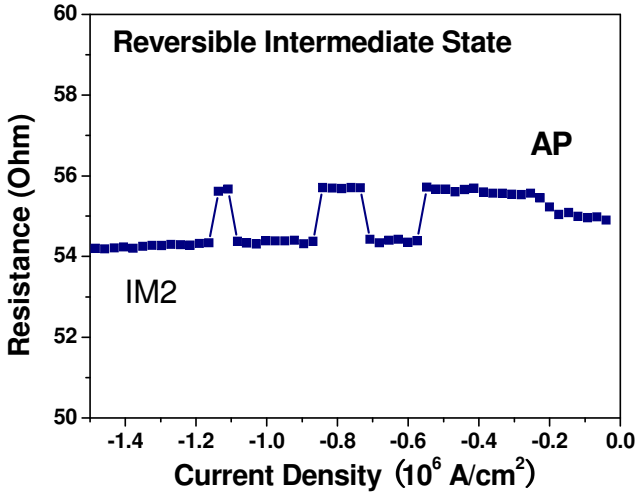


Fig.4.13 Reversible intermediate state was observed at small negative applied current, which may be due to the domain nucleation.

### 4.2.3 Summary

The current-induced magnetization switching properties were studied in large MTJ devices with a composite free layer. The deposition conditions of the nano-current-confined layer were optimized to achieve granular structure with superparamagnetic behavior. Two stable intermediate states were observed in both ellipse and bar shape MTJ devices, which have different switching mechanisms. The switching current distribution and the reversible intermediate state were also reported and discussed.

# Chapter 5 Conclusions

MTJ based spintronic devices and circuit, which is operated by spin-transfer-torque switching, has been proposed and studied. Three input MTJ cell was proposed as the basic logic cell. A basic logic unit that is composed of three MTJs connected by two NMCs was proposed as the building block of spintronic circuits. An advanced spintronic circuit, ALU, was designed and demonstrated based on the above proposed building blocks. Micromagnetic and HSPICE simulations have been done and demonstrated the operation of the basic logic unit and ALU. Based on this work, we believe that maximizing the functionality of the MTJ cells and minimizing the semiconductor components in spintronic circuits can further push the limit of traditional spintronic logic circuits in terms of functionalities and better device scaling.

A new type of MTJ devices was proposed and studied, which has a hybrid free layer structure. The hybrid structure introduces a spatial magnetic non-uniformity along the current direction, which exerts an adiabatic spin torque on the free layer. Through the optimization of the properties of the hybrid structure, the adiabatic spin torque can be larger than the conventional in-plane spin torque. Such a giant adiabatic torque can plays a critical role in the switching of the magnetization in the free layer. In particular, this torque allows for both the AP to P and P to AP switching operations with a single-polar current under different bias fields. In addition, the experimental results were confirmed by numerical simulations that were based on a macrospin model.

The current-induced magnetization switching properties were also studied in large

MTJ devices with a composite free layer. The deposition conditions of the nano-current-confined layer were optimized to achieve granular structure with superparamagnetic behavior. Two stable intermediate states were observed in both ellipse and bar shape MTJ devices, which have different switching mechanisms. The switching current distribution and the reversible intermediate state were also studied and discussed.

## Bibliography


1. S.A. Wolf, A. Y. Chtchelkanova, and D.M. Treger, IBM J. RES. & DEV. 50, 101-110 (2006)
2. http://nobelprize.org/nobel_prizes/physics/laureates/2007/info.html
3. M. Julliere, Phys. Lett. 54A: 225-226 (1975)
4. S. Maekawa and U. Gäfvert, IEEE Trans. Magn. 18, 707 (1982)
5. T. Miyazaki, and N. Tezuka, J. Magn. Magn. Mater., 139, L231-L234 (1995)
6. J.S. Moodera, L.R. Kinder, T.M. Wong, and R. Reservey, Phys. Rev. Lett., 74, 3273-3276 (1995)
7. S. Parkin, X. Jiang, C. Kaiser, A. Panchula, K. Roche, and M. Samant, Proc. Of the IEEE, 91, 661 (2003)
8. D. Wang, C. Nordman, J.M. Daughton, Z. Qian and J. Fink, IEEE Trans. Magn., 40, 2269 (2004)
9. S. Ikeda, et al, Appl. Phys. Lett., 93, 082508 (2008)
10. J. C. Slonczewski, J. Magn. Magn. Mater., 159, L1 (1996)
11. L. Berger, Phys. Rev. B, 54, 9353 (1996)
12. M. Tsoi, et al, Phys. Rev. Lett., 80, 2181 (1998)
13. G. Moore, Proc. Int. Solid-State Circuits Conf., 1, 20 (2003)
14. I. Amlani, A. O. Orlov, G. Toth, G. H. Bernstein, C. S. Lent, And G. L. Snider, *Science,* 284, 289 (1999)
15. A. Imre, G. Csaba, L. Ji, A. Orlov, G. H. Bernstein, and W. Porod, *Science*, 311, 205 (2006)
16. M. C. B. Parish, and M. Forshaw, *Appl. Phys. Lett.,* 83, 2046 (2003)
17. R. P. Cowburn, and M. E. Welland, *Science,* 287, 1466 (2000)
18. D. A. Allwood, G. Xiong, M. D. Cooke, C. C. Faulkner, D. Atkinson, N. Vernier, and R. P. Cowburn, *Science*, 296, 2003 (2002)
19. D. A. Allwood, G. Xiong, C. C. Faulkner, D. Atkinson, D. Petit, and R. P. Cowburn, *Science*, 309, 1688 (2005)
20. D. Atkinson, C. C. Faulkner, D. A. Allwood, and R. P. Cowburn, *Spin Dynamics in Confined Magnetic structures* III. Berlin; NY: Springer, 101, 207 (2006)
21. A. Ney, C. Pampuch, R. Koch, and K. H. Ploog, *Nature*, 425, 485 (2003)

22. C. Y. You, and S. D. Bader, *J. Appl. Phys.,* 87, 5215 (2000)
23. W. C. Black, and B. Das, *J. Appl. Phys*., 87, 6674 (2000)
24. A. Ney, and J. S. Harris, *Appl. Phys. Lett*., 86, 013502 (2005)
25. R. Richter, L. Bar, J. Wecker, and G. Reiss, *Appl. Phys. Lett*., 80, 1291 (2002)
26. J. G. Wang, H. Meng, and J.-P. Wang, *J. Appl. Phys*., 97, 10D509 (2005)
27. H. Meng, J. G. Wang, and J.-P. Wang, *IEEE Electron Dev. Lett.*, 26, 360 (2005)
28. J.-P. Wang, and X. F. Yao, *J. Nanoelectr. Optoelectr.,* **3**, 12 (2008)
29. S. Patil, X. F. Yao, H. Meng, J.-P. Wang, and D. Lilja, *ACM International Conference on Computing Frontiers*, section 5, 98 (2008)
30. S. Lee, S. Choa, S. Lee, and H. Shin, *IEEE Trans. Electron Dev.,* 54, 2040 (2007)
31. S. Ikeda, J. Hayakawa, Y. M. Lee, Matsukura, F., Ohno, Y., Hanyu, T., and Ohno, H., *IEEE Trans. Electr. Dev.,* 54, 991 (2007)
32. S. Lee, N. Kim, H. Yang, G. Lee, S. Lee, and H. Shin, *IEEE Trans. Magn.,* 43, 2677 (2007)
33. T. Kawahara, et al, Phys. Stat. Sol. (a) 204, 3929 (2007)
34. S. Matsunaga, et al, Appl. Phys. Expr. 1, 091301 (2008)
35. X.F. Yao, Y. S. Zhang, H. Meng, and J.-P. Wang, FC-03, *IEEE International Magnetic Conference*, Madrid, Spain (2008)
36. J. Harms, F. Ebrahimi, X.F. Yao, and J.-P. Wang, *IEEE Trans. Electr. Dev.*, 57, 1425 (2010)
37. A. Lyle, J. Harms, S. Patil, X.F. Yao, D. J. Lilja, and J.-P Wang, *Appl. Phys. Lett.*,97, 152504 (2010)
38. S. Matsunaga, J. Hayakawa, S. Ikeda, K. Miura, H. Hasegawa, T. Endoh, H. Ohno, and T. Hanyu, Appl. Phys. Exp., 1, 091301 (2008)
39. M. Hayashi, L. Thomas, C. Rettner, R. Moriya , X. Jiang, and S. S. P. Parkin, *Phys. Rev. Lett.,* 97, 207205 (2006)
40. D. Morecroft, I. A. Colin, F. J. Castano, J. A. C. Bland, and C. A. Ross, *Phys. Rev. B,* 76, 054449 (2007)
41. D. Ravelosona, S. Mangin, J.A. Katine, E. E. Fullerton, and B. D. Terris, *Appl. Phys. Lett.,* 90, 072508 (2007)
42. A. Yamaguchi, K. Yano, H. Tanigawa, S. Kasai, and T. Ono, *Jpn. J. Appl. Phys*., 45, 3850 (2006)
43. S. H. Florez, C. Krafft, and R. D. Gomez, *J. Appl. Phys.,* 97, 10C705 (2005)

44. J. Grollier, D. Lacour, V. Cros, A. Hamzic, A. Vaures, A. Fert, D. Adam, and G. Faini, *J. Appl. Phys.,* 92, 4825 (2002)
45. G. Tatara, and H. Kohno, *Phys. Rev. Lett.,* 92, 086601 (2004)
46. A. Thiaville, Y. Nakatani, J. Miltat, and Y. Suzuki, *Europhys. Lett.,* 69, 990 (2005)
47. A. Himeno, T. Ono, S. Nasu, K. Shigeto, K. Mibu, and T. Shinjo, *J. Appl. Phys.,* 93, 8430 (2003)
48. T. Ono, Y. Ooka, S. Kasai, H. Miyajima, N. Nakatani, N. Hayashi, K. Shigeto, K. Mibu, and T. Shinjo, *Mater. Sci. Eng. B,* 84, 126 (2001)
49. S. D. Kim, B. S. Chun, and Y. K. Kim, *J. Appl. Phys.,* 101, 09F504 (2007)
50. See LLG Micromagnetics Simulator™ at http://llgmicro.home.mindspring.com
51. A. Lyle, X.F. Yao, F. Ebrahimi, J. Harms, and J.-P Wang, *IEEE Trans. Magn*., 46, 2216 (2010)
52. X. F. Yao, H. Meng, Y. S. Zhang, and J.-P. Wang, *J. Appl. Phys.*, 103, 07A717 (2008)
53. H. Meng, and J.-P. Wang, *Appl. Phys lett.*, 89, 152509 (2006)
54. Y. Jiang, T. Nozaki, S. Abe, T. Ochiai, A. Hirohata, N. Tezuka, and K. Inomata, *Nature Mater.* 3, 361 (2004)
55. C. T. Yen, W. C. Chen, D. Y. Wang, Y. J. Lee, C. T. Shen, S. Y. Yang, C. H. Tsai, C. C. Hung, K. H. Shen, M. J. Tsai, and M. J. Kai, *Appl. Phys. Lett.*, 93, 092504 (2008)
56. Ren, F., Marković D., IEEE Trans. Electron Dev., 57, 1023 (2010)
57. M. Nakayama, T. Kai, N. Shimomura, M. Amano, E. Kitagawa, T. Nagase, M. Yoshikawa, T. Kishi, S. Ikegawa, and H. Yoda, J. Appl. Phys.103, 07A710 (2008)
58. S. Patil, A. Lyle, J. Harms and and D.J. Lilja, presented at the 28th IEEE Int. Conf. on Computer Design, Amsterdam, The Netherland, Oct.3-6, Paper 74 (2010)
59. L. Berger, *J. Appl. Phys.* 49, 2156 (1978)
60. Y.B. Bazaliy, B.A. Jones, and S.-C. Zhang, *Phys. Rev. B* 57, R3213-R3216 (1998)
61. G. Tatara, and H. Kohno, *Phys. Rev. Lett.* 92, 086601 (2004)
62. Z. Li, and S. Zhang, *Phys. Rev. B* 70, 024417 (2004)
63. S. Zhang, and Z. Li, *Phys. Rev. Lett.* 93, 127204 (2004)
64. L. Thomas, et al. *Nature* 443, 197 (2006)
65. M. Hayashi, L. Thomas, C. Rettner, R. Moriya, and S.S.P. Parkin, *Nature Phys.* 3, 21 (2007)
66. L. Thomas, et al. *Science* 315, 1553 (2007)
67. M. Kläui, et al. *Phys. Rev. Lett.* 95, 026601 (2005)

68. J.A. Katine, F.J. Albert, R.A. Buhrman, E.B. Myers, and D.C. Ralph, *Phys. Rev. Lett.* 84, 3149 (2000)
69. S. Mangin, et al., *Nature Mater.* 5, 210 (2006)
70. D. Ravelosona, et al., *Phys. Rev. Lett.* 96, 186604 (2006)
71. I.N. Krivorotov, et al., *Science* 307, 228 (2005)
72. D. Houssameddine, et al., *Nature Mater.* 6, 447 (2007)
73. O. Ozatay, et al. , *Nature Mater.* 7, 567 (2008)
74. Z. Li, et al., *Phys. Rev. Lett.* 100, 246602 (2008)
75. J.C. Sankey, et al, *Nature Phys.* 4, 67 (2008)
76. A.M. Deac, et al., *Nature Phys.* 4, 803 (2008)
77. H. Kubota, et al., *Nature Phys.* 4, 37 (2008)
78. G.D. Fuchs, et al., *Appl. Phys. Lett.* 86, 152509 (2005)
79. Y. Huai, M. Pakala, Z. Diao, and Y. Ding, *Appl. Phys. Lett.* 87, 222510 (2005)
80. H. Meng, J.G. Wang, and J.-P. Wang, *Appl. Phys. Lett.* 88, 082504 (2006)
81. J. Hayakawa, et al., *Japan. J. Appl. Phys.* 45, L1057 (2006)
82. C.-T. Yen, et al., A*ppl. Phys. Lett.* 93, 092504 (2008)
83. W. Kim, T.D. Lee, and K.J. Lee, *Appl. Phys. Lett.* 93, 232506 (2008)
84. J. Herfort, H.-P. Schönherr, and K.H. Ploog, *Appl. Phys. Lett.* 83, 3912 (2003)
85. G. Xiao, and C.L. Chien, *J. Appl. Phys.* 63, 4252 (1988)
86. J.Z. Sun, Phys. Rev. B 62, 570 (2000)
87. J. Grollier, V. Cros, A. Hamzic, J. M. George, H. Jaffres, A. Fert, G. Faini, J. Ben Youssef and H. Legall, *Appl. Phys. Lett.,* 78, 3663 (2001)
88. F. J. Albert, J. A. Katine, R. A. Buhrman and D. C. Ralph, *Appl. Phys. Lett.,* 77, 3809 (2000)
89. Y. M. Huai, F. Albert, P. Nguyen, M. Pakala and T. Valet, *Appl. Phys. Lett.,* 84, 3118 (2004)
90. J. Z. Sun, *J Magn Magn Mater,* 202, 157 (1999)
91. T. Y. Chen, Y. Ji, C. L. Chien and M. D. Stiles, *Phys. Rev. Lett.,* 93, 026601 (2004)
92. S. Zhang, P. M. Levy and A. Fert, *Phys. Rev. Lett.,* 88, 236601 (2002)
93. H. Meng and J. P. Wang, *IEEE Trans. Magn.,* 41, 2612 (2005)
94. H. Meng and J. P. Wang, *Appl. Phys. Lett.,* 88, 172506 (2006)
95. T. Yang, T. Kimura and Y. Otani, *J. Appl. Phys.,* 97, 064304 (2005)
96. Y. Jiang, N. Tezuka and K. Inomata, *Appl. Phys. Lett.,* 89, 122514 (2006)

97. D. Ravelosona, S. Mangin, Y. Lemaho, J. A. Katine, B. D. Terris and E. E. Fullerton, P*hys. Rev. Lett.,* 96, 186604 (2006)
98. H. Meng and J. P. Wang, *Appl. Phys. Lett.,* 89, 152509 (2006)
99. H. Meng and J. P. Wang, *IEEE Trans. Magn.,* 43, 2833 (2007)
100. J.-P. Wang and H. Meng, *Eur. Phys. J. B,* 59, 471 (2007)
101. X. F. Yao, H. Meng, Y. S. Zhang and J. P. Wang, *J. Appl. Phys.,* 103, 07A717 (2008)
102. J. Hayakawa, S. Ikeda, Y. M. Lee, R. Sasaki, T. Meguro, F. Matsukura, H. Takahashi and H. Ohno, *Jpn. J. Appl. Phys. Part 2,* 45, L1057 (2006)
103. H.J. Richter, A. Y. Dobin, O. Heinonen, K. Z. Gao, R. J. M. v. d. Veerdonk, R. T. Lynck, J. Xue, D. Weller, P. Asselin, M. F. Erden, and R. M. Brockie, *IEEE Trans. Magn*., 42, 2255 (2006)
104. J.C. Lodder, *J. Magn. Magn. Mater.*, 272, 1692 (2004)
105. R.H. Victora, X. Shen, *IEEE Trans. Magn.,* 41, 537 (2005)
106. D. Suess, Appl. Phys. Lett., 89, 113105 (2006)
107. J-P. Wang, W. K. Shen, and J. M. Bai, *IEEE Tran. Magn*, 41, 3181 (2005)
108. S. Y. Chou, P. R. Krauss, and P. J. Renstrom, *J. Vac. Sci. Technol. B*, 14, 4129 (1996)
109. J. G. Goodberlet, J. T. Hastings, and H. I. Smith, *J. Vac. Sci. Technol. B,* 19, 2499 (2001)
110. W.K. Shen, A. Das, M. Racine, R. Cheng, J. Judy, and J. P. Wang, *IEEE Trans. Magn.*, 42, 2381 (2006)

## Appendix A: Fabrication of Giant Magneto-Resistance Based Bio-magnetic Sensor

In this study, the magnetization of the free layer is used to store the information. The coercivity of the free layer should be small, which make the free layer easily be switched by a small field.

First, the film with free layer only was studied. NiFe is a soft magnetic material. When doping Nitrogen element in NiFe film, N atoms help reduce the grain size of NiFe, which make the coercivity smaller. We use mixed $N_2$-Ar gas during the sputtering process and varied the volume fraction of $N_2$ gas.

Fig.A.1 shows the M-H loops of the samples with different $N_2$ concentration. With higher $N_2$ concentration, the coercivity of NiFe film was reduced greatly. With 5% $N_2$, the coercivity was 1 Oe, which is satisfied our requirement.

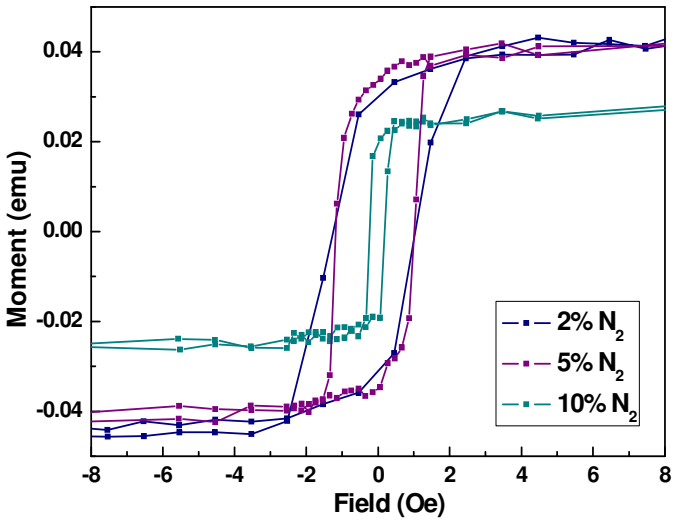


Fig.A.1 M-H loops of NiFe films with different $N_2$ doping.

Second, the fixed layer structure was studied. Samples with both free layer and fixed layer were deposited. By fixing the free layer structure with NiFe-5% $N_2$, the fixed layer structure was varied in order to get proper coercivity, and high magnetoresistance (MR) value.

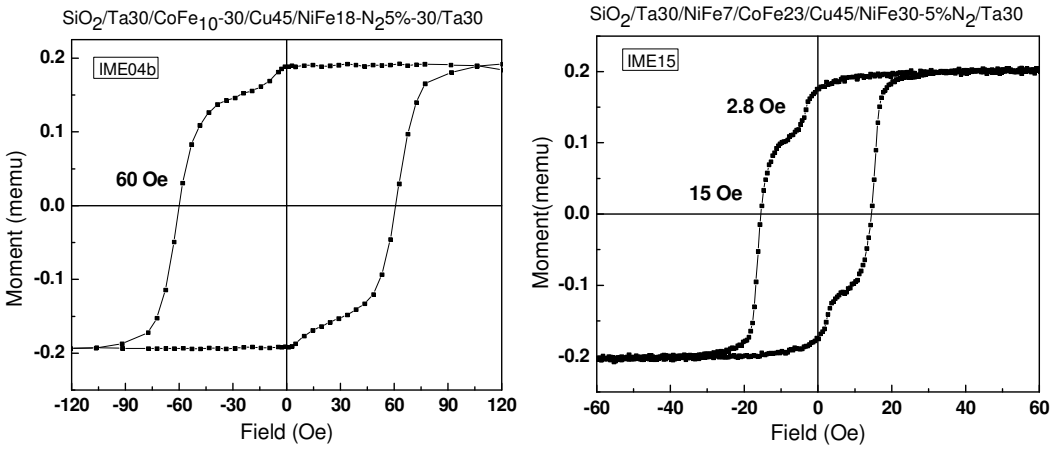


Fig.A.2 Hysteresis loops of samples with different fixed layer. (a) left: sample with 30 Å CoFe fixed layer; (b) right: sample with 7Å NiFe/23Å CoFe fixed layer.

Fig.A.2 (a) and (b) show the M-H loops of two samples with different fixed layer structure. The sample with 30 Å CoFe has 60 Oe coercivity, which is too large for the requirement of the memory cell. Thin NiFe layer (7Å), which replaced 7 Å CoFe in the fixed layer, effectively reduced the coercivity to 23.5 Oe. Also, the sample with 30 Å CoFe fixed layer had stronger exchange coupling between the free layer and the fixed layer, comparing with the sample with 7Å NiFe/23Å CoFe fixed layer. That is because

CoFe has larger magnetization than NiFe, which generates larger fringing field which is coupling with the free layer.

Since CoFe has higher magnetization, which results in higher spin-polarization comparing with NiFe, we exchanged the position of NiFe and CoFe layers in the fixed layer, and make CoFe layer adjacent to the spacing layer Cu.

The following R-H curves are for the samples with the same film structure, except the position of NiFe and CoFe in the fixed layer. It showed that the sample with CoFe adjacent to Cu had a little higher GMR value that that with NiFe adjacent to Cu.

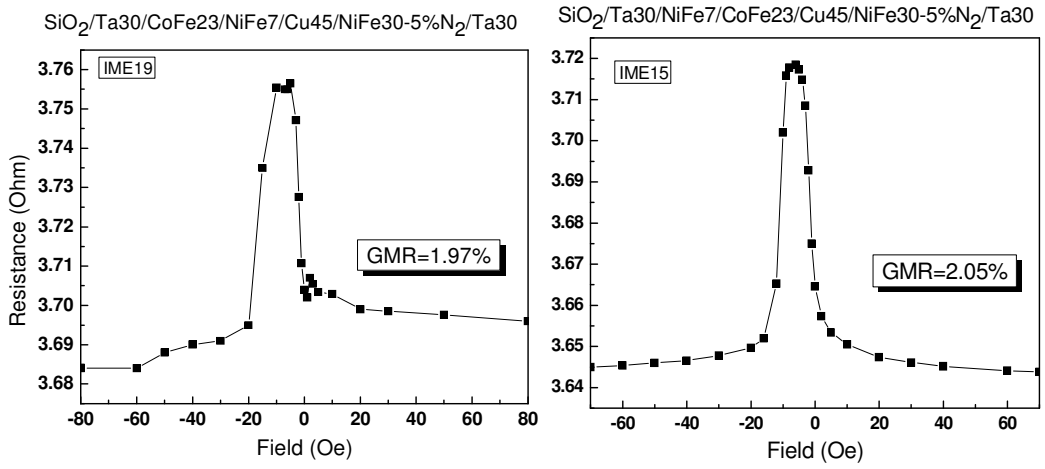


Fig.A.3 R-H loops of samples with the same structure except different fixed layer: (left) CoFe23Å/NiFe7Å/Cu; (right) NiFe7Å/CoFe23Å/Cu.

The films with different sputtering power will have different microstructure, crystal structure. Two samples with exactly the same film structures were deposited with different sputtering power (Fig.4). The sample with lower power had higher GMR value

(2.28%) comparing with the sample with higher power (2.05%); at the mean time, the coercivities of the free and fixed layer were increased. That is because the lower sputtering power makes the grains grow larger, which has higher coercivity. And the film with lower sputtering power has better crystal (film) quality, such as less defects, which increases the GMR value.

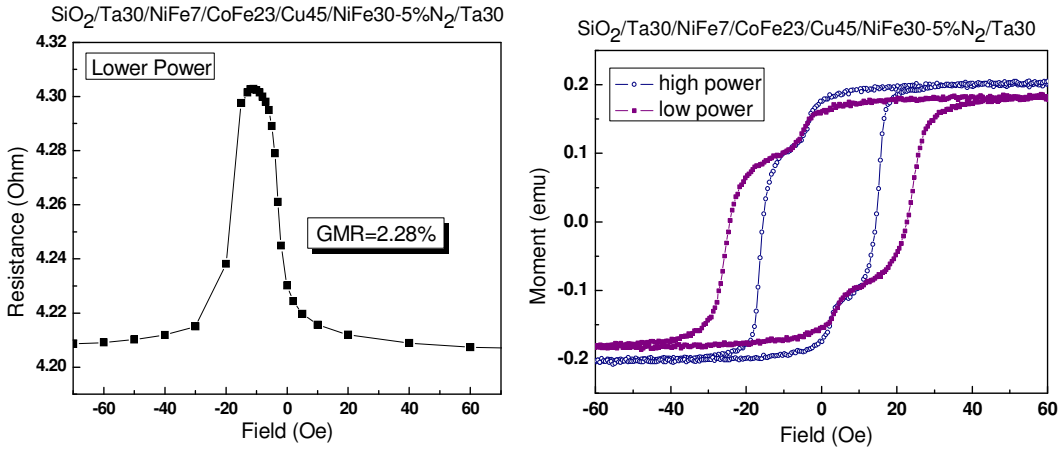


Fig.A.4 Left: R-H loop of sample deposited at low power; Right: M-H loops with samples deposited at different sputter power.

To further increase the GMR value, a thin CoFe layer was inserted between the free layer and the space layer Cu. The experimental results showed that GMR value was dramatically increased with such thin CoFe, which adjacent to Cu (Fig.5 left). And the thickness of such thin CoFe layer was adjusted to obtain a low coercivity of the free layer (Fig.5). The free layer with structure of 3Å CoFe/30 Å NiFe-5% $N_2$ had coercivity of 5 Oe.

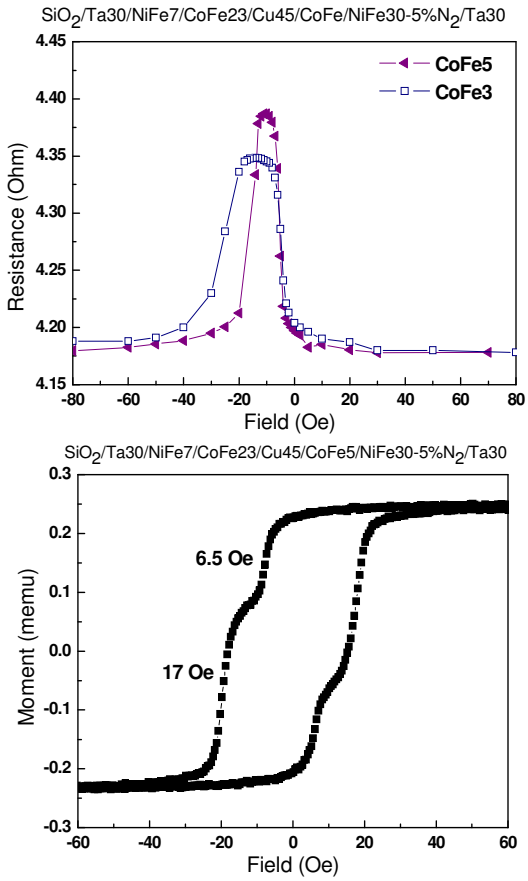


Fig.A.5 Left: R-H loop of samples with different thickness of thin CoFe layer; Right: M-H loops of the sample with 5Å CoFe between Cu and free layer.

The thickness of NiFe in the free layer was studied. The experiment results showed that samples with 40Å NiFe-5%$N_2$ had larger loop squareness than that with 30 Å NiFe-5%$N_s$. Such high squareness resulted in high GMR value of 5.53%. The full film

structure was: Si substrate/ thermal growth $SiO_2$1000/Ta30/NiFe7/CoFe23/Cu45 /CoFe5/ NiFe40-5%$N_2$/Ta30 (unit: Å). Such film structure had highest GMR value of 5.53% and low coercivity, and was used to deposit the wafers for device patterning.

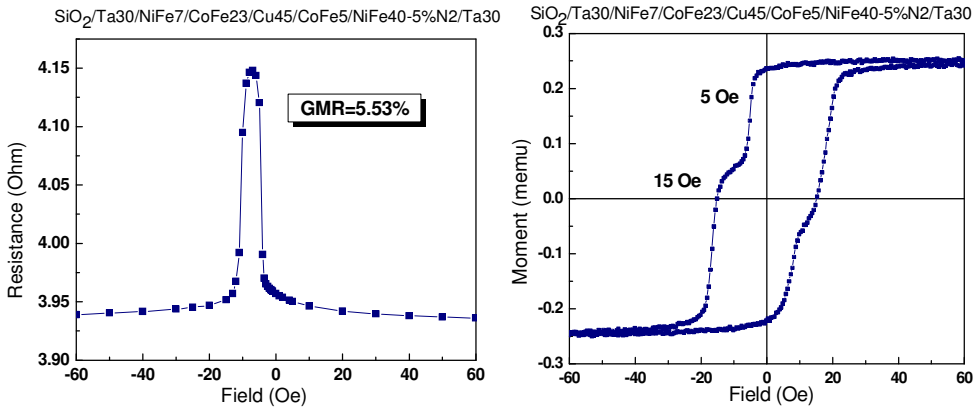


Fig.A.6 R-H (left) and M-H loop (right) of the sample with free layer structure of CoFe 5Å/NiFe 40Å-5%$N_2$.

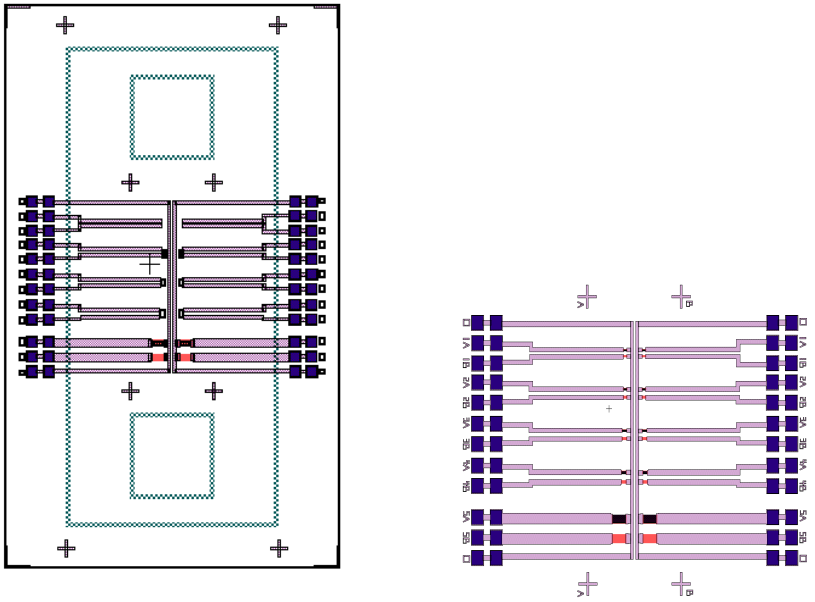

Fig.A.7: Device layout (left) and zoom in (right) of GMR based bio-magnetic sensor

In summary, the film structure of GMR was studied for the application of data storage. $N_2$ doped NiFe had lower coercivity than un-doped NiFe film. CoFe layer had higher spin-polarization, which was inserted between the spacer layer Cu and $N_2$-doped NiFe. This dramatically increased the GMR value. Proper NiFe layer thickness in the free layer (40Å) gave much higher squareness of M-H loop, comparing with the sample with 30 Å NiFe. The GMR value reached as high as 5.53%, and the coercivities of the free and fixed layer were 5 Oe and 15 Oe, respectively.

## Appendix B Study on Patterned Exchange Coupled Composite Media

*Abstract*—Patterned Exchange Coupled Composite media was fabricated by using a nano-imprinting lithography method. Scanning electron microscope image showed that the average dot size was about 100 nm. Magnetic force microscope images showed that patterned ECC dots can have single domain or multi-domain structure after AC demagnetization.

Patterned media is one of the promising candidates to overcome the magnetic recording density limitation. In the traditional thin film media, one bit contains many grains (in recent report [103], 1 bit has 65 grains for recording density of 250 Gbit/in$^2$). Patterned media has discrete magnetic islands arranged in 2-D, and each magnetic dot acts as a single bit. Because of the absence of transitional noise, patterned media has a higher signal to noise ratio (SNR) than thin film media with the same recording density [104]. In other words, patterned media could achieve higher recording density than thin film media. One of the challenges for patterned media is to fabricate uniform magnetic dots with narrow distribution of magnetic properties. Recent report showed that the bit-patterned media recording was very sensitive to the distributions of the magnetic properties**Error! Bookmark not defined.**. In this work, patterned media based on exchange coupled composite (ECC) structure was investigated. We have successfully demonstrated the advantages of ECC media and its switching mechanism in our previous reports [105-107], which provides a promising method to support recording areal density up to 1 Terabit/in$^2$. The advantages of ECC structure, like lower switching field and less

switching field distribution, have the potential to solve the patterned media problems as stated above.

Another challenge of patterned media is to fabricate small magnetic dots in large area with low cost. Among the fabrication methods, the combination of electron-beam and nano-imprinting lithography is a promising method to meet these requirements [104,108-109]. Electron beam can generate very small dots (~20 nm), and nano-imprinting has advantages of low cost and mass fabrication.

## EXPERIMENTS AND RESULTS

The fabrication of patterned ECC media includes three parts: ECC thin film preparation; mold fabrication by electron-beam lithography (EBL); cast fabrication and pressing by using nano-imprint lithography (NIL). Figure B.1 is the schematic drawing of the fabrication procedure.

### *B.1 ECC thin film preparation*

ECC thin film structure was deposited in an 8-target dc magnetron sputtering system. The film structure is: Si(1.5 nm)/CoCrPt-$SiO_2$(6 nm)/Pt(1 nm)/CoCrPt(20 nm)/Ru(20 nm)/Ta(2.5 nm)/Si substrate. The base pressure was around $1.5\times10^{-7}$ Torr. Ta and Ru were seedlayer and underlayer, respectively, to grow the (0002) textured CoCrPt [110]. The 6 nm thick CoCrPt-$SiO_2$ layer was magnetic soft with low Pt content at room temperature. The 1 nm Pt space layer in between of two CoCrPt-$SiO_2$ layers induced the stacking faults in soft CoCrPt-$SiO_2$ layer for a magnetic performance [105-107].

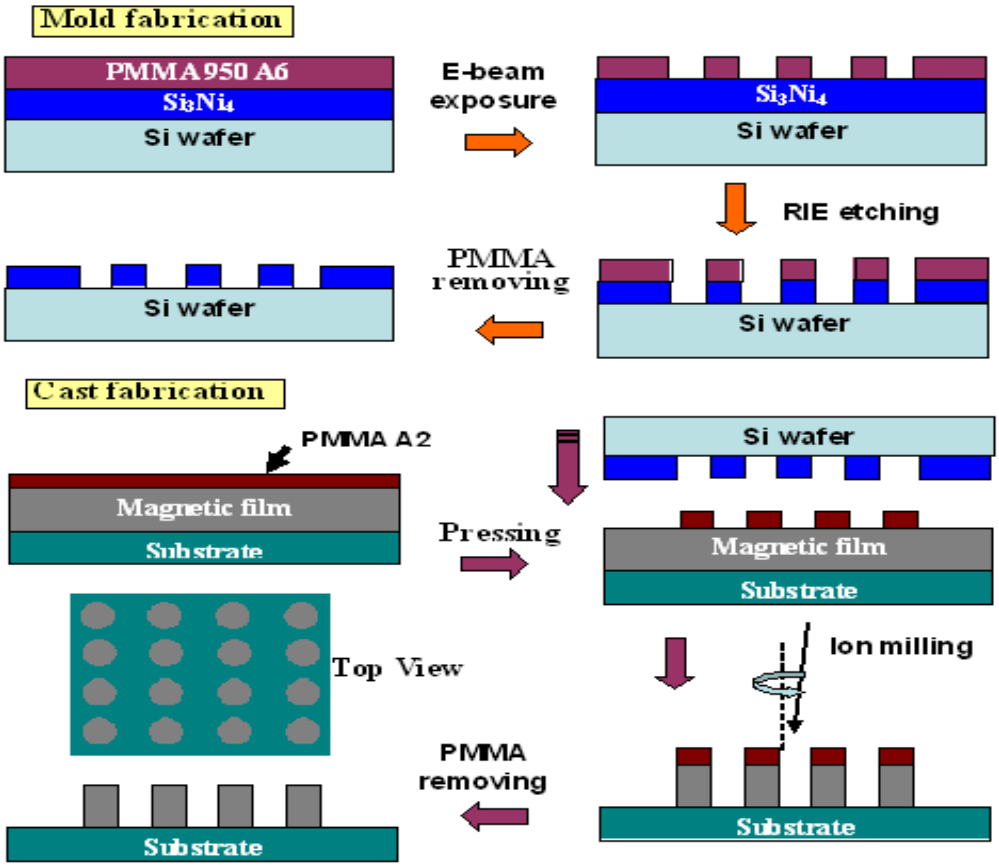


Fig.B.1 Schematic drawing of the fabrication procedure, which combined electron-beam and nano-imprint lithography.

The ECC thin film was deposited with well exchange coupled magnetic soft and hard layer. The granular structure and vertically column growth were obtained (TEM results were in ref. **Error! Bookmark not defined.**).

*B.2 Mold fabrication*

The mold was fabricated by EBL. 100 nm $Si_3N_4$ was first grown on Si substrate by low-pressure chemical vapor deposition (LPCVD) followed by spin coating PolyMethyl MethAcrylate (PMMA) A6. The dots matrix is as large as 1 mm×1 mm, and the distance between each exposure dot is 1μm. The developer is pure Methyl-Iso-butyl-Ketone (MIbK) and the developing time was 20 seconds. The next step was to transfer the nano-pattern on PMMA into the $Si_3N_4$ layer by using Reactive Ion Etching (RIE). The residual PMMA could be removed by either acetone or oxygen plasma.

*B.3 Cast fabrication and Pressing operation*

These steps were done by using nano-imprint lithography. First, a layer of PMMA A2 was coated on the top of ECC thin film. After that, the sample was baked at 180ºC for 2 hours to harden the PMMA layer and keep it in good shape after the following press operation.

A self-designed mechanical presser was used in the pressing step. The cast was fixed at the sample holder. By moving the stage with mold on it, mold contacted with the cast. The pressure applied on the mold was 250 psi for 15 second. Then the patterns on the mold were transferred successfully into the thickness contrast of the PMMA on the cast.

Nano-pattern structure was transferred to the ECC thin film by 7 minutes Ion Milling etching. The incident angle of ion beam with the film normal axis was 12º. The residual PMMA was removed by dry etching (RIE).

The Scanning Electron Microscope (SEM) image (Fig. B.2) of the patterned ECC

dots shows a good shape and size uniformity. The average diameter of the magnetic dots was 120 nm and the distance between each dot was 1μm.

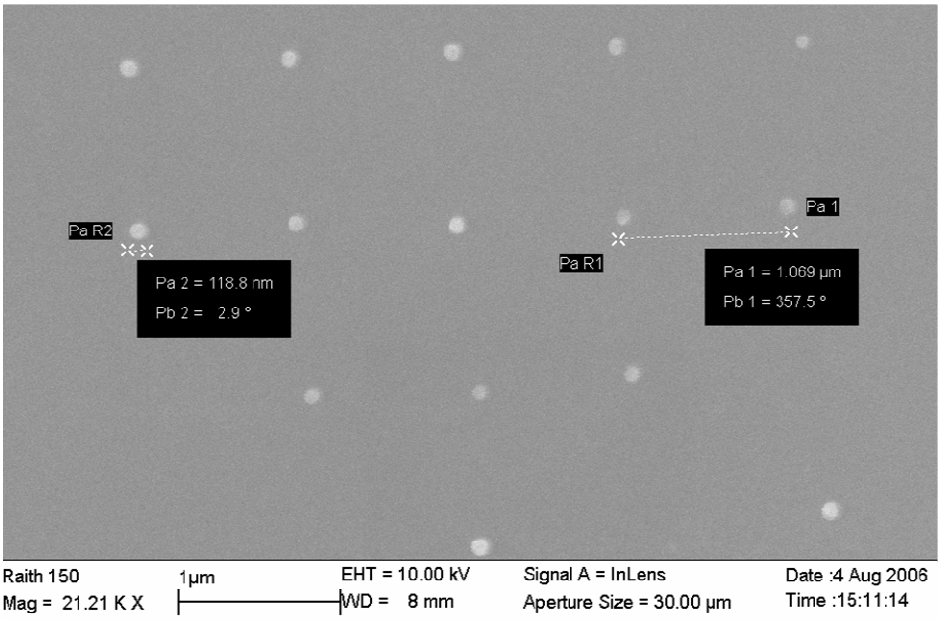


Fig.B.2 SEM image of patterned exchange coupled composite dots. The average dot diameter is 120 nm and the distance between the adjacent dots is 1 μm.

Fig. B.3 shows the measurement results by Magnetic Force Microscope (MFM). Before the measurement, the patterned ECC sample was demagnetized by AC magnetic field, which was perpendicular to the film plane. Fig. B.3 (A) shows the remanent state of four magnetic dots. Three dots had uniform color, which indicated that they had single domain structures. The one at the lower right corner had a color contrast between left and right parts. This may indicate that it had two magnetic domains in the remanent state. The multi-domain structure may be formed because of the large dot size (120 nm). Fig.B.3 (a) is the zoom in MFM image of the dot, which had two magnetic domains. Fig.

B.3 (B) shows the remanent state of the same four magnetic dots after applying a positive 12 KOe perpendicular magnetic field. All the dots have a uniform color, which means that they all have single domain structures at the remanent state. The magnetizations of the dots were pointing out of the paper plane. Fig.B.3 (C) shows the remanent state of the same four magnetic dots after applying a negative 12 KOe perpendicular magnetic field. The displayed uniform color indicates the all the dots have single domain structures. Three of them had magnetization reversed by pointing in the paper plane. However, the magnetization of the dot at the upper right corner didn't reversed after applying the negative field. Since the size of the patterned dots was large enough to exclude the thermal instable effect, one of the possible reasons is due to the

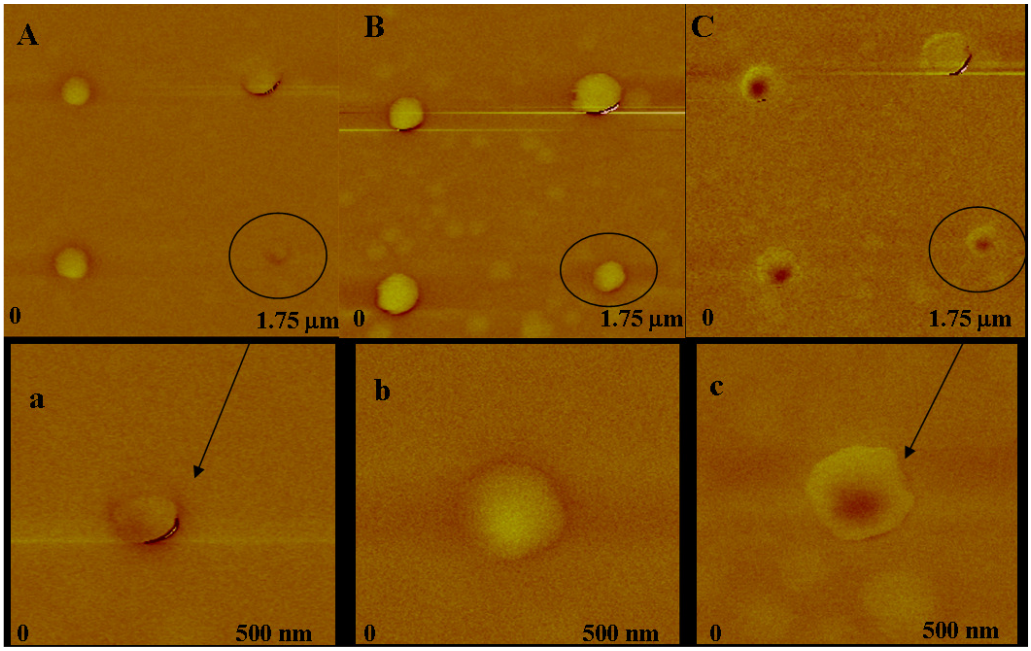


Fig.B.3 MFM images of patterned exchange coupled composite dots. (A)(a): remanent magnetic state after AC demagnetization. (B)(b): remanent magnetic state after magnetized by positive 12 KOe external field. (C)(c): remanent magnetic state after magnetized by negative 12 KOe external field. (A)(B)(C) were taken from the same area; and (a)(b)(c) were taken from the same dot.

fabrication process. A thin residual PMMA layer may be on the top of that dot after dry etching, which will increase the distance between the dot and the MFM tip and result a weak magnetic signal.

## SUMMARY

Patterned ECC media is the promising candidate to get higher recording density than conventional perpendicular media. By using E-beam and nano-imprint lithography method, patterned ECC media was successfully fabricated and tested. The average dot size was 120 nm. After AC demagnetization, magnetic dots may have single domain or multi-domain structure.

## Appendix C: HSPICE Simulation on Spintronic Logic Devices

→ MTJ macro-model with time dependence and advanced RV characteristics

→ MTJ macro-model with Nano-Magnetic-Channel (NMC)

→ Basic Logic Unit macro-model with four MTJs

→ Testbench for single MTJ hysteresis curve

→ Testbench for the operation of Nano-Magnetic-Channel (NMC)

→ Testbench for three-current input

→ Testbench for ALU simulation with input of (001)

```
** MTJTRV macro-model with time dependence and advanced RV characteristics
**
** Authors:
**      Jon Harms               (harms074@umn.edu)
**      Farbod Ebrahimi         (ebrah008@umn.edu)
**
** Latest Update:
**      2009 08 13
**
** -------------------------**
** Declaration of Sub-circuit
** -------------------------**

.SUBCKT MTJTRV n+ n-
.PRINT R(gMTJ)

** -------------------------**
** User Parameter Defaults
** -------------------------**
.PARAM
+       ICAP=-425u
+       ICP=325u
+       R0=1.8k
+       A0=2.7k
+       W0=.615
+       V0=-.1
+       R1=800
+       A1=1k
+       W1=.615
+       V1=-.1
+       THSBT=22
+       IC=-1
+       TTP=7n
+       PCAP=.6f
+       ITPP='ICP*(1-THSBT*log(TTP/1n))'
+       ITPAP='ICAP*(1-THSBT*log(TTP/1n))'

** -------------------------**
** MTJ Electrode Connections
** -------------------------**

*~Voltage Controlled Resistor
gMTJ   n+      nVCR1 VCR    nVCtrl  0       1

*~Parasitic Capacitance
cPara   n+      nVCR1 'PCAP'

*~Current Sampling
vISample        n-      nVCR1 DC=0
```

```
*~Binary Current Sensors
eISensBin1      nINeg 0VOL='EXP(5*I(vISample)/ICP)-1' MIN=0 MAX=1
eISensBin2      nIPos 0 VOL='EXP(5*I(vISample)/ICAP)-1' MIN=0 MAX=1

** -------------------------**
** Decision Circuit
** -------------------------**

*~Current mirrors
gMirror1        n51     n50     CUR='1/(EXP(THSBT*(1+I(vISample)/-ICAP))+TTP*1e5*(-
ITPAP/I(vISample))^2)' MAX=10

gMirror2        n50     n51
        CUR='1/(EXP(THSBT*(1+I(vISample)/ICP))+TTP*1e5*(ITPP/I(vISample))^2)'
MAX=10

*~Decision capacitors
cDec1   n50     0 1n IC=0
cDec2   n51     0 1n IC=0

*~Voltage limiters
rlim1   n50     n60     .01
elim1   n60     0       n50     0       1       MIN=0 MAX=1.01
rlim2   n51     n61     .01
elim2   n61     0       n51     0       1       MIN=0 MAX=1.01
rshunt1 n50 0 10g
rshunt2 n51 0 10g

*~Current controlled 2:1 MUX
eMux3 nVDec  0       VOL='v(n50)*v(nINeg)-v(n51)*v(nIPos)'

** -------------------------**
** Bi-stable Multivibrator
** -------------------------**

*~Amplifier w/clipping
eBiStable       nBiStable       0       VCVS  nFeedback      0       10000   MAX=10V
        MIN=-10V

*~Positive Feedback
rFB1    nVDec nFeedback       1e3
rFB2    nFeedback       nBiStable       10e3

*~Initial Conditions
cIC1    nFeedback       0       1f      IC='(IC<0)?-1V:1V'
cIC2    nBiStable       0       1f      IC='(IC<0)?-10V:10V'

** -------------------------**
```

```
** Curve Fitting Circuit
** -------------------------**

*~Curve fitting amplifiers
eRVFitHigh      nRVFitHigh      0
          VOL='(.5+.05*v(nBiStable))*(R0+(A0/(W0*1.2533)*EXP(-2*POW(v(n+)-v(n-)-
V0,2)/POW(W0,2))))'

eRVFitLow       nRVFitLow       0          VOL='(.5-
.05*v(nBiStable))*(R1+(A1/(W1*1.2533)*EXP(-2*POW(v(n+)-v(n-)-V1,2)/POW(W1,2))))'

eRVFit nRVFit 0          VOL='v(nRVFitHigh)+v(nRVFitLow)'

*Feedback filter (avoids oscillation)
rShunt3             nRVFit nVCtrl 1k
cSRL2  nVCtrl 0 6f

.ends MTJTRV
```

```
** MTJ macro-model with Nano-Magnetic-Channel (NMC)
**
** Authors:
**      Jon Harms                   (harms074@umn.edu)
**
** Latest Update:
**      2010 06 15
**

** -------------------------**
** Declaration of Sub-circuit
** -------------------------**

.SUBCKT MTJ4T nL n+ nR n- stateL stateR nBiStable
.PRINT R(gMTJ)

** -------------------------**
** User Parameter Defaults
** -------------------------**
.PARAM
+       ICAP=-400u
+       ICP=400u
+       ICChan=1m
+       RAP=2k
+       RP=1k
+       RChannel=3k
+       RVFIT=.5
+       IC=-1

** -------------------------**
** MTJ Electrode Connections
** -------------------------**

*~Channel Connections
rL nL nfreeL 'RChannel/2'
rR nR nfreeR 'RChannel/2'

*~Voltage Controlled Resistor
gMTJ   n+      nVCR1 VCR    nVCtrl  0       1e3

*~Current Sampling
vISample        n- nVCR1 DC=0
vISampleL       n+ nfreeL DC=0
vISampleR       n+ nfreeR DC=0

** -------------------------**
** Decision Circuit
** -------------------------**
```

```
*~Current mirrors
fMirror1 0 nVTest  CCCS vISample  1
fMirror2 0 nVTestL CCCS vISampleL 1
fMirror3 0 nVTestR CCCS vISampleR 1

*~Reference currents
iRefICAP nVRefICAP 0 DC='ICAP'
iRefICP nVRefICP 0 DC='ICP'
iRefICChan nVRefChan 0 DC='ICChan'

*~Terminating resistors
rterm1  nVtest    0 1k
rterm2  nVRefICAP 0 1k
rterm3  nVRefICP  0 1k
rterm4  nVtestL   0 1k
rterm5  nVtestR   0 1k
rterm6  nVRefChan 0 1k

eDec1 n50 0 VCVS nVTest nVRefICAP  1e3 MAX=1.01V MIN=0V
eDec2 n51 0 VCVS nVTest nVRefICP   1e3 MAX=0V MIN=-1.01V
eDec3 n52 0 VCVS nVRefChan nVTestL 1e3 MAX=.2V MIN=0V
eDec4 n53 0 VCVS nVRefChan nVTestR 1e3 MAX=.2V MIN=0V

eDec5 nstateL 0 VCVS stateL 0 1
eDec6 nstateR 0 VCVS stateR 0 1

*~Current controlled 2:1 MUX
eMux3 nVDec  0          VOL='v(n50)+v(n51)+v(n52)*v(stateL)+v(n53)*v(stateR)'

** -------------------------**
** Bi-stable Multivibrator
** -------------------------**

*~Amplifier w/clipping
eBiStable       nBiStable       0       VCVS  nFeedback       0       10000   MAX=10V
        MIN=-10V

*~Positive Feedback
rFB1    nVDec  nFeedback       1e3
rFB2    nFeedback       nBiStable       10e3

*~Initial Conditions
cIC1    nFeedback       0       1f      IC='(IC<0)?-1V:1V'
cIC2    nBiStable       0       1f      IC='(IC<0)?-10V:10V'

*~Biasing and offset
eVTMR           nVTMR           0       VCVS  nBistable       0       1       MIN='RP/1e3'
MAX='RAP/1e3'
```

```
** -------------------------**
** Curve Fitting Circuit
** -------------------------**

*~Curve fitting amplifiers
eRVFit nRVFit 0          VOL='v(nVTMR)*(EXP((PWR(ABS(v(n+)-v(n-)),2)/(-2*RVFIT))))'

*Feedback filter (avoids oscillation)
rShunt3             nRVFit nVCtrl 1k
cSRL2  nVCtrl 0 6f

.ends MTJ4T
```

```
** Basic logic unit macro-model with four MTJs
**
** Authors:
**        Jon Harms                (harms074@umn.edu)
**        Farbod Ebrahimi          (ebrah008@umn.edu)
**
** Latest Update:
**        2009 08 13
**

** -------------------------**
** Declaration of Sub-circuit
** -------------------------**

.SUBCKT MTJ4T nL n+ nR n- stateL stateR nBiStable
.PRINT R(gMTJ)

** -------------------------**
** User Parameter Defaults
** -------------------------**
.PARAM
+         ICAP=-400u
+         ICP=400u
+         ICChan=1m
+         RAP=2k
+         RP=1k
+         RChannel=3k
+         RVFIT=.5
+         IC=-1

** -------------------------**
** MTJ Electrode Connections
** -------------------------**

*~Channel Connections
rL nL nfreeL 'RChannel/2'
rR nR nfreeR 'RChannel/2'

*~Voltage Controlled Resistor
gMTJ   n+        nVCR1 VCR     nVCtrl  0          1e3

*~Current Sampling
vISample         n- nVCR1 DC=0
vISampleL        n+ nfreeL DC=0
vISampleR        n+ nfreeR DC=0

** -------------------------**
** Decision Circuit
** -------------------------**
```

```
*~Current mirrors
fMirror1 0 nVTest  CCCS vISample  1
fMirror2 0 nVTestL CCCS vISampleL 1
fMirror3 0 nVTestR CCCS vISampleR 1

*~Reference currents
iRefICAP nVRefICAP 0 DC='ICAP'
iRefICP nVRefICP 0 DC='ICP'
iRefICChan nVRefChan 0 DC='ICChan'

*~Terminating resistors
rterm1  nVtest    0 1k
rterm2  nVRefICAP 0 1k
rterm3  nVRefICP  0 1k
rterm4  nVtestL   0 1
rterm5  nVtestR   0 1k
rterm6  nVRefChan 0 1k

eDec1 n50 0 VCVS nVTest nVRefICAP  1e3 MAX=1.01V MIN=0V
eDec2 n51 0 VCVS nVTest nVRefICP   1e3 MAX=0V MIN=-1.01V
eDec3 n52 0 VCVS nVRefChan nVTestL 1e3 MAX=.2V MIN=0V
eDec4 n53 0 VCVS nVRefChan nVTestR 1e3 MAX=.2V MIN=0V

eDec5 nstateL 0 VCVS stateL 0 1
eDec6 nstateR 0 VCVS stateR 0 1

*~Current controlled 2:1 MUX
eMux3 nVDec  0          VOL='v(n50)+v(n51)+v(n52)*v(stateL)+v(n53)*v(stateR)'

** -------------------------**
** Bi-stable Multivibrator
** -------------------------**

*~Amplifier w/clipping
eBiStable       nBiStable       0       VCVS  nFeedback       0       10000   MAX=10V
        MIN=-10V

*~Positive Feedback
rFB1    nVDec  nFeedback       1e3
rFB2    nFeedback       nBiStable       10e3

*~Initial Conditions
cIC1    nFeedback       0       1f      IC='(IC<0)?-1V:1V'
cIC2    nBiStable       0       1f      IC='(IC<0)?-10V:10V'

*~Biasing and offset
eVTMR           nVTMR           0       VCVS  nBistable       0       1       MIN='RP/1e3'
MAX='RAP/1e3'
```

```
** -------------------------**
** Curve Fitting Circuit
** -------------------------**

*~Curve fitting amplifiers
eRVFit nRVFit 0          VOL='v(nVTMR)*(EXP((PWR(ABS(v(n+)-v(n-)),2)/(-2*RVFIT))))'

*Feedback filter (avoids oscillation)
rShunt3             nRVFit nVCtrl 1k
cSRL2  nVCtrl 0 6f

.ends MTJ4T
```

```
** ---------------------------------------**
** Testbench of single MTJ Hysteresis Curve
**    Simulation Parameters & Stimulus
** ---------------------------------------**

.TRAN .001n 10n
.print i(vsample)

i0 0 free DC=0 PULSE(1m -1m 0 2.5n 2.5n .1n 5n)


*i4 0 free DC=0 PULSE(0 200u  6n .01n .01n .05n 1u)
*i3 0 free DC=0 PULSE(0 -200u 1n .01n .01n .05n 1u)


vsample fixed 0 DC=0

** ---------------------------------------**
** Option Statements
** ---------------------------------------**

.TEMP 25
.OPTION
+    ARTIST=2
+    INGOLD=2
+    MEASOUT=1
+    PARHIER=LOCAL
+    PSF=2
+    LIST
+    NODE
+    POST

** ---------------------------------------**
** MTJ Instantiation
** ---------------------------------------**

Xmtj1 free fixed mtj ICAP=-600u          ICP=433u RVFIT=1000 SWTIME=.01n IC=1

.END
```

```
** --------------------------------------**
** Testbench of the operation of NMC
**    Simulation Parameters & Stimulus
** --------------------------------------**

* Current Source Test

.TRAN '1p' '100n'

i1a nfree1a x PULSE(0 1m 10n .1n .1n 2n 1)
i1b nfree1b x PULSE(0 1m 20n .1n .1n 2n 1)
i1c nfree1c x PULSE(0 -1m 30n .1n .1n 2n 1)
i1d nfree1d x PULSE(0 -1m 40n .1n .1n 2n 1)
i1e nfree1e x PULSE(0 1m 50n .1n .1n 2n 1)
i1f nfree1f x PULSE(0 1m 60n .1n .1n 2n 1)
i1g nfree1g x PULSE(0 -1m 70n .1n .1n 2n 1)
i1h nfree1h x PULSE(0 -1m 80n .1n .1n 2n 1)

r1a nfree1a nfree1 100
r1b nfree1b nfree1 100
r1c nfree1c nfree1 100
r1d nfree1d nfree1 100
r1e nfree1e nfree1 100
r1f nfree1f nfree1 100
r1g nfree1g nfree1 100
r1h nfree1h nfree1 100

i2a nfree2a y PULSE(0 1m 10n .1n .1n 2n 1)
i2b nfree2b y PULSE(0 1m 20n .1n .1n 2n 1)
i2c nfree2c y PULSE(0 1m 30n .1n .1n 2n 1)
i2d nfree2d y PULSE(0 1m 40n .1n .1n 2n 1)
i2e nfree2e y PULSE(0 -1m 50n .1n .1n 2n 1)
i2f nfree2f y PULSE(0 -1m 60n .1n .1n 2n 1)
i2g nfree2g y PULSE(0 -1m 70n .1n .1n 2n 1)
i2h nfree2h y PULSE(0 -1m 80n .1n .1n 2n 1)

r2a nfree2a nfree2 100
r2b nfree2b nfree2 100
r2c nfree2c nfree2 100
r2d nfree2d nfree2 100
r2e nfree2e nfree2 100
r2f nfree2f nfree2 100
r2g nfree2g nfree2 100
r2h nfree2h nfree2 100

v3a nL1a nR2a PULSE(0  4meg  15n .1n .1n 2n 20n)
v3b nL1b nR2b PULSE(0 -4meg 25n .1n .1n 2n 20n)
r3a nL1a nL1 1000e6
```

```
r3b nL1b nL1 1000e6
r3c nR2a nR2 1000e6
r3d nR2b nR2 1000e6

rx x 0 100e6
ry y 0 100e6

** --------------------------------------**
** MTJ Instantiation .SUBCKT MTJ nL n+ nR n- stateL stateR nBiStable
** --------------------------------------**
Xmtj1 nL1   nfree1 nChan x nBistable1 nBistable2 nBistable1 MTJ4T
Xmtj2 nChan nfree2 nR2 y   nBistable1 nBistable2 nBistable2 MTJ4T

** --------------------------------------**
** Option Statements
** --------------------------------------**
.OPTION
+   ARTIST=2
+   INGOLD=2
+   MEASOUT=1
+   PARHIER=LOCAL
+   PSF=2
+   LIST
+   NODE
+   POST


.END
```

```
** --------------------------------------**
** Testbench of three current input
**    Simulation Parameters & Stimulus
** --------------------------------------**

.TRAN '1p*mult' '10n*mult'
.print i(vsample) v(free)

.param
+mult=10
+mult2=.1

vsa na 0 0
vsb nb 0 0
vsc nc 0 0

ia na n1 DC=0 PULSE(-500u 500u 'mult*0.5n' 'mult2*.01n' 'mult2*.01n' 'mult*1n' 'mult*2n')
ib nb n1 DC=0 PULSE(-500u 500u 'mult*0.5n' 'mult2*.01n' 'mult2*.01n' 'mult*2n' 'mult*4n')
ic nc n1 DC=0 PULSE(-500u 500u 'mult*0.5n' 'mult2*.01n' 'mult2*.01n' 'mult*4n' 'mult*8n')

l1 n1 free .05m
r1 n1 0 1meg

vsample fixed 0 DC=0

** --------------------------------------**
** MTJ Instantiation
** --------------------------------------**
Xmtj1 free fixed MTJTRV

** --------------------------------------**
** Option Statements
** --------------------------------------**
.OPTION
+    ARTIST=2
+    INGOLD=2
+    MEASOUT=1
+    PARHIER=LOCAL
+    PSF=2
+    LIST
+    NODE
+    POST

.END
```

```
** ---------------------------------------**
** ALU simulation with input of (001)
** ---------------------------------------**

* ALU Simulation

.TRAN '1p' '100n'

.param a=0 b=0 c=1

vrefh sh 0 1
vrefl sl 0 -10

vm1 m1 0 DC=0 PULSE(0 1 40n 1n 1n 10n 100n)
vm2 m2 0 DC=0 PULSE(0 0 0 1n 1n 10n 100n)
vm3 m3 0 DC=0 PULSE(0 0 0 1n 1n 10n 100n)
vm4 m4 0 DC=0 PULSE(0 0 0 1n 1n 10n 100n)
vm5 m5 0 DC=0 PULSE(0 0 0 1n 1n 10n 100n)

vaa aa 0 DC=0 PULSE(0 'a'   10n 1n 1n 10n 100n)
vap ap 0 DC=0 PULSE(0 '1-a' 10n 1n 1n 10n 100n)

vbb bb 0 DC=0 PULSE(0 'b'   10n 1n 1n 10n 100n)
vbp bp 0 DC=0 PULSE(0 '1-b' 10n 1n 1n 10n 100n)

vcc cc 0 DC=0 PULSE(0 'c'   10n 1n 1n 10n 100n)
vcp cp 0 DC=0 PULSE(0 '1-c' 10n 1n 1n 10n 100n)

vblock block 0 DC=0 PULSE(1 0 69n 1n 1n 14n 100n)

vread read 0 DC=0 PULSE(0 1 70n 1n 1n 10n 100n)

** ---------------------------------------**
** MTJ Instantiation .SUBCKT MTJ nL n+ nR n- stateL stateR nBiStable
** ---------------------------------------**

g1        n000     0          VCR     block    0          0v,0.001 1v,10e6

Xmtj1 n001 n002 n003 n038 s1 s2 s1 MTJ4T
Xmtj2 n003 n004a n005 n000 s1 s3 s2 MTJ4T
Xmtj3 n005 nfe3 n006 nfx3 s2 sL s3 MTJ4T

xinort1 n001 n005 m1 inort imag=2m
xinort2 n006 n003 m2 inort imag=2m
xinort3 n006 n003 m3 inort imag=2m
xinort4 n006 n003 m4 inort imag=2m

xinort5 n002 n038 cp inort imag=1m
xinort6 n038 n002 cc inort imag=1m
```

```
g2        n004a   n004b   VCR     block   0         0v,0.001 1v,10e6

Xmtj4 n007 n006 n008 n039 s4 s5 s4 MTJ4T
Xmtj5 n008 n004b n009 n011a s4 s6 s5 MTJ4T
Xmtj6 n009 nfe6 n010 nfx6 s5 sL s6 MTJ4T

xinort7 n007 n009 m1 inort imag=2m
xinort8 n010 n008 m2 inort imag=2m
xinort9 n010 n008 m4 inort imag=2m
xinort10 n010 n008 m4 inort imag=2m

xinort11 n006 n039 bp inort imag=1m
xinort12 n039 n006 bb inort imag=1m

g3        n011a   n011b   VCR     block   0         0v,0.001 1v,10e6

** Note MTJ8 has been removed, but m5 was connected to mtj7 state to simulate it
Xmtj7  n014 n013 n015 n012 s7 s9  s7  MTJ4T
Xmtj9  n015 n016 n017 n011b s7 s10 s9  MTJ4T
Xmtj10 n017 n018 n019 n040 s9 s10 s10 MTJ4T

xinort13 n014 n017 m1 inort imag=2m
xinort14 n014 n017 m5 inort imag=2m
xinort15 n015 n019 m4 inort imag=2m

xinort16 n013 n012 ap inort imag=1m
xinort17 n012 n013 aa inort imag=1m

xinort18 n018 n040 ap inort imag=1m
xinort19 n040 n018 aa inort imag=1m

xinort20 n018 n040 bp inort imag=1m
xinort21 n040 n018 bb inort imag=1m

xinort22 n018 n040 cp inort imag=1m
xinort23 n040 n018 cc inort imag=1m


** ---------------------------------------**
** Optional Section to be removed
** ---------------------------------------**

*Xmtj11 n023 ne11 n024 nx11 s12 sL  s11 MTJ4T
*Xmtj12 n022 n011 n023 n025 s13 s11 s12 MTJ4T
*Xmtj13 n020 n021 n022 n041 s13 s12 s13 MTJ4T
*
*xinort42 n020 n023 m2 inort imag=2m
*xinort43 n024 n022 m3 inort imag=2m
```

```
*
*xinort24 n021 n041 ap inort imag=1m
*xinort25 n041 n021 aa inort imag=1m
*
*xinort26 n021 n041 bp inort imag=1m
*xinort27 n041 n021 bb inort imag=1m
*
*xinort28 n021 n041 cp inort imag=1m
*xinort29 n041 n021 cc inort imag=1m


r n026 n028 1.5k

Xmtj14 n031a ne14 n032  nx14 s15 sL  s14 MTJ4T
Xmtj15 n030  n031b n031a n028 s16 s14 s15 MTJ4T
Xmtj16 n029  n037 n030  n042 s16 s15 s16 MTJ4T

xinort44 n029 n031a m1 inort imag=2m
xinort45 n029 n031a m5 inort imag=2m
xinort46 n032 n030 m2 inort imag=2m
xinort47 n032 n030 m3 inort imag=2m
xinort48 n032 n030 m4 inort imag=2m

xinort30 n037 n042 ap inort imag=1m
xinort31 n042 n037 aa inort imag=1m

xinort32 n037 n042 bp inort imag=1m
xinort33 n042 n037 bb inort imag=1m

xinort34 n037 n042 cp inort imag=1m
xinort35 n042 n037 cc inort imag=1m

g4        n031aa  n031b   VCR     block    0          0v,0.001 1v,10e6

Xmtj17 n035 ne17 n036 nx17 s18 sL  s17 MTJ4T
Xmtj18 n034 n031aa n035 nStrange s19 s17 s18 MTJ4T
Xmtj19 n032 n033 n034 n050 s19 s18 s19 MTJ4T

xinort49 n032 n035 m1 inort imag=2m
xinort50 n036 n034 m2 inort imag=2m
xinort51 n036 n034 m4 inort imag=2m
xinort52 n036 n034 m5 inort imag=2m

xinort36 n033 n050 ap inort imag=1m
xinort37 n050 n033 aa inort imag=1m

xinort38 n033 n050 bp inort imag=1m
xinort39 n050 n033 bb inort imag=1m
```

```
xinort40 n033 n050 cp inort imag=1m
xinort41 n050 n033 cc inort imag=1m

g5        nStrange 0        VCR     block    0          0v,0.001 1v,10e6

** ---------------------------------------**
** Sense Amplifier
** ---------------------------------------**
xinort70 n016 0 read inort imag=100u
xinort71 n026 0 read inort imag=100u

e1 n+ 0 VCVS n016 n026 1e6 max=1 min=-1

e2089 nread 0 VCVS sh read 1

g6 n+   ns01 VCR nread 0 0v,0.001 1v,10e6

.print r(g6)

r2492 ns01 valmostout 1k

e2 valmostout 0 VCVS ns01 0 1000 max=.5 min=-.5

v2389 vout valmostout DC=.5


** ---------------------------------------**
** Option Statements
** ---------------------------------------**
.OPTION
+    ARTIST=2
+    INGOLD=2
+    MEASOUT=1
+    PARHIER=LOCAL
+    PSF=2
+    LIST
+    NODE
+    POST

** ---------------------------------------**
** Current Source Subcircuit
** ---------------------------------------**
.subckt inort n+ n- enable

.param
+ imag=1m

*~Voltage Controlled Resistor (Switches)
g1        n+        n0        VCR     en        0          0v,0.001 1v,10e6
```

```
g2      n-      n2      VCR    en      0       0v,0.001 1v,10e6

r1 n0 n1 100e3

v1 ref 0 1
e1 en 0 VCVS ref enable 1
v2 n1 n2 'imag*100e3*1.12'


r2 n+ 0 10e6
r3 n- 0 10e6

.ends

.END
```

## Appendix D Publications and Presentations

Publications:

1. X.F. Yao, J. Harms, A. Lyle, F. Ebrahimi, Y.S. Xhang, and J.-P. Wang, "Magnetic tunnel junction-based spintronic logic units operated by spin transfer torque", *IEEE Trans. NanoTech.* (2011) Accepted.
2. X.F. Yao, Y.S. Zhang, A.Lyle, R. Malmhall, R. Ranjan, L. Lu, M.Z. Wu, H. Wang, Y. Jing, and J.-P. Wang, "Observation of unique current-induced switching in magnetic tunnel junctions with hybrid free layer structure", *Appl. Phys. Lett.* (2011) submitted.
3. X.F. Yao, R. Malmhall, R. Ranjan, and J-P Wang, "Observation of intermediate states in magnetic tunnel junctions with composite free layer", *IEEE Trans. Magn.,* 44, 2496 (2008)
4. X.F. Yao, H. Meng, Y. Zhang, and J-P Wang, "Improved current switching symmetry of MTJ and GMR devices with nano-current-channel structure", *J. Appl. Phys*., 103, 07A717 (2008)
5. J-P Wang, X.F. Yao, "Programmable spintronic logic devices for reconfigurable computation and beyond- history and outlook", *J. Nanoelectr. Optoelectr.*, (Invited Paper) 3, 22 (2008)
6. A. Lyle, X.F. Yao, F. Ebrahimi, J. Harms, and J.-P. Wang, "Communication between magnetic tunnel junctions using spin-polarized current for logic applications", IEEE Trans. Magn., 46, 2216 (2010)
7. J. Harms, F. Ebrahimi, X.F. Yao, and J-P. Wang, "SPICE macromodel of spin-torque-transfer operated magnetic tunnel junctions", IEEE Trans. Electr. Dev., 57, 1425 (2010)
8. A. Lyle, J. Harms, S. Patil, X.F. Yao, D.J. Lilja, and J.-P. Wang, "Direct communication between magnetic tunnel junctions for nonvolatile logic fan-out architecture", Appl. Phy. Lett., 97, 152504 (2010)
9. Y.P. Li, B. Srinivasan, Y. Jing, X.F. Yao, M.A. Hugger, J.-P. Wang, and C.G. Xing, "Nanomagnetic Competition Assay for Low-Abundance Protein biomarker quantification in unprocessed human sera", 132, 4388 (2010)
10. B. Srinivasan, Y.P. Li, Y. Jing, Y.H. Xu, X.F. Yao, C.G. Xing, J.-P. Wang, "A detection system based on giant magnetoresistive sensors and high-moment magnetic nanoparticles demonstrates zeptomole sensitivity: potential for personalized medicine", *Angew. Chem. Int. Ed.*, 48, 2764 (2009).

## Appendix D Publications and Presentations (Cont.)

Presentations:

1. "Unique spin torque transfer switching in magnetic tunnel junctions with composite free layer" ED-08, IEEE International Magnetics Conference, Sacramento, CA, USA, May (2009)
2. "Spin torque transfer operated spintronic logic circuit" AS-09, 53rd MMM Conference, Austin, TX, USA, Nov., (2008)
3. "Design and fabrication of spin torque transfer devices with magnetic nano-current-confined structures", V.A-3, 66th IEEE Device Research Conference, UCSB, CA, USA, Jun. (2008)
4. "Magnetic-tunnel-junction-based programmable logic devices by spin transfer torque switching", FC-03, IEEE International Magnetics Conference, Madrid, Spain, May (2008)
5. "Observation of intermediate states in large magnetic tunnel junctions with compsite free layer", AA-05, IEEE International Magnetics Conference, Madrid, Spain, May (2008)
6. "Improved current switching symmetry of MTJ and GMR devices with nano-current-channel structure", BB-03, 52nd MMM Conference, Tampa, FL, USA, Nov. (2007)
7. "Spintronic logic devices based on magnetic tunnel junctions", CP-18, 52nd MMM Conference, Tampa, FL, USA, Nov. (2007)
8. "Patterned exchange-coupled composite media", DB-06, 10th Joint MMM/Intermag Conference, Baltimore, NJ, USA, Jan. (2007)
9. "(002) textured CoFe/MgO/CoFe Magnetic Tunnel Junctions on Cr underlayer", AC-07, the 50th MMM Conference, San Jose, CA, USA, Nov. (2005)